Technische Universität München
Fakultät für Physik

Dissertation

Novel Reaction Pathways through On-Surface Conditions: Tunneling-mediated Hydroalkoxylation and Gas-induced Deprotonation

Tobias Paintner

Technische Universität München
Fakultät für Physik

Novel Reaction Pathways through On-Surface Conditions: Tunneling-mediated Hydroalkoxylation and Gas-induced Deprotonation

Tobias Paintner

Vollständiger Abdruck der von der Fakultät für Physik der Technischen Universität München zur Erlangung des akademischen Grades eines Doktors der Naturwissenschaften (Dr. rer. nat.) genehmigten Dissertation.

Vorsitzender: Prof. Dr. Wilhelm Zwerger

Prüfer der Dissertation:
1. Priv.-Doz. Dr. Florian Klappenberger
2. Prof. Dr. Sabine Maier

Die Dissertation wurde am 15.04.2019 bei der Technischen Universität München eingereicht und durch die Fakultät für Physik am 07.05.2019 angenommen.

German title/Deutscher Titel:

Neue Reaktionswege durch Oberflächenbedingungen: Durch Tunneln vermittelte Hydroalkoxylation und gasinduzierte Deprotonierung

Abstract

In this thesis novel reaction mechanisms for a wide range of applications including the bottom-up construction of (primarily 2D) nanomaterials are investigated via space averaging as well as real space experimental methods complemented by computer simulations. First, a tunneling-mediated hydroalkoxylation reaction of a triply functionalized symmetric linear polyphenylene compound, F1-DETP, with a central ethynyl-group flanked by a hydroxyl- and carbonitrile-group and a deuterated variant of the same molecule are investigated on the Ag(111) surface. Second, a gas-induced deprotonation of a three-fold symmetric compound consisting of an aromatic ring bound to three ethynylphenyl moieties with the ethynyls pointing outwards, Ext-TEB, is examined on the same substrate. Both systems are characterized by a combination of scanning tunneling microscopy (STM), X-ray photoelectron spectroscopy (XPS), near-edge X-ray absorption fine structure (NEXAFS spectroscopy), temperature-programmed desorption (TPD), force-field molecular dynamics simulations within the CHARMM framework and density functional theory (DFT).

In the first part F1-DETP is deposited at low substrate temperatures (100-150 K), after which self-assembled superstructures characterized by a zig-zag-shaped structural motif are observed in STM image data. XPS and NEXAFS data confirm that under these preparation conditions, reactants are still present on the surface, which enables establishing a model for the analysis of the STM data since we conclude that these zig-zag domains consist of the intact species only. That the zig-zag assembly corresponds to intact molecules is confirmed by an analysis of the molecular fit, which reveals that they are stabilized by intermolecular ethynyl-hydroxyl and carbonitrile-hydroxyl H-bond interactions as well as by CHARMM force-field calculations. By step-wise annealing, the organic compound evolves into a chemically altered species and changes its self-assembled superstructures, now consisting of almost straight lines with a snake-like appearance. While the reaction itself occurs instantaneously, the ratio between reacted- and non-reacted species changes gradually with annealing steps. Again, analyzing the STM images with additional chemical information from XPS and NEXAFS enables designing a model which corresponds to force-field simulations, allowing the identification of the product as the aforementioned molecule in its ring-closed variant. This RC variant is obtained through an intramolecular covalent reaction, whereby the ethynyl and hydroxyl moieties react to form a furan ring in a hydroalkoxylation reaction. Considering the low temperature onset of this reaction combined with a counterintuitive coexistence of reactant and product domains on the surface for a large range of annealing temperatures, the hypothesis of a tunneling step involved

in the mechanism is conceived, which would allow for a slowly changing reaction rate at increasing annealing temperatures. TPD measurements evidenced that the rates of the species on the surface were not influenced significantly by desorption or deprotonation. In order to show such a tunneling effect, which is identified as rate-determining, a comparison between the original molecule and a deuterated variant is carried out. A new molecule (D-F1-DETP) was synthesized with deuterated hydroxyl groups and prepared under the same conditions as the original reactant F1-DETP, after which again STM image data is analyzed with the chemical information from XPS and NEXAFS investigations. Significantly higher annealing temperatures are required in order to increase the ratio of the product on Ag(111), while a steep increase would be expected for moderately higher annealing temperatures. This occurrence can be rationalized very well by a novel DFT method employed in collaboration with Jonas Björk, which achieves consistency with the atomic scale process, leading to the identification of a rate-determining tunneling step in the reaction mechanism, even when using the most conservative estimates and interpretations for the data gathered. To summarize this part, the proton-tunneling mediated intramolecular hydroalkoxylation has been verified by a number of techniques to a degree beyond any reasonable doubt. It could serve as a blue print for new tectons from which highly regular covalently bound structures can be formed on surfaces due to low activation energy and high chemical selectivity. Furthermore, it has been shown that a "switch" reaction like this can change the supramolecular assembly with implications especially for magnetically or optically active materials.

In the second part, a new method of preparation for building on-surface metal-coordinated networks with Ext-TEB on Ag(111) is investigated via STM. These networks are obtained from surface stabilized radicals created by oxygen exposure without resorting to Ullmann coupling and exhibit extraordinary range, regularity and stability. While Ext-TEB on Ag(111) exposed to molecular oxygen at low temperature (less than 200 K) leads to irregular structures and a modified surface, pre-adsorbed Ext-TEB on Ag(111) showed an intriguing deprotonation reaction after exposure to a low pressure oxygen atmosphere at higher temperatures (200 K). Slight annealing up to 375 K of the deprotonated species then leads to the formation of large scale (micrometer) exceptionally regular honeycomb networks, with single molecules linked to each other via an alkynyl–Ag–alkynyl bridging motif. Further annealing however does not result in a conversion towards a covalent bond, instead the network deteriorates. Other gases, CO or H_2O, did not yield any promising results regarding deprotonation. The conclusions are twofold: On the one hand, it was demonstrated that gas-mediated reactions can improve the way we synthesize carbon-based 2D sheet materials, while on the other hand, the metal-alkynyl networks are demonstrated to be extraordinarily stable with regard to temperature.

In summary, the thorough description and evaluation of the two reaction pathways unraveled in this thesis contribute to the understanding of chemical surface reactions. The rarely discussed aspect of tunneling under on-surface conditions is illuminated and gas exposure is combined with terminal alkynes in order to achieve deprotonation. The hydroalkoxylation presented in here represents the first instance of an interfacial synthesis of organic cycles via proton tunneling, while the gas-mediated deprotonation especially facilitates the synthesis of extended interfacial nanoporous molecular networks. Both mechanisms may have general implications for the UHV on-surface construction of carbon based sheet materials. Furthermore, they can also provide the basis for new bottom-up construction methods.

Contents

1 Introduction

From the earliest ideas of humankind of matter as a bulk of discrete subunits, it has taken us thousands of years to actually image these discrete subunits that we call atoms. While it turns out that they are not actually "uncuttable" as the Greek root of the word suggests and while other kinds of matter exist, our invasion into the world of the smallest things has turned out to be one of the most technologically and intellectually challenging but also rewarding journeys of our civilization. Research in this area has revolutionized our understanding of catalysis and chemical reactions in general [1], our understanding of the properties of matter, especially surfaces [2] and has also led to advanced technologies that have now become everyday devices [3]. We have even become able to direct matter to form from pre-designed building blocks or *tectons*.

It is however difficult to actually "see" atoms or molecules. The way we see things, by detecting photons reflected from surfaces towards our retina, proves difficult to achieve on the nanoscale as higher resolution will commonly require shorter wave length. While techniques utilizing X-rays in the way described exist and have been successfully tested [5], the problem is that shorter wavelengths mean higher photon energies which in turn leads to higher degradation for most materials. Furthermore such photons are more likely to penetrate further into the bulk. Therefore in order to probe materials more susceptible to damage other methods are necessary. Among these are the techniques employed in this publication: Scanning Tunneling Microscopy (STM), X-ray Photoelectron Spectroscopy (XPS), Near Edge X-ray Fine Structure Absorption (NEXAFS). While all three can influence (e. g. beam damage) the state of matter on a surface, such interference can either be deliberately employed (e. g. tip manipulation) or avoided. While STM directly visualizes single atoms and molecules on the surface, XPS and NEXAFS provide averaged chemical and orientational information about molecules on the sample. Combined, intriguing insights into the smallest of things are possible [6].

However, several challenges complicate our endeavor. The smaller our area (as in actual area) of interest becomes, the easier it becomes to detect movement, especially due to the thermal energy present in the sample. Detect sounds good, but if the movement impairs the measurement, the sample has to be cooled down to become measurable, which is commonly done in case of microscopy techniques. Even a cold sample will not guarantee success. Probing a sample requires an exact knowledge of what has been done to it and the exclusion of any external influence. In order to achieve such a clean state, nanotechnology often takes place in clean rooms; the techniques described above along with deep temperatures generally require or prefer vacuum technology for their application.

But going to such lengths is worth the pain. Having established that we *can* image matter as small as molecules [7], atoms [8] and beyond [9], we are able to check the results of what our pre-synthesized building blocks become due to the manipulations we employ, which grants us access to the world of bottom-up nanotechnology by allowing us to join molecular and

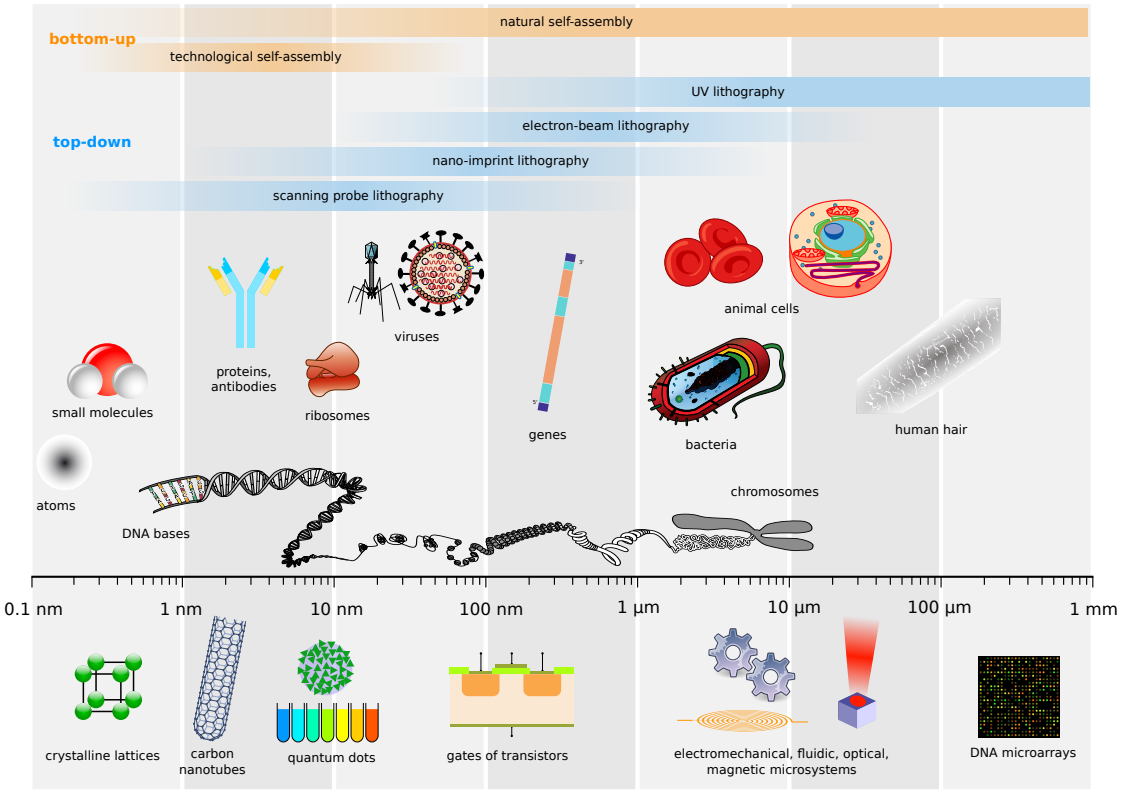

Figure 1.1: A comparison of the scales of objects in the world of nanotechnology and biology. While computers today already use transistors manufactured precisely at the nm-range via top-down methods, this work will focus on the manipulation and reaction of small molecules on crystalline lattices, scales only accessible through self-assembly methods. Figure cited from [4].

atomic building blocks into ultra-precisely manufactured functional materials [10]. Haunted by Moore's law [11], we have to consider options different from top-down methods to advance further, as these may inevitably hit their technical limits [12].

Relations and reactions between single building blocks or tectons are governed by attractive and repulsive interactions between one another. While different terminologies are in use for the process in which these tectons organize themselves [10, 13], self-organization or dynamic self-assembly, the principle is clear: by templating the constituents of a structure that is to be synthesized, the result is already ingrained in the building blocks, rather than starting from a perfect prototype as in top-down approaches. The chemical and physical interactions in this process are regulated especially by covalent and ionic bonds, complex chemistry as well as intermolecular bonds like simple electrostatic (and hydrogen bonds) and of course van der Waals interactions, while the interactions between substrate and/or solvent and tecton should not be omitted.

Yet of course, these forces and interactions are not simply our toolbox. They are the laws of nature and their most fascinating natural application is life itself. Molecular machines such as ATP-synthase [14] allow us to live, the molecule at the very heart of our existence is the self-replicating DNA, a double helix code molecule held together by hydrogen bonds [15].

The STM [16], which is the primary experimental method used for this work, has proven to be a versatile tool for discovering the (2D) nano-world. With it, fascinating insights of semiconductor [17] and metal [18] surfaces have been gained, most famously the 7x7 Si(111) dimer-adatom-stacking fault reconstruction was among the first STM results to be published. Further research items for this technique include atomic [19] and molecular switches [20], fractals built from molecules [21], molecular rotors [22], the magnetic properties of nanomaterials [23] as well as molecular networks with covalent [24] or metal complex [25] bonds. Especially the tuning of electronic structures is an aspect of this research, facilitated by the diversity of usable building blocks in bottom-up synthesis [26].

However, achievements of the main experimental method do not guarantee significant results. Therefore, the relevance and scope of the research presented herein have to be laid out. This thesis is concerned with two different surface reactions, which are both intriguing in their own right. First, an intramolecular hydroalkoxylation reaction of a functionalized terphenyl molecule on Ag(111) is presented. The key aspect of this reaction is that it proceeds at very low temperature. The low activation energy enables a high yield and allows us to suppress side reactions that otherwise often accompany chemical reactions [27, 28] leading to new covalent bonds in 2D bottom up synthesis. While the reaction itself is intramolecular, its mechanism can lead to a blueprint as to how to construct tectons that can elegantly form stable, covalently bound 2D materials on a given substrate. An explanation how such a low activation energy could be observed turned out to be difficult to achieve. The final conclusion, after excluding other options, was that the reaction mechanism included a rate determining hydrogen tunneling step from the hydroxyl group to the ethynyl moiety. In order to provide definitive evidence, a molecule with a deuterated hydroxyl group was synthesized and the relevant experiments were repeated. On the one hand, (hydrogen) tunneling steps in chemical reactions are fairly well known in chemistry generally, especially due to the pioneering work of Ronald P. Bell in the first half of the previous century [29, 30], with examples including an influence on biological processes such as enzyme activity [31, 32] and DNA mutations [33] as well as on

processes in extreme and cold, e. g. interstellar, environments [34, 35]. On the other hand, while tunneling is not unheard of in on-surface chemistry, as publications on diffusion [36], tautomerization [37], concerted tunneling in H_2O [38], hydrogenation [39] and desorption [40] exemplify, covalent, irreversible tunneling-mediated on-surface reactions of organic molecules remain rare.

Corroborated by theoretical analysis and XPS and NEXAFS experiments, a tunneling step in the reaction mechanism was confirmed. As already suggested above, the value of this research lies in its potential applicability to 2D-bottom up construction principles, while it might also enhance the way we approach research into other, possibly vital, chemical reactions in and around us.

Secondly, this work also focuses on a gas-mediated deprotonation reaction of a triangular molecules on Ag(111) consisting of three phenyl rings connected by C-C bonds to a benzene ring center, which have terminal alkynes attached opposite the C-C bonds. In the reaction, the terminal alkynes are deprotonated by molecular oxygen, which leads to the formation of extraordinarily regular and stable alkynyl-Ag-alkynyl honeycomb networks after slight annealing. The advantages of this gas-mediated reaction are similar to the above mentioned reasons for the relevance of a tunneling-mediated reaction: we achieve a long-range ordered material of exceptional quality in a process unhampered by side-reactions, adding a new method to our toolbox. Furthermore, carbon-metal-carbon (C-M-C) bonds could serve as an intermediate on the way to C-C bonded species on surfaces when starting with halogen-terminated organic species [41], while they are also promising candidates for novel topological insulators [42]. Though it was not possible to convert the network presented herein to C-C bonds, the mechanism and the resulting long-range metal-organic networks show fascinating new possibilities for bottom-up synthesis.

This thesis now proceeds with an outline of theoretical and experimental descriptions before presenting the insights gained through the above mentioned experiments, after which a conclusion and acknowledgements will follow.

2 Theory

2.1 Scanning Tunneling Microscopy

2.1.1 Tunneling

In the early 20th century, several ideas, such as the theory of general relativity and quantum physics, revolutionized our view of the world, of space, time and matter. Within surprisingly short amounts of time, applications in which these fundamental discoveries appeared were developed, such as GPS and the detection of gravitational waves in the case of relativity or the scanning tunneling microscopy in case of quantum mechanics. Tunneling is the process by which a particle can overcome a barrier whose passing its own energy would classically not allow. While this sounded somewhat paradoxical at the time (and still does), nature is our judge, not any kind of preconception or bias. Therefore, unsurprisingly, the tunneling effect was already identified as explanation for the α-decay by Gamow in 1928 [44], since classical physics could not be reconciled with the experimental observation.

Mathematically, the tunneling of particles can be calculated by solving the basic equation of quantum mechanics, the Schrödinger equation [45], which can be given as follows for a simplified 1D time-independent system (notation and formulae adapted from [46]):

$$-\frac{\hbar^2}{2m}\frac{d^2}{dz^2}\psi(z) + U(z)\psi(z) = E\psi(z), \tag{2.1}$$

The first part consists of the Hamiltonian operator of the system applied to the wave function ψ, $U(z)$ is a function for the potential barrier that has to be overcome while E is the energy of a particular state or wave function. The Schrödinger equation generally describes the evolution of a quantum state in time and space (here only space). This state is the wave function ψ, which is interpreted as a probability amplitude whose absolute square is therefore the probability density of the investigated quantity with respect to place, time or momentum. As STM is about tunneling electrons, we fix $m = m_{\text{electron}}$.

For the sake of simplicity, let us assume that $U(z)$ is strictly rectangular and finite, but higher than E. Solving this equation then requires two different expressions for $\psi(z)$. In the classically "allowed" region with $E > U$, we use

$$\psi(z) = \psi(0)e^{\pm ikz} \tag{2.2}$$

where

$$k = \frac{\sqrt{2m(E-U)}}{\hbar} \tag{2.3}$$

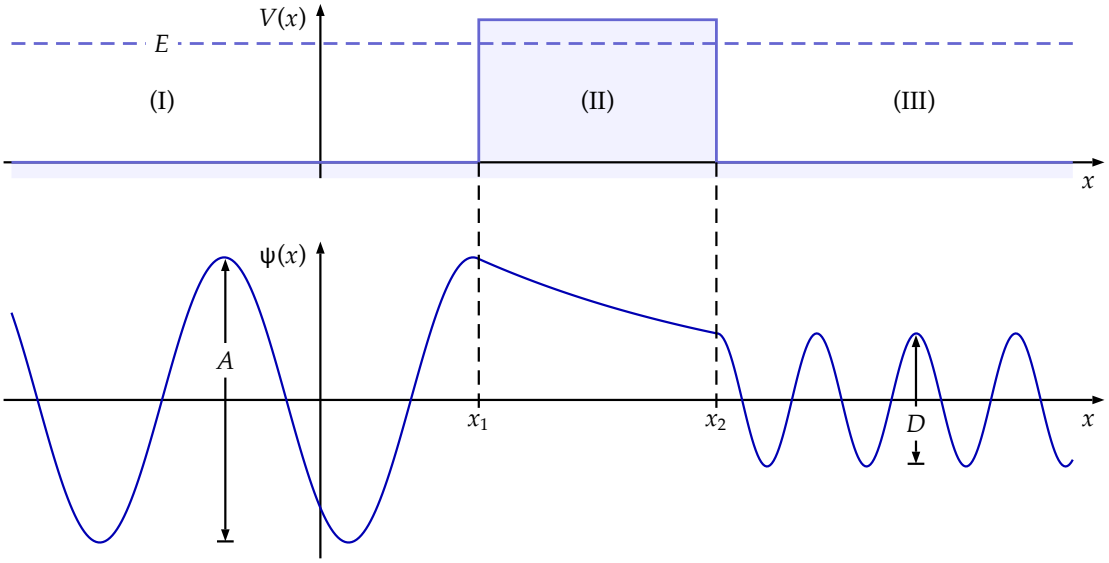

Figure 2.1: A wave impinging on a rectangular barrier; the amplitude is not zero on the right hand side of the barrier. For particles, this means that their probability of passing through the barrier is not zero, even if their energy would classically not let them pass through the barrier. Figure cited from [43].

while for the classically "forbidden" region with $E < U$ we use

$$\psi(z) = \psi(0)e^{-\kappa z} \tag{2.4}$$

where

$$\kappa = \frac{\sqrt{2m(U-E)}}{\hbar}. \tag{2.5}$$

In order to calculate the probability for the particle to be in the "forbidden" region, we use the square of its wave function

$$|\psi(0)|^2 e^{-2\kappa z} > 0. \tag{2.6}$$

A result above zero indicates that there is a chance of finding the particle in the "forbidden" region, which means tunneling has to be possible.

After this very basic discussion, we can turn to the situation in an STM. While we disregard temperature effects ($T = 0$), we do look at electrons in metals. These electrons occupy states up to the Fermi level, which is below the vacuum energy level. This vacuum level shall be used as a reference point here in the form $U = 0$. "Lifting" an electron from Fermi to vacuum level requires an amount of energy referred to as the work function, commonly called Φ, which depends on surface orientation and material [47]. When speaking of an STM, we have

a tip/sample system; here, let us assume that tip and sample are of the same material and have the same work function prior to any manipulation:

$$-\phi_{\text{tip}} = -\phi_{\text{sample}} = E_F \tag{2.7}$$

Thus, initially we obtain the same Fermi energy for both materials. Since this system would be quite boring and tunneling effects would cancel each other out, a manipulation has to be introduced. This is done by applying a voltage (called bias voltage) to one of the electrodes, in our case a positive bias to the sample:

$$E_{F\_\text{sample\_1}} = E_{F\_\text{sample\_0}} - eV \tag{2.8}$$

Since E_F is now lower in the sample than it is in the tip (since $E_{F\_\text{sample\_0}} = E_{F\_\text{tip}}$), the sample has unoccupied states where the tip has occupied states. Transmission rates can then be calculated by comparing the tunneling current with the impinging current at $z = 0$

$$T \equiv \frac{I(z)}{I(0)} = e^{-2\kappa z} \tag{2.9}$$

Another assumption, $eV << \Phi$ keeps said states E_n close to E_F, allowing for the statement $E_n \approx \phi$ and yields an easy-to-handle expression for κ

$$\kappa = \frac{\sqrt{2m\phi}}{\hbar}. \tag{2.10}$$

From equation 2.9 an important basic insight can be gained: T is exponentially correlated with z, thus distance is of high relevance here, something extraordinarily convenient for a surface imaging technique like STM.

2.1.2 Metal Insulator Metal Junction

John Bardeen already developed a time-dependent perturbation theory in 1961 [48] for metal-insulator-metal (MIM) junctions, which promotes the understanding of the STM's physical foundations. An important early application was its utilization in explaining the MIM junction behavior used by Giaever [49–51] to verify the Bardeen-Cooper-Schrieffer (BCS) theory of superconductivity [52].

In order to describe the tunneling junction, according to Bardeen's theoretical framework, it is first divided into two individual subsystems. The (stationary) Schrödinger equations of these subsystems are then first solved separately, after which time-dependent perturbation theory is applied, which shall then yield the electron transmission rate between the first and the second electrode. A tunneling matrix M is defined by surface-integrating over the unperturbed wave functions of the previously subdivided systems A and B at a separation surface (the surface itself can be chosen relatively unrestricted, if the electrodes are planar, it will be planar as well).

Subsystem A's Schrödinger equation in this framework has the form (adapted from [46])

$$i\hbar\frac{\partial\Psi}{\partial t} = \left[-\frac{\hbar^2}{2m}\frac{\partial^2}{\partial z^2} + U_A\right]\Psi, \tag{2.11}$$

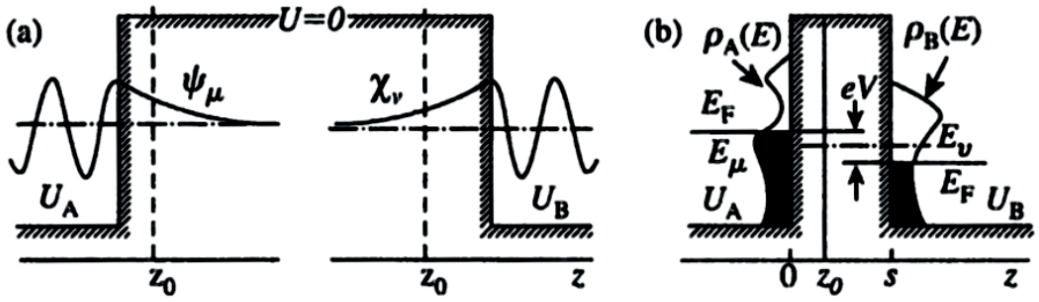

Figure 2.2: Bardeen tunneling theory in one dimension. a) Wave functions of electrodes A and B decaying into the potential barrier (the vacuum in between). b) Occupied and unoccupied states of both electrodes when a bias is applied, enabling tunneling from occupied states in A to unoccupied states in B. Cited from [46].

where $\Psi = \Psi(z,t)$ and U_A is the potential of system A. The stationary states

$$\Psi = \psi_\mu e^{-iE_\mu t/\hbar} \tag{2.12}$$

conform to the equation

$$\left[-\frac{\hbar^2}{2m}\frac{\partial^2}{\partial z^2} + U_A\right]\psi_\mu = E_\mu \psi_\mu. \tag{2.13}$$

On the other hand,

$$\Psi = \chi_\nu e^{-iE_\nu t/\hbar} \tag{2.14}$$

and

$$\left[-\frac{\hbar^2}{2m}\frac{\partial^2}{\partial z^2} + U_B\right]\chi_\nu = E_\nu \chi_\nu \tag{2.15}$$

describe electrode B.
Both electrodes are represented by

$$i\hbar\frac{\partial \Psi}{\partial t} = \left[-\frac{\hbar^2}{2m}\frac{\partial^2}{\partial z^2} + U_A + U_B\right]\Psi. \tag{2.16}$$

A graphic representation of these equations can be observed in Fig. 2.2 (a), where both electrodes are shown with their wave functions on either side of the potential. (b) shows the case in which a bias voltage is applied, which creates an energy window where there are unoccupied states in one electrode for occupied states in another electrode (see discussion above and from eq. 2.26 onwards).

This combination enables the transfer of a state from one system into the other, e. g. from A to B, which necessitates an adjustment of the time evolution of Ψ. Differing from eq. 2.12, we now have to use the wave function

$$\Psi = \psi_\mu e^{-iE_\mu t/\hbar} + \sum_{\nu=1}^{\infty} c_\nu(t)\chi_\nu e^{-iE_\nu t/\hbar}, \tag{2.17}$$

which is inserted into eq. 2.16 resulting in

$$i\hbar \sum_{\nu=1}^{\infty} \frac{\mathrm{d}c_\nu(t)}{\mathrm{d}t}\chi_\nu e^{-iE_\nu t/\hbar} = U_B\psi_\mu e^{-iE_\mu t/\hbar} + U_A \sum_{\lambda=1}^{\infty} c_\lambda(t)\chi_\lambda e^{-iE_\lambda t/\hbar}. \tag{2.18}$$

A more extensive treatment can be found in [53]. Note that ψ_μ and χ_ν are not eigenfunctions of the combined Hamiltonian. Yet we advance with the assumption that they are approximately orthogonal,

$$\int \psi_\mu^* \chi_\nu \mathrm{d}^3\mathbf{r} \cong 0, \tag{2.19}$$

therefore eq. 2.17 is still normalized up to a second order infinitesimal quantity proportional to $|c_\nu|^2$. Since the second term on the right hand side of eq. 2.18 is such a quantity, we can continue without it and proceed with an integral whose limits are given by the dimensions of U_B, as it is zero outside them

$$i\hbar\frac{\mathrm{d}c_\nu(t)}{\mathrm{d}t} = \int\limits_{z>z_0} \psi_\mu U_B \chi_\nu^* \mathrm{d}^3\mathbf{r} e^{-i(E_\mu - E_\nu)t/\hbar}, \tag{2.20}$$

This leads to a definition of the tunneling matrix element $M_{\mu\nu}$ as

$$M_{\mu\nu} = \int\limits_{z>z_0} \psi_\mu U_B \chi_\nu^* \mathrm{d}^3\mathbf{r}. \tag{2.21}$$

With this expression and an integration over time, eq. 2.20 becomes

$$c_\nu(t) = M_{\mu\nu}\frac{e^{-i(E_\mu - E_\nu)t/\hbar} - 1}{E_\mu - E_\nu}, \tag{2.22}$$

from which a transition probability $\mu(\mathrm{A}) \longrightarrow \nu(\mathrm{B})$ follows of the form

$$p_{\mu\nu} = |c_\nu(t)|^2 = |M_{\mu\nu}|^2 \frac{4\sin^2\left[(E_\mu - E_\nu)t/2\hbar\right]}{(E_\mu - E_\nu)^2}. \tag{2.23}$$

This fraction reaches its maximum as E_μ approaches the value of E_ν and vice versa, while otherwise it will quickly approach 0. The result is that the main contribution to the tunneling

current arises from processes where an electron tunnels from an occupied state in one electrode to the corresponding unoccupied state into the other electrode. Notice that with

$$\int_{-\infty}^{\infty} \frac{\sin^2 au}{\pi a u^2} \mathrm{d}u = 1 \tag{2.24}$$

together with the assumption of elastic tunneling ($E_\mu = E_\nu$), eq. 2.24 applied to the situation in eq. 2.23 leads to a delta function replacing the formula above due to $t \gg \frac{\hbar}{\Delta E}$ (corresponding to large a), enabling us to define a local density of states (LDOS) $\rho(E)$ in the transition probability

$$p_{\mu\nu}(t) = \frac{2\pi}{\hbar} |M_{\mu\nu}|^2 \rho_0(E_\mu) t. \tag{2.25}$$

For a constant DOS in both electrodes within the range of an applied bias voltage V, we can express the tunneling current as

$$I = \frac{2\pi e^2}{\hbar} |M_{\mu\nu}|^2 \rho_B(E_F) \rho_A(E_F) V. \tag{2.26}$$

An expression for Bardeen's tunneling matrix in the case of elastic tunneling in one dimension can be obtained by inserting eqs. 2.13 and 2.15 in eq. 2.21. After some mathematical simplifications it can be formulated as a surface integral of the wave functions of the two free electrodes

$$M_{\mu\nu} = \frac{\hbar^2}{2m} \int_{z=z_0} \left[\psi_\mu \frac{\partial \chi_\nu^*}{\partial z} - \chi_\nu^* \frac{\partial \psi_\mu}{\partial z} \right] \mathrm{d}x \mathrm{d}y. \tag{2.27}$$

Considering the case of a bias voltage V and finite temperature utilizing the Fermi distribution

$$f(E) = \frac{1}{1 + \exp[(E - E_F)/k_B T]} \tag{2.28}$$

by summing up over all states considered, 2.26 can be expressed as

$$I = \frac{4\pi e}{\hbar} \int_{-\infty}^{\infty} [f(E_F - eV + \epsilon) - f(E_F + \epsilon)] \rho_A(E_F - eV + \epsilon) \rho_B(E_F + \epsilon) |M|^2 \mathrm{d}\epsilon, \tag{2.29}$$

where $\rho_A(E)$ and $\rho_B(E)$ are the density of states (DOS) of electrodes A and B. Returning to our earlier assumption of $T = 0$, for which the Fermi-function becomes a step function and introducing $|M|^2 \approx$ constant, the tunneling current is given as a convolution of the DOS of both electrodes,

$$I \propto \int_0^{eV} \rho_A(E_F - eV + \epsilon) \rho_B(E_F + \epsilon) \mathrm{d}\epsilon. \tag{2.30}$$

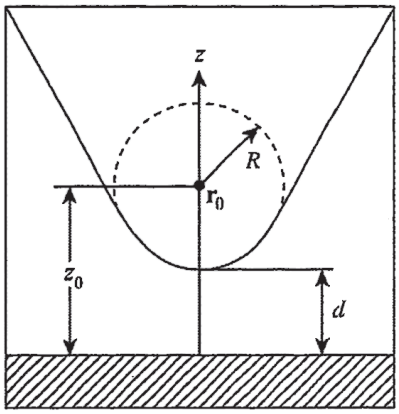

Figure 2.3: The Tersoff-Hamann model treats the tip as a locally spherical potential well. Cited from [46], after [57].

This results in a linear I-V-curve in tunneling spectroscopy for two ordinary metals, while for superconducting materials, a "gap" (zero current between two voltages, typically several meV with the exception of Cooper pair tunneling at $V = 0$) is observed.

The approximation of $|M|^2$ as constant can however not generally be employed as it will often depend on the energy, which is a concern in scanning tunneling spectroscopy (STS), especially as a frequent object of investigation are molecular states, where an energy range of up to several eV is required to, e. g., explore the HOMO/LUMO gap (details in the next part).

Since the experimental methods used herein do not refer to inelastic tunneling or spin polarized materials, their theory is not discussed in detail here, however a short overview can be provided.

Inelastic tunneling is caused by transmission loss effects, first observed due to molecules deposited in the tunneling junction by Jaklevic and Lambe [54] in 1966. The energy loss was caused by a molecular vibrational mode, resulting in a kink in the tunneling conductance G. Often, the quantity observed is $\frac{dG}{dV} = \frac{d^2I}{dV^2}$, where the loss feature appears as a blip. Since then, inelastic electron tunneling spectroscopy (IETS) has developed into a frequently employed method for materials characterization; in STM setups, lock-in amplifiers are utilized in order to extract G or $\frac{dG}{dV}$ for single molecules or other particles, surface conformations etc.

In the case of magnetic materials, tunneling currents that differ according to the magnetization of said materials are desirable. On the nano-level, such research is carried out via spin-polarized STM [55], while an effect widely applied in hard-drive read heads is the tunneling magnetoresistance [56].

2.1.3 Tersoff-Hamann

Bardeen's description of the tunneling junction refers to two approximately equivalent electrodes. This is not the case in an STM, where a planar electrode (the surface) and a tip form the system, therefore the previous theory had to be adjusted, which was achieved in the early

1980s by Tersoff and Hamann [57,58]. As can be estimated from eq. 2.30, the processed signals in STM data are a convolution of surface and tip DOS, which can hamper a straight-forward interpretation. Therefore a closer look at how the tip and its local DOS can improve data analysis is advisable. This was the objective of Tersoff and Hamann, who start by modeling the tip as spherically symmetric tip (scheme depicted in Fig. 2.3). It is possible to conclude that only the LDOS at the center of curvature of the tip is relevant for the tunneling current, leading to the assumption that constant-current (see below) STM images are essentially a Fermi-level LDOS contour of the surface. Conveniently, this would lead to STM data that only represents surface and not tip properties. A revised tunneling matrix can therefore be obtained,

$$M \propto \psi(\mathbf{r_0}), \tag{2.31}$$

which means the conductance can be expressed as

$$G \equiv \frac{I}{V} \propto |\psi(\mathbf{r_0})|^2 \rho_S(E_F), \tag{2.32}$$

where $|\psi(\mathbf{r_0})|^2 \rho_S(E_F)$ is the LDOS of the surface at the center of curvature of the tip.

The problem here is that the approximations do not hold in most cases. In order to provide fast evidence for this, a simple calculation of the minimally visible feature size can help: Fourier-expansions serve to discover the tip and sample wave functions satisfying the Tersoff-Hamann Schrödinger eq., which then lead to the matrix element. These Fourier-expansions contain a component $\mathbf{q}$ connected to the feature size a by the relation $|\mathbf{q}| = \frac{\pi}{\mathbf{a}}$ (more extensively in [46]), which, solved for a with $\kappa = 10\ \mathrm{nm}^{-1}$, yields

$$a = \frac{\pi}{|\mathbf{q}|} \approx 1\mathrm{nm} \gg \frac{\pi}{\kappa} \cong 0.3\mathrm{nm}. \tag{2.33}$$

where 1 nm is the limit calculated for the s-wave model, and 0.3 nm is the diameter of clearly experimentally observable silver atoms (similar sizes can be resolved for other metals and semiconductors, even without molecular tip functionalization). Therefore it becomes obvious that while the Tersoff-Hamann model is useful, for example in catalysis research via STM [59], in certain cases it would be an over-simplification. This means that other than s-waves have to be taken into account, in particular more localized p- and d-states.

An interesting aspect with regard to this work is the visibility of molecular species. Even the possibility of imaging molecules has been debated prior to its introduction due to the large gap between highest occupied and lowest unoccupied molecular orbitals (HOMO/LUMO) of several eV around E_F, which would have meant that for scanning close to E_F contributions should have been small. Yet of course, experimental data has shown that scanning molecules is possible. Some techniques can meanwhile even resolve the backbone of organic molecules. That molecules are not transparent in STMs is derived from non-resonant tunneling due to tails of the molecular orbital resonances, therefore even insulating materials (including inorganic layers) can usually be imaged. However, imaging molecules is not trivial. As pointed out above, the assumption that STM topographs are depicting the substrate LDOS does not always hold, for molecules the STM data is at least a mutually perturbed LDOS of adsorbate and substrate. Furthermore, STM images do not depict one particular orbital, even when at resonance, but also traces of other molecular orbitals [60].

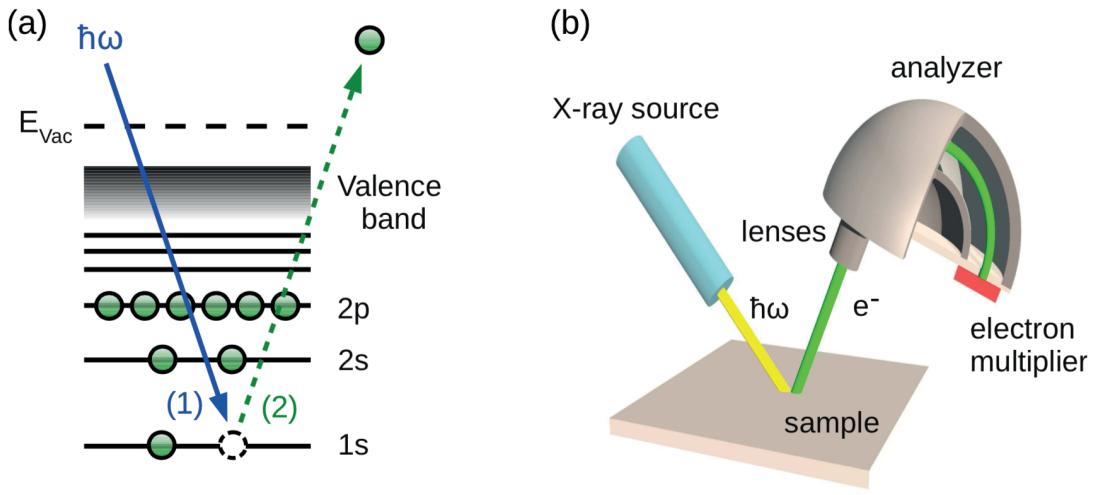

Figure 2.4: Scheme of XPS. a) The photoemission process in the simplest case, one photon transfers all of its energy to an electron which is ejected. b) A beam of photons with a certain energy hits the surface, ejecting electrons which are then guided through an analyzer before eventually hitting the detector. Cited from [66].

2.2 Photoemission

Photoemission is a result of the particle nature of light, famously formulated by Einstein in 1905 [61], his annus mirabilis. It is a discovery that later secured him the 1921 Nobel prize in physics [62]. After experimental discoveries by Hertz [63], Hallwachs [64], Thomson [65] and others in the late 19th century, it was already known that light impinging on an electrode could lead to a potential difference and an electric current, therefore the light must have had (re)moved charge carriers from the matter examined. The classical view did not deem this impossible, yet the way light achieved this effect was irreconcilable with theory at the time, since a gradual onset would be expected from the wave nature of light. However, the current measured did not increase gradually when the electrodes were irradiated, rather a certain maximum threshold wavelength λ or minimum frequency ν was necessary for the abrupt onset of the photoelectric effect, which also depended on the cathode material (as the work functions would differ). The reason for this is outlined in Fig. 2.4; as electrons have distinct binding energies, photoemission will only occur if a specific binding energy can be overcome. In order to measure the signal, the resulting electrons are filtered for their energy and counted via an electron multiplier.

A photon will not always simply eject an electron from any kind of material, several options are possible. Photons may simply pass through matter without any interaction (transparency), while on the on the other hand it can collide with a particle, especially an electron. In the second case, the electron can either gain some energy due to a partial energy transfer (Compton scattering), which may or may not lead to an ejection of the electron from the electrode, or a full energy transfer, which (without considering further electron scattering) will lead to an ejection of the electron if the photon is above the aforementioned energy threshold. Investigating the

latter electrons turns out to be quite interesting. Their kinetic energy can be described by the Einstein equation,

$$E_{kin} = \hbar\omega - E_b - \Phi, \tag{2.34}$$

where $\hbar\omega$ is the energy of a photon as given by the Planck relation [67], E_b is the binding energy of the electron (a quantity of utmost interest for chemical information, see below) and $\Phi = E_{vac} - E_F$, the energy necessary for the electron to reach the vacuum level, is the work function (the spectrometer work function). If all other quantities are known (Φ is a material constant), E_b can be calculated in order to obtain information about the chemical environment of the element investigated, as said environment (atoms covalently or supramolecularly linked to the element in question) will influence E_b, enabling the technique X-ray photoelectron spectroscopy (XPS).

XPS is sensitive to the situation on the surface, especially to the chemical condition of adsorbates, as electrons have a short attenuation length of only a few nm in the bulk. Due to retrievable binding energies via eq. 2.34 and since core level electron binding energies are exceptionally element- and environment-specific, the chemical properties of a material (near its surface) can be revealed. Note that the electron removed cannot be viewed as an isolated particle, therefore E_b is actually the ionization energy of the element investigated for one electron. The total energy difference between the system with N electrons and $N-1$ electrons, the initial state $|i\rangle$ and the final state $|f\rangle$ [68] is formulated as

$$E_b = E_f(N-1) - E_i(N). \tag{2.35}$$

The kinetic and binding energies have to be referenced. A useful choice is to reference E_b to the Fermi level, written E_b^F, and E_{kin} to the vacuum level, written E_{kin}^F, which leads to the expression

$$E_b^F = \hbar\omega - E_{kin}^V - \Phi. \tag{2.36}$$

2.2.1 Initial and Final State Effects

As pointed out above, an atom's electron cannot simply be treated without considering its surroundings. Removing it from its atom leads to a rearrangement of the remaining electrons, which means E_b is different from an electron's negative orbital energy $-\epsilon_k$. Therefore, Koopmans' theorem [69]

$$E_b \approx -\epsilon_k \tag{2.37}$$

does not hold when closer scrutiny is required. As pointed out in eq. 2.35, initial and final states influence E_b. When an electron is removed from the atomic shell, the rest will attempt to shield off the core hole in order to minimize the energy of the system. This leads to final state relaxation effects from intra- and extra-atomic relaxation (caused by electrons inside and outside of the atom excited), expressed in a contribution $E_r(k)$. Other (minor) influences occur

due to electron correlation $\delta_{\epsilon_{corr}}$ and relativistic effects $\delta_{\epsilon_{rel}}$, yielding an expression of the total binding energy reading

$$E_b = -\epsilon_k - E_r(k) - \delta_{\epsilon_{corr}} - \delta_{\epsilon_{rel}}. \tag{2.38}$$

While the equation seems to be applicable quite straight-forward, determining its parameters can be quite challenging. For now only a qualitative description of the causes for initial and final state effects are presented. In their initial state, atoms mostly differ from their isolated nature due to chemical bonds with other atoms. A shift in energy due to a bond (be it covalent or of another nature) is called a chemical shift and immediately leads to a very powerful application of XPS, as when checked against a reference value, these shifts can lead to the identification of reaction pathways on surfaces or yield other useful chemical information. Though a number of reasons (basically any change in the environment of the atom) can lead to a chemical shift, the most important shifts occur due to orbital hybridization and partial or full (in the case of ions) charge transfer. In order to illustrate this, imagine two atoms, A and B. A is more electronegative than B, thus A acquires a negative (partial) charge from B leading to less repulsion among the electrons in B, increasing E_b^B. On the other hand E_b^A will decrease with an increase of repulsion.

A number of reasons can cause final state effects. As outlined above, relaxation effects are a major issue but other options such as multiplet splitting and shake-up/offs are also possible. A shake-up takes place when some of the kinetic energy of the photoelectron is lost to another atomic electron transferred into a higher molecular orbital, leading to an E_b signal lowered by a discrete value, shake-off means that the additionally excited electron is also ejected from the atom [70, 71].

2.2.2 Spin Orbit Interaction

As XPS E_b spectra are usually calibrated using unique and well-known substrate signals observed as characteristic double peaks (e. g. Ag 3d) with certain area ratios, a look into how these peaks can exist seems reasonable. The doublet peaks in question only appear for $l > 0$ due to spin-orbit coupling from a magnetic field in the electron's rest frame, which can be formulated as (Biot-Savart's law) [72]

$$\mathbf{B_l} = -\frac{Ze\mu_0}{4\pi r^3}(\mathbf{v} \times \mathbf{r}) \tag{2.39}$$

where Z is the number of protons in the nucleus, e the elementary charge and μ_0 the magnetic constant. The negative sign is a result of the core movement in the electron's rest frame. Inserting $\mathbf{l}$ and a transformation into the core's rest frame employing the relativistic Thomas correction factor of $1/2$ [73] yields

$$\mathbf{B_l} = \frac{Ze\mu_0}{8\pi r^3 m_0}\mathbf{l}. \tag{2.40}$$

The exchange energy operator is given by the product of the electron's magnetic moment

and the field

$$V_{ls} = -\boldsymbol{\mu}_{\mathbf{s}} \cdot \mathbf{B}_{\mathbf{l}}, \tag{2.41}$$

where

$$\boldsymbol{\mu}_{\mathbf{s}} = -g_s \frac{e}{2m_0}\mathbf{s}, \tag{2.42}$$

with an electron g-factor of about 2 and the spin angular momentums $\mathbf{s}$.
The definition of the total angular momentum

$$\mathbf{j} = \mathbf{l} + \mathbf{s}. \tag{2.43}$$

requires some mathematical transformations but then yields

$$\mathbf{ls} = \frac{1}{2}(\mathbf{j}^2 - \mathbf{l}^2 - \mathbf{s}^2). \tag{2.44}$$

A combination of eqs. 2.40, 2.42, 2.44 and 2.41 after replacement of the operators with their eigenvalues (possible as they commute) where $a = Ze^2\mu_0\hbar^2/(8\pi m_0^2 r^3)$ allows the formulation

$$V_{ls} = \frac{a}{2}\left[j(j+1) - l(l+1) - s(s+1)\right], \tag{2.45}$$

with a new quantum number j,

$$j = |l \pm s| = \left|l \pm \frac{1}{2}\right|, \tag{2.46}$$

responsible for doublet splitting in orbitals beyond s in XPS due to different energies for different j.
The second new quantum number

$$m_j = [-j, -(j-1), ..., j], \tag{2.47}$$

the j projection along the z-axis yields the degeneracy of a j value as $2j + 1$, which causes the intensity ratios observed in doublet splitting.

SOC heavily depends on the atom's core charge (and therefore mass), which is not immediately visible from the expression for a given above. However, because of the relationship between r^{-3} and Z, the actual correlation is $a \propto Z^4$.

2.2.3 Spectral Aspects and Quantitative Analysis

As already extensively discussed, the photoemission process is complex and the "standard" collision (photon transfers energy to electron and electron is immediately measured) is not always achieved. A common occurrence is that when the core hole in the excited atom is filled with an electron of the same atom from a higher shell and thus with excess energy, this excess energy has to be released. This is possible either by the emission of a photon or an

Auger electron, whose signature is visible in the E_b spectrum at a certain energy value; as their energy does not depend on E_{kin}, their position in the E_b spectrum calculated with the Einstein equation varies when $\hbar\omega$ is varied, leading to yet another surface analysis technology, Auger electron spectroscopy (AES) [70, 71].

In the case of XPS, commonly the signal will vary with the X-ray source used (monochromatized radiation is preferred) and electrons can be emitted from the valence band instead of the core band or loss features can be observed. Further, a background of secondary and inelastically scattered electrons always accompany the signal, which necessitates background subtraction, which was achieved here with a linear fit and subsequent normalization, whereafter the resulting peaks were fitted with a Voigt function. This is especially important for quantitative analysis, a powerful usage of XPS allowing to check for relative (and in some cases absolute) abundance of elements investigated in a certain area, yielding stoichiometric information about, e. g., adsorbed species. A theoretical description of XPS signal intensity can be given as [74]

$$I_{ij} = J_0 \sigma_{ij} T(E_{kin}) \int_{\gamma=0}^{\pi} \int_{\varphi=0}^{2\pi} L_{ij}(\gamma) \int_{z=0}^{\infty} n_i(z) \exp\left(\frac{-z}{\lambda_i \cos(\theta)}\right) \mathrm{d}z \mathrm{d}\gamma \mathrm{d}\varphi, \tag{2.48}$$

where I_{ij} denotes the peak intensity of element i with core level j, J_0 the incident X-ray beam intensity, $\sigma_{ij}(\hbar\omega)$ the photon wave-length dependent cross section, $T(E_{kin})$ the electron energy dependent transmission function; the integration over $L_{ij}(\gamma)$ takes into account the angular dependence of photoemission while the second integral takes into account from how many substrate atoms the signal will originate from by multiplying the number of atoms of element i depending on depth z with an exponential term containing the attenuation length λ_i and the escape angle θ to exclude electrons unable to leave the bulk. This attenuation can also be deliberately used to increase or decrease the surface sensitivity of XPS. The attenuation length is defined as the distance an electron beam in a material has to traverse to lower its intensity to $1/e$, formulated separately as

$$I = I_0 \exp\left(\frac{-d}{\lambda \cos(\theta)}\right), \tag{2.49}$$

which means that varying θ [68], usually by tilting the sample, can increase (grazing emission) or decrease (normal emission) the surface sensitivity in a given experiment [70, 71].

2.3 NEXAFS

While XPS is quite useful when analyzing the chemical behavior of surfaces and adsorbates, it does not usually contain any information about the adsorption geometry of particles, especially molecules on a surface. NEXAFS in this case is an extraordinarily powerful technique allowing the analysis of how molecules adsorb in terms of space due to the polarization dependence of its signal. The approach at first is similar to XPS, photons of a known energy are directed towards the sample. Yet here, already two important differences have to be pointed out: the

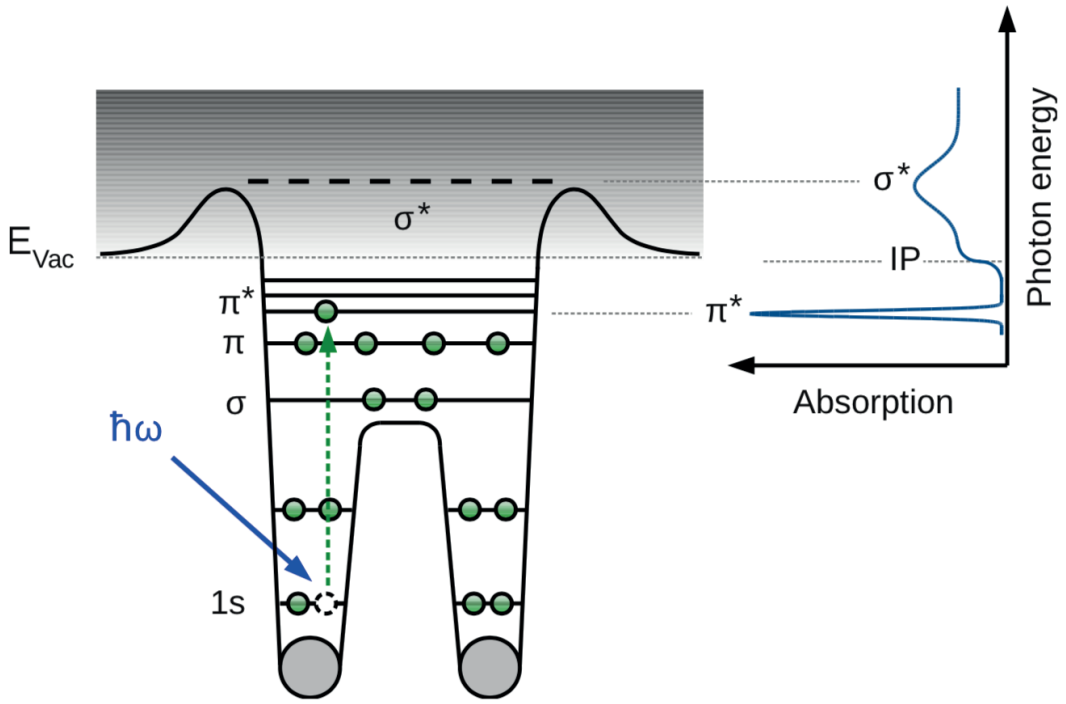

Figure 2.5: NEXAFS principle and correlation of the impact process with orbital contributions. An electron is excited to a higher orbital and a hole is created, here, a π^* resonance is observed. Cited from [66].

photons' energy has to be variable and the light has to be polarized. In the energy ranges here (several hundred eV), usually the light emitted from synchrotrons is employed (experimental description below). Continuing from above, the photons in this case are – contrary to the XPS case – not intended to directly remove an electron from an atom, instead, as the name suggests, the atom should absorb the photons energy (near an absorption edge, usually the K-edge), which then raises the electron's energy into a higher orbital and creates a core hole in a lower band. This process has two issues attached: First, detection is only possible due to a secondary effect caused by the decay of this state. Second, while a photon will trivially have to have enough energy to cover the difference between final and initial state, the orbital change of the electron also follows selection rules, the angular momentum quantum number has to differ by one, leading to a situation where s- or p-type orbital electrons can only transfer into p- or s-type orbitals respectively, but not into orbitals of the same nature. (Initial and final state energy conditions are similar to the XPS case, with relaxation effects commonly having the highest influence, followed by correlation effects and multiplet splitting, with relativistic corrections usually of minor relevance [75]). The secondary effects used in order to gather a signal are comprised of Auger electrons, which can be easily detected using a channeltron, or photons emitted by the decay process. Here, electron detection was applied.

The most important features observed in NEXAFS spectra are the anti-bonding π^* and σ^*

signals. While for a more thorough treatment, [75] is recommended, in general bonding and anti-bonding states are arranged from σ, the strongest bonding state, via π and π^*, to σ^*, the highest energy anti-bonding state (cf. Fig. 2.5). Qualitatively, the σ state has an electron density directly in between and around the nuclei (commonly defined as the z-axis of the system), leading to effective shielding and lower electrical potential between the nuclei, while a σ^* state leads to the exact opposite; the electron density is lowest between the nuclei and shielding is inefficient, even more than in the situation of π^* states. π (p_x, p_y) states however create no electron density directly in between the nuclei but only parallel to the bond and therefore bind less strongly than σ bonds. While the π^* signal is a very sharp resonance below the binding energy E_b, which means it is still relatively stable, a step can be observed when the photon energy $\hbar\omega$ reaches E_b (see inset in Fig. 2.5) as then transitions above the vacuum level occur, on the other hand the σ^* is typically a relatively broad resonance beyond E_b, due to a photoelectron emission shortly after the excitation, leading to a short lifetime of the state.

While interpreting NEXAFS spectra for one particular element which is always in the same chemical configuration can be quite straight-forward, the case becomes very complicated for any real system with the same element in different configurations. For this reason, theory is often a necessary part of analyzing the spectrum, as a comparison between the theoretically calculated spectrum and the observed spectrum tremendously corroborates any argument.

As pointed out before, the information gained by NEXAFS experiments is very valuable as it can reveal the orientation of molecules. As already hinted above, molecular orbitals have strong directional character and directly correlate with molecular geometry. The polarization dependence of the transition intensity is mathematically expressed using the X-ray absorption cross section, with the angular dependence included in the dipole matrix element $\langle f|\mathbf{r}|i\rangle$ and X-ray polarization along unit vector $\mathbf{e}$ as [75]

$$I_{if} \propto |\langle f|\mathbf{e}\cdot\mathbf{r}|i\rangle|^2 \propto |\mathbf{e}\cdot\langle f|\mathbf{r}|i\rangle|^2. \tag{2.50}$$

As mainly the K-shell excitations of second row element, such as C, N or O are considered, a description of their polarization-dependent signal seems most valuable. Here, a transition from the very localized 1s initial state $|i\rangle = R_{1s}(r)$ shall take place to a final state composed of 2s and 2p states. Employing the linear combination of atomic orbitals (LCAO) technique, the final state wavefunction is formulated as a linear combination of excited atomic 2s and 2p states as [75]

$$|f\rangle = a|2s\rangle + b|2p_x\rangle + c|2p_y\rangle + d|2p_z\rangle \tag{2.51}$$

$$= aR_{2s}(r) + R_{2p}(r)(b\sin\theta\cos\phi + c\sin\theta\sin\phi + d\cos\theta) \tag{2.52}$$

with weighting coefficients a, b, c, and d. Since both, the s-type contribution in the final state and the s-type initial state are radially symmetric, any polarization dependence will occur due to the p-contributions of the final state, furthermore dipole selection rules exclude a transition between 1s and 2s. Therefore, a direction for the final state can be defined with the weighting factors and unit vectors $\mathbf{e_i}$ as

$$\mathbf{O} = (b\mathbf{e_x} + c\mathbf{e_y} + d\mathbf{e_z}). \tag{2.53}$$

The dipole moment can now be split into a radial dipole moment contribution R and $\mathbf{O}$, which after introducing spherical coordinates can be written as

$$\langle f|\mathbf{r}|i\rangle = R\frac{4\pi}{3}\mathbf{O} \tag{2.54}$$

or in full

$$\langle f|\mathbf{r}|i\rangle = \int R_{1s}(r)R_{2p}(r)r^3dr\frac{4\pi}{3}(b\mathbf{e_x} + c\mathbf{e_y} + d\mathbf{e_z}), \tag{2.55}$$

with eq. 2.50 (note $\mathbf{e}$ from here onwards is simply the direction of $\mathbf{E}$ again)

$$I_{if} \propto |\mathbf{e}\cdot\langle f|\mathbf{r}|i\rangle|^2 \propto |\mathbf{e}\cdot\mathbf{O}|^2 \propto \cos^2\delta, \tag{2.56}$$

where δ is simply defined as the angle between $\mathbf{O}$ and $\mathbf{E}$. It follows that the transmission intensity is directly correlated with the squared cosine of this angle.

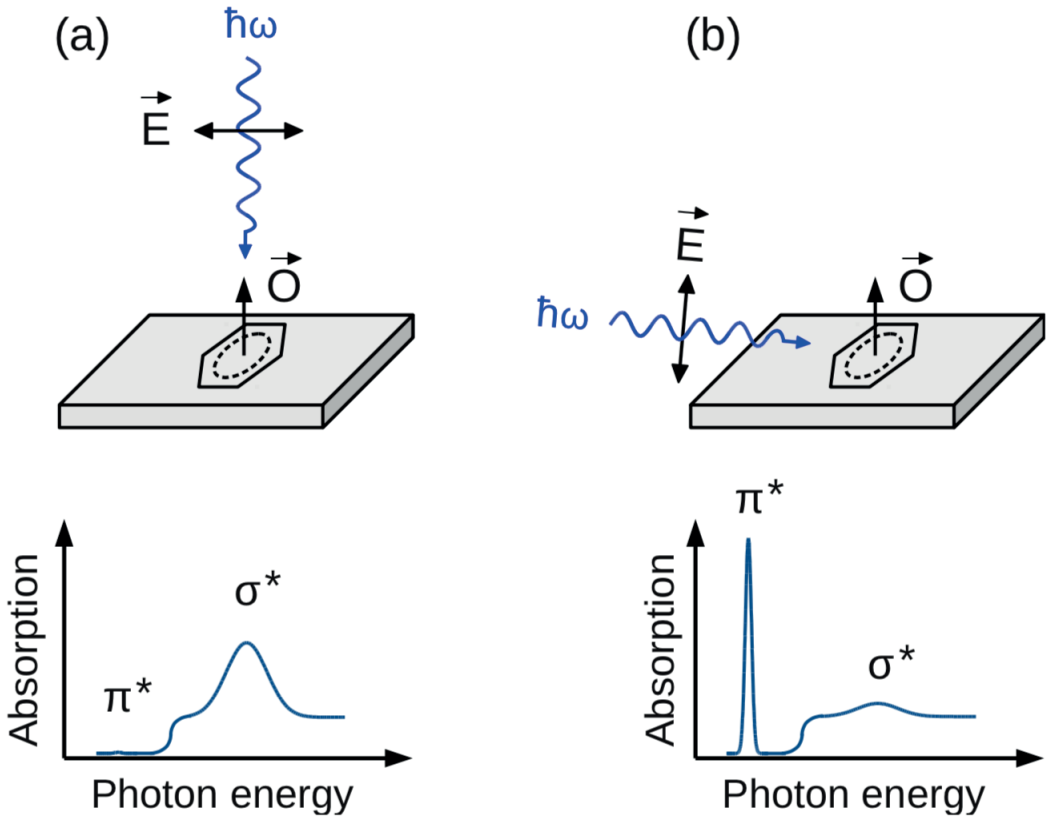

Figure 2.6: NEXAFS structural analysis example using benzene. π^* orbitals are oriented in $\mathbf{O}$ direction, while $\mathbf{E}$ is the field vector. If benzene lies flat on the surface, both vectors are parallel for grazing incidence, resulting in a detected signal for π^*, while σ^* is quenched. The opposite is observed for normal incidence. Cited from [66].

For simple, second row, diatomic molecules such as N_2, what would this result in? The σ^* orbital extends, as is commonly defined, along the z-axis, therefore in order to maximize the dot-product $|\mathbf{e} \cdot \mathbf{e_z}|^2$, the X-ray electric field would have to be aligned parallel to the final state orbital, thus transition intensity depends on the squared cosine of the angle between the two vectors. For the π^* resonance, the direction of $\mathbf{e}$ has to align with x- and y-oriented p-type orbitals, due to which, because of superposition of both π^* influences, transition intensity is correlated with the squared sine of the angle between $\mathbf{e_z}$ (used for σ^* above) and $\mathbf{e}$. Analogously, the rationale for benzene and benzene-like molecules is depicted in Fig. 2.6. This sine - cosine relationship ensures the polarization/orientation sensitivity of NEXAFS.

2.4 Density Functional Theory

Density functional theory (DFT) is at its core a technique designed to enable the ab initio[1] simulation of complex electronic structures. While theoretically, even a many-body system can simply be described by its Schrödinger equation, such a calculation turns out to be too complex for most systems like larger molecules due to the many degrees of freedom. DFT reduces the complexity of the system with several assumptions while still preserving an extraordinary degree of accuracy, which explains its popularity. While the author of this work did not explicitly use DFT himself, a very general explanation should still be provided as the experimental data presented herein was validated with and compared to DFT theoretical models in order to show their consistency.

In general, a ground state with N electrons can be described by a wave function that depends on $3N$ coordinates. The Hohenberg-Kohn-Theorem [76] then asserts that this state is also given by the spatially dependent electron density $n(\mathbf{r})$, as this defines its potential. In DFT, this means that by finding the electron density in the ground state, other features of the system in this condition can be derived, since they are functionals of the density. An overview also used as a basis of the following discussion can be found in [77].

As pointed out above, DFT relies on simplifications in order to reduce complexity. The first important simplifying assumption is the Born-Oppenheimer approximation [78], which basically states that heavy and light particles change their directional movement on very different time scales. In the case of a molecule, this means that for the electrons the nuclei are basically fixed in space, therefore they behave like attractive potentials $\hat{V}_{en}$ and repulsive potentials $\hat{V}_{nn}$.

The electron density is determined by self-consistently and iteratively solving the Kohn-Sham-equations [79] (presented in atomic units here)

$$\left(-\frac{1}{2}\nabla^2 + v_{\mathrm{eff}}(\mathbf{r}) - \epsilon_j\right)\phi_j(\mathbf{r}) = 0, \tag{2.57}$$

[1] Calling DFT methods ab initio is somewhat controversial, especially since often when DFT is mentioned, in fact approximations are concerned. When ab initio is understood as "from first principles", even some approximation methods can be considered ab initio, however, many functionals contain empirical parameters. A useful discussion might be found at `https://chemistry.stackexchange.com/questions/33764/is-density-functional-theory-an-ab-initio-method`.

by inserting ansatz functions ϕ_j, leading to N solutions for the effective potential v_{eff}. As these solutions are independent of each other, they can be solved separately, leading to an easier calculation. The electron density is given by summing up over the electron density of each Kohn-Sham-equation (i. e. its wave function's absolute squared)

$$n(\mathbf{r}) = \sum_{j=1}^{N} \left|\phi_j(\mathbf{r})\right|^2, \tag{2.58}$$

the effective potential in turn depends on the electron density. In general, three influences on the effective potential have to be taken into account: $v(\mathbf{r})$, the external potential caused by the nuclei, the Hartree term (second in the following equation) describing the electrostatic potential between the electrons, and $v_{\mathrm{xc}}(\mathbf{r})$, the exchange correlation potential, which is defined so that it will take into account, as the name implies, exchange and correlation effects of the many-body system and is generally not known. Mathematically, the potential is expressed as

$$v_{\mathrm{eff}}(\mathbf{r}) = v(\mathbf{r}) + \int \frac{n(\mathbf{r'})}{|\mathbf{r} - \mathbf{r'}|} \mathrm{d}^3 r' + v_{\mathrm{xc}}(\mathbf{r}). \tag{2.59}$$

As can be concluded from the above equation, $v_{\mathrm{eff}}(\mathbf{r})$ depends on $n(\mathbf{r})$ due to the Hartree term, which explains why the process of achieving a self-consistent solution can and has to be achieved iteratively. The Kohn-Sham functions are to be interpreted with care, as in general they do not necessarily describe physical reality beyond their role in the Kohn-Sham equations, while useful insights might still be gained from their careful analysis.

As pointed out above, the problem in this approach so far is that $v_{\mathrm{xc}}(\mathbf{r})$ is not known and has to be approximated. This is complicated by the fact that $v_{\mathrm{xc}}(\mathbf{r})$ does not only depend on $n(\mathbf{r})$ in one point in space but on the full spatial electron distribution. Several approximation techniques are used in order to find the exchange correlation potential. The local density approximation (LDA) only takes into account the electron density in one point, leading to a binding energy over-estimation (overbinding), whereas the general gradient approximation (GGA) also takes into account the density gradient. Hybrid methods combine either of these approaches with the Hartree-Fock method, which is then used to calculate the exchange energies of the Kohn-Sham functions. Since in any case, an approximation is employed, there are some issues with regard to their choice. Such problems include binding energies deviating from experimental values, underestimated bandgaps, and blindness for van der Waals interactions in "semi-local" methods due to their long-range charge distribution correlation.

As for the wave functions inserted as ansatz into the Kohn-Sham equations, several options are possible, which should be used according to which ansatz allows the most efficient solution by the computing system. Muffin-tin orbitals are suitable for the description of core states, while plane waves are used for modeling valence electrons. Since plane waves can easily be Fourier-transformed, which allows solving the Kohn-Sham equations quickly, condensed matter calculations often use them as a basis with additional precautions for core electrons, either through a completely separate treatment (augmented plane waves) or through the addition of other wave functions (projector augmented waves) or by introducing a pseudo-potential.

For molecular systems, Gauss functions pre-optimized for each atom and based on the hydrogen atom functions are commonly combined linearly in order to find molecular orbitals

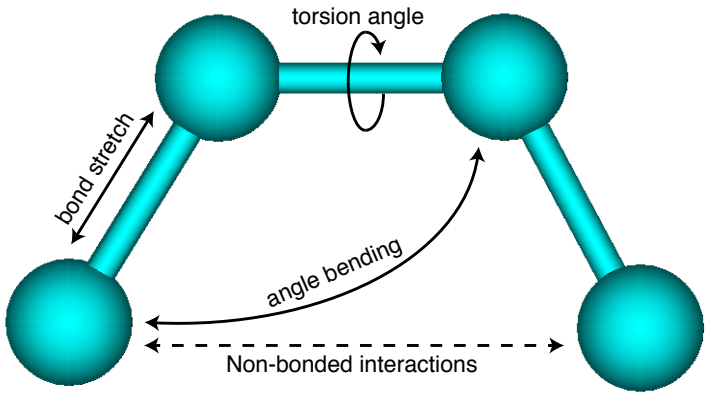

Figure 2.7: Illustration of the contributions in molecular force-field simulations.

(linear combination of atomic orbitals, LCAO).

2.5 Force-Field Simulations

As a further computer simulation method, force-field is applied in here in order to show the consistency between models fitted to STM data and the theoretical alignment of surface molecules. Employing the program *Chemistry at HARvard Macromolecular Mechanics* (Charmm) [80–82] with its implementation of the *Merck Molecular Force Field* (MMFF) [83–87] several samples were simulated by minimizing their total energy, expressed generally in the context of force-field as

$$E_{\text{total}} = E_{\text{bonded}} + E_{\text{nonbonded}}, \tag{2.60}$$

where

$$E_{\text{bonded}} = E_{\text{bond}} + E_{\text{angle}} + E_{\text{dihedral}} \tag{2.61}$$

and

$$E_{\text{nonbonded}} = E_{\text{electrostatic}} + E_{\text{van der Waals}}. \tag{2.62}$$

In force-field simulations, contrary to its name, the focus is on potentials and how they are approximated, so that the resulting structure with the lowest calculated energy emerges. Bond and angle terms, for example, are usually not determined by the Morse potential, instead it is replaced with the less computationally expensive quadratic potential. Non-bonded interactions, as indicated above, generally take into account van der Waals interactions (via the Lennard-Jones potential) and electrostatic interactions (via the Coulomb potential) but only up to a certain cutoff, as larger systems would become exponentially more difficult to calculate. Herein, a final cutoff for non-bonding interactions was set at 8 Å with the potential fading within this limit in a sigmoidal fashion. The substrate in the simulation consisted of three

slabs of Ag(111) compressed into one plain with all silver atom positions fixed. This surface handling was previously described in [88]. Simulations were carried out without taking into account temperature effects.

3 Experimental Setup

3.1 Scanning Tunneling Microscope Setup

The STM set-up consists of a stainless-steel chamber, subdivided into a preparation part and an STM part, decoupled from surface percussions by pneumatic dampers during measurements and pumped by a multi-stage arrangement of pumps. The system generally maintains a base pressure of $p \approx 10^{-10}$ mbar (ultra high vacuum, UHV), the STM is routinely kept at a temperature of ~4 K (liquid helium) with a commercial cryostat by Cryovac; temperatures of 1.2 K can be reached via a Joule-Thomson stage (see below). Transfer between the chambers and into and out of the vacuum system is achieved with manipulators, manipulator-STM transfer is accomplished with a wobble stick (a magnetically operated, freely movable, grabbing device).

3.1.1 STM

The commercial STM by SPECS GmbH (Berlin) is constructed in a so-called "walker design", which means the electrochemically etched tip (usually tungsten) is attached to a scanner tube (for fine movement) which is in turn affixed to a scanner-holder (for coarse movement). As the name suggests, the scanner-holder "walks" within a cavity due to piezoelectric movement. Piezo-elements have been instrumental in STM development, their deformation upon application of a voltage allows for extremely high precision movements. In the system at hand, depicted in Fig. 3.1, after introduction into the STM with the wobble stick, the sample is first moved with coarse y-piezos which allow lateral movement in order to maneuver it into tracks in the STM stage. The sample is then approached coarsely with the scanner-holder in z-direction, whereafter the deformation (in x-, y- and z-direction) is applied solely to the scanner tube resulting in a scan frame of the area reachable by the scanner tube. Collision during coarse approach is avoided by a stepwise process, the scanner-holder will carry out as many steps as the z-deformation of the scanner tube can cover. After one coarse movement, the scanner tube probes its full z-range until substrate contact is detected; if it is not, the scanner tube withdraws in z-direction after which the process is repeated. While piezoelectric elements offer highly precise access to the nanoworld, several issues are noticed. When scanning an STM image, the tube is moved above the surface line by line, resulting in a fast and slow scanning direction, resulting in possible distortions, while also the position in the scan frame may influence the scan as well as thermal drift, if tip and sample have not yet reached equilibrium. Further scanning issues are caused by effects from a real tip, i. e. one that is not necessarily atomically sharp (which is usually remedied by controlled tip crashes into the sample, "tip forming", or high voltage pulses, "bias pulses"). Further vibrational isolation is ensured by an STM head hanging on springs. Images are obtained either by scanning the sample in constant current or constant height mode, which are characterized by the following features:

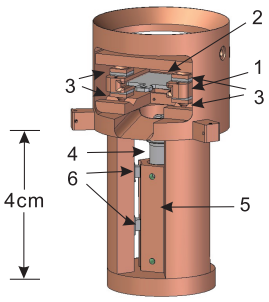

Figure 3.1: Schematics of STM head, (1) sample rack, (2) sample and sample plate, (3) piezo for coarse motion in x-direction, (4) tip and scanner, (5) scanner-holder (Cu prism), and (6) piezo for coarse motion in z-direction. Cited from [89].

- **Constant Height Mode (CHM)**: The tip is moved over a surface at a pre-set tip-sample distance and a fixed value for the applied bias voltage V_{bias}. Prerequisite for this scanning mode are a relatively even and well aligned sample, and a high stability of the system in general. As pointed out above the tunneling current I_{tunnel} will then exponentially depend on the height of surface features (and thereby tip-sample distance), from which an STM topograph is calculated.

- **Constant Current Mode (CCM)**: Scanning in constant current mode requires a feedback-loop that continuously adjusts the (apparent) tip-sample distance, so that a "setpoint" specifying V_{bias} and I_{tunnel} can be kept. Apparent is mentioned, as especially when molecules or different materials are involved, the measured current will not exactly correspond to the tip-sample distance. Feedback parameters (in conjunction with scan speed and size) have to be tuned carefully, so that no overreaction or crash occurs.

While imaging represents the primary purpose of scanning tunneling microscopy, an extremely sharp metal-tip aligned extraordinarily precise over and very close to a surface inherently enables manipulation capabilities of matter, which is of obvious interest when dealing with adsorbates. For these manipulations, several techniques can be employed.

Firstly, a particle can be picked up or dropped by moving the tip close to it, often in a pre-programmed manner (which may or may not include a voltage pulse), in the way of Vertical Manipulation. This method is applied for transporting matter across the surface or tip functionalization (picking up a molecule of the sample under investigation can, for example, greatly improve resolution; a more controlled option includes picking up co-evaporated CO but even tip electronic and magnetic properties can be tuned [7, 91])

Secondly, a particle can simply be moved laterally. Several possible mechanisms can be utilized: "Dragging" is enabled by the attractive force between tip and particle, "pushing" refers to tip-induced movement from repulsive interaction, while "sliding" means that the particle is trapped under the tip when moving [92]. In order to induce lateral manipulation, the tip is approached to the particle of interest, usually the feedback is turned off and occasionally the setpoint is set to a desired value (which may be done before and after turning off the feedback,

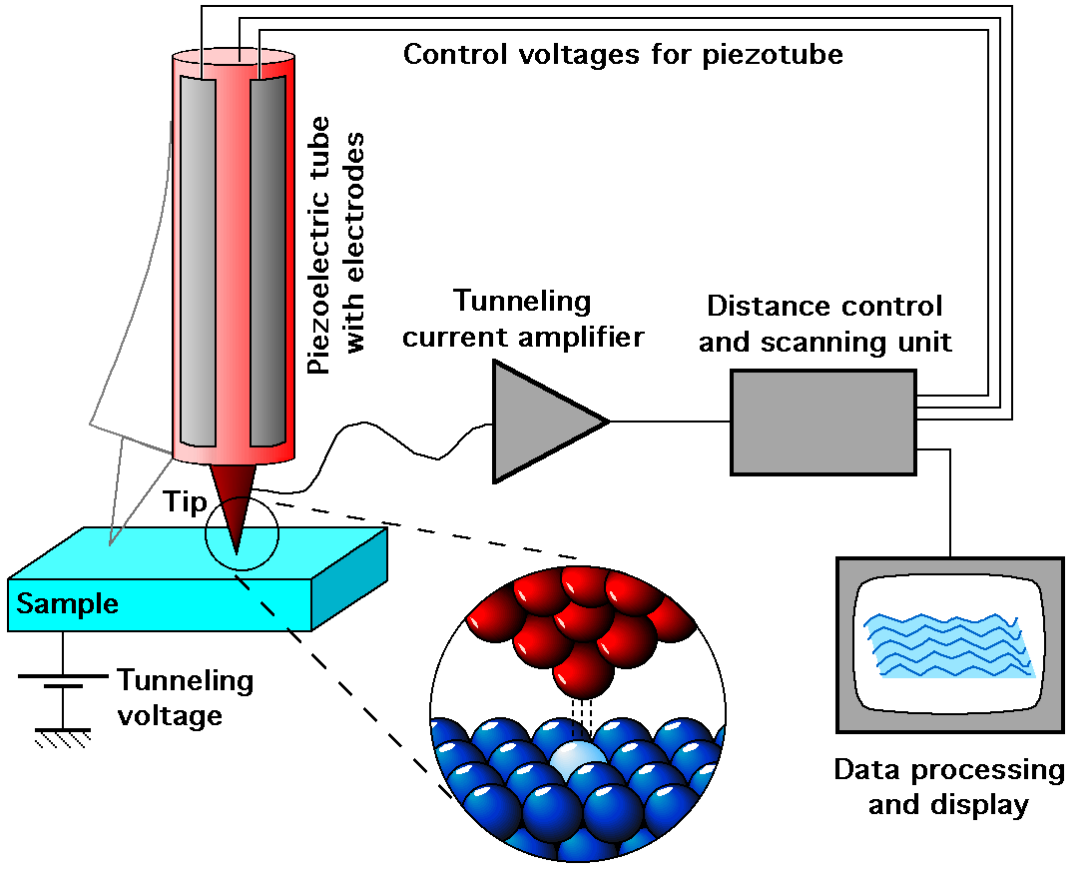

Figure 3.2: Schematics of STM in general, the tip glides over the sample, either controlled by a feedback loop in CCM or in CHM, where only the tunneling current is read out. Cited from [90].

in the first case to move the tip closer to the surface, in the second case in order to interact with the particle). Lateral manipulation has achieved impressive results like quantum corrals [93] or the famous IBM logo made up of single atoms [8].

Thirdly, the tip can induce chemical reactions and generally influence supra- or intramolecular bonds. As in the manipulation techniques outlined above, the tip has to be moved to the particle of interest, after which either a pulse with pre-programmed duration, strength and profile is applied or only specific tip movements are performed. Examples include O_2 bond dissociation on Pt(111) [94], induced tautomerization [95, 96], controlled dissociation of decaborone on Si(111) by inelastic tunneling [97], site-specific manipulation of larger molecules [98] as well as the synthesis of molecules on a surface [99].

3.1.2 Cryostat

The cryostat that keeps the STM at an equilibrium temperature of ~4 K consists of three stages (cf. Fig. 3.3). In an outer part LN_2 at a temperature of ~77 K is used, surrounding an inner part cooled down with LHe, while both are continuously refilled and kept at the respective boiling point of the coolant used under atmospheric pressure. The stages are separated in vacuum and insulated from thermal radiation by metallic shields (gold plated for LHe parts). A separately shielded Joule-Thomson stage (explained below) can cool down the STM to a temperature of ~1.2 K after precooling warmer samples to ~4 K via a thermal bridge, which is especially desirable for spectroscopic uses due to lower thermal broadening.

The Joule-Thomson (Fig. 3.4) stage requires pressurized He, which is precooled by guiding its tube along the LHe bath. The pressurized He can either consist of ^{3}He or ^{4}He, with the first being wildly more expensive than the latter but also allowing for lower temperatures (in the device discussed here, only ^{4}He was used). The gas is further precooled by a counter current heat exchanger after which it is expanded through a nozzle, liquefied and pumped. The liquefied gas is collected in a small reservoir in order to reach a lower equilibrium temperature in the STM. In order to keep additional noise to a minimum, the pump is located in a vibrationally decoupled box. The condensation in this process, or the further loss of temperature due to expansion occurs because of precooling below the inversion temperature, meaning the Joule-Thomson coefficient

$$\mu_{JT} = \left(\frac{\partial T}{\partial P}\right)_H \tag{3.1}$$

has to be positive as temperature and pressure decrease simultaneously. Note that an ideal gas always shows $\mu_{JT} = 0$, yet even helium does not always behave like an ideal gas. Competitive processes enable the loss of thermal energy when the pressure is lowered while maintaining the total energy under steady state conditions.

Consider particles moving in the attractive region of the Lennard-Jones potential at already low temperatures. Larger interparticular distances after expansion lead to higher potential energy which in turn lowers the kinetic energy and therefore also the temperature in the system as enthalpy is conserved.

At higher temperatures, frequent particle collisions lead to more particles in the repulsive region of the potential, also increasing potential energy and lowering kinetic energy. Expan-

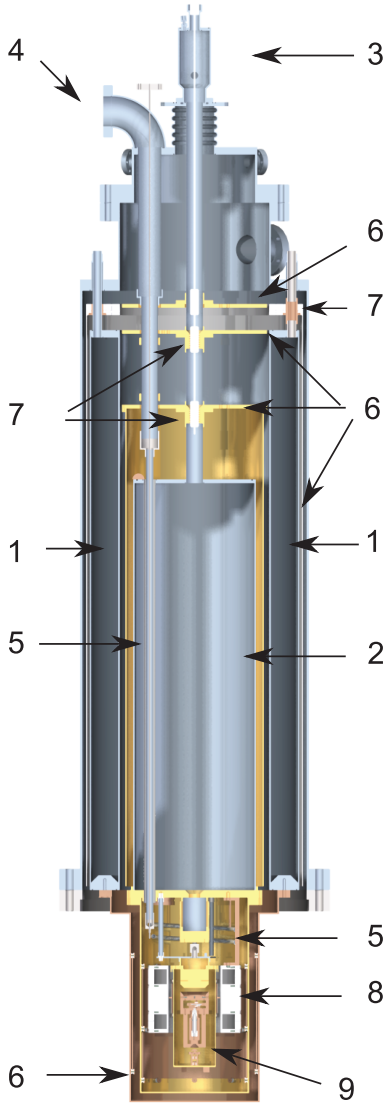

Figure 3.3: Scheme of the cryostat. (1) Liquid nitrogen tank, (2) liquid helium tank, (3) in- and outlet of liquid helium, (4) in- and outlet of He gas, (5) countercurrent heat exchanger for He, (6) radiation shield, (7) heat exchangers coupled with cryogenic gas, (8) superconductive coil, and (9) microscope head. Cited from [89].

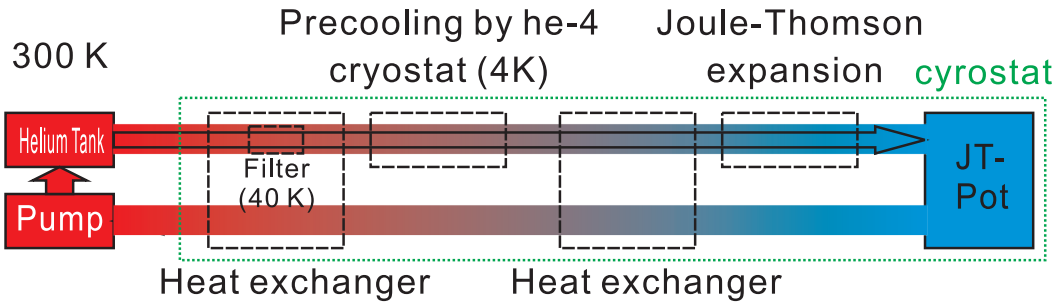

Figure 3.4: Scheme of the He-cycle in the JT-cryostat. Cited from [89].

sion here will cause less repulsion, leading to lower potential energy. With the overall energy conserved, this means higher kinetic energy and thereby higher temperature [100].

From the argument above, it becomes clear that the gas simply has to be cooled down beyond a point after which effect 1 wins out against after effect 2.

A magnet depicted in Fig. 3.3 was not used. Instead, eddy current damping was employed in addition to the three springs that vibrationally insulate the STM head from the Joule-Thomson cryostat.

3.1.3 Chamber Setup

The vacuum chamber containing the STM (Fig. 3.5) is subdivided into an STM part and a preparation part, separated by a large valve in order to allow the transfer of samples via a manipulator arm. While the preparation and the STM chamber are equipped with an ion getter pump (details below), only the preparation chamber is pumped with turbo molecular pumps and a membrane pump, which means that for initial operation, the STM part has to be pumped through the preparation part. Venting the system or parts of it will usually (depending on the volume and sensitivity of e. g. molecules in an OMBE (organic molecular beam evaporator, see below) require a bakeout of the system above 100°C for ca. 48 h in order to remove residual water etc. Afterwards, the valve usually stays closed whenever possible to avoid contamination of the STM due to preparation processes (c. f. below) and solely the STM ion pump and the cryostat (as a cold trap) hold the pressure. The preparation chamber can be shut off from the pumping system with access to the preparation ion pump maintained, so that pumps causing vibration can be deactivated during STM scanning or spectroscopy, on the other hand a valve to the preparation chamber ion pump can be shut in case preparation procedures cause relatively high pressure (above 10^{-8} mbar).

The STM and preparation chambers are equipped with several add-ons which can be fitted to the body, often with valves so that add-ons can be changed or removed without venting the chamber. For the STM chamber possible add-ons include a Co-evaporator and a quartz window through which in-situ UV-laser irradiation is possible. Sample transfer (and storage in garages attached to the LN2 shield) and cryostat operation (opening/closing the shields and the thermal bridge) is enabled by two wobble sticks, magnetically operated sticks of which

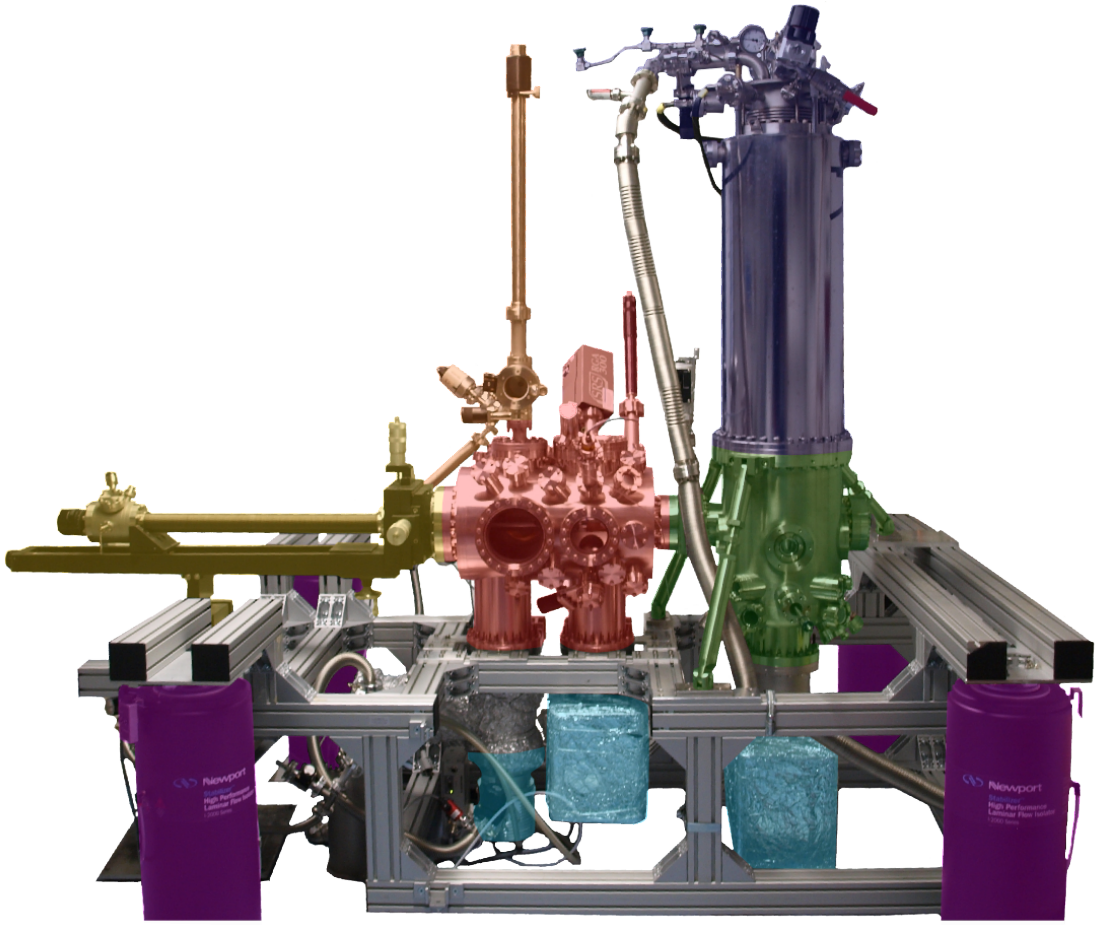

Figure 3.5: Overview of the vacuum chamber. (green) STM chamber, (dark blue) cryostat, (red) preparation chamber, (yellow) manipulator, (light blue) pumping system, (orange) load lock and (violet) external vibration isolation. Cited from [101].

one is equipped with a gripper. The preparation chamber features a vertically operated load-lock system which allows sample transfer between atmosphere and vacuum without venting the whole system through an extra manipulator (operated magnetically) with access to the main manipulator, which is mechanically maneuvered in x-, y- and z-direction, with an x/y-range of several cm and a z-range of ca. 70 cm. The main manipulator can be cooled down to around 100 K by a flux of LN2 and heated up to more than 770 K with a built in tungsten filament. Temperature of manipulator and sample are monitored by two thermocouple contacts, each consisting of two different conductors producing a potential difference due to the thermoelectric effect which can be translated into a temperature. Their signals can be utilized by a heating feedback loop. Mechanical and electrical feedthroughs ensure these functions. The main manipulator also has a second, higher position in order to facilitate certain transfer operations and avoid sputtered off particles of the sample holder on the sample (see preparation). Add-ons to the chamber include a commercial SPECS ion gun, two organic molecular beam evaporators (OMBE), a Ho-evaporator (not used for the experiments presented here), a residual gas analyzer (RGA) as well as a low-energy-electron-diffraction system (LEED, not used in here either). OMBEs comprise three inert quartz crucibles in which the particles to be evaporated are stored (atoms or molecules), evaporation is induced by heat produced from resistive heating while the rest of the device is cooled with water. The temperature is either measured directly with thermocouples or by a calibration using the resistance of the heating wire.

The whole system (STM and preparation) can be lifted from the ground in order to float freely on vibrationally isolating Newport laminar flow stabilizers. The STM features a second isolation system, as during scanning it is suspended on three springs made of a low-temperature optimized metal alloy.

3.1.4 Pumps

A controlled preparation of clean samples and samples that contain only the materials they were treated with deliberately requires a very low base pressure (~10^{-10} mbar), which is achieved by the usage of several stages and types of pumps.

A membrane pump serves as the first stage. The principle is comparable to a lung, just that the air will not leave the same way it entered. As the name suggests, a membrane is operated in order to suck in and expel air, directionality is achieved by valves that prohibit air flow back into the chamber. The method is operated oil-free, a desired quality for vacuum systems due to possible problems with contamination by residual oil, and reaches a pressure of ~1 mbar.

A membrane pump lowers the pressure far enough, so that turbomolecular pumps (TMP) can be operated. The composition is similar to a turbine. Rotors (at frequencies of up to c. 1.5 kHz) and stators are arranged in a way so that particles are accelerated towards the exhaust. Low pressure is a requirement as a high mean free path for the particles is required within this principle and because high rotation frequencies are impossible in a high pressure environment. In the system at hand, two such pumps are used, one achieving a pressure of ~10^{-7} mbar, the other ~10^{-10} mbar. For the latter pressure, a bakeout in which the whole system is pumped and held at a relatively high temperature (beyond 100°C) for some time is necessary.

Additionally, both sub-chambers are equipped with ion getter pumps, where a strong electric

field ionizes particles and drives them into titanium plates. An exposure to high pressure should be avoided, as without the addition of protective measures flashovers or premature aging could occur. Such pumps are also relatively ineffective when pumping noble gases, as inert gases cannot easily be buried in titanium.

Two other pumping mechanisms are present in the system. In the STM chamber the cryostat acts as a cold trap, adsorbed particles are usually only released when the cryostat or parts of it warm up (which is also the reason why the STM/preparation valve should be opened when warming up the cryostat). An additional system in the preparation chamber that sublimates titanium from filaments into the recipient (titanium sublimation pump, TSP) assists with capturing residual particles, which will stick to the titanium, which in turn will stick to the chamber.

3.2 Preparation Process

As the preparation process is nearly the same for any UHV system, independent of the investigation technique, it is discussed separate from the STM system. In this work, only metal single crystals were used as substrate materials, for which the cleaning procedure consists of multiple cycles of sputtering and annealing. In semiconductors the material is harder and the surface would be restored by a cleaving process.

When the sample is sputtered, this means it is bombarded with Ar^+ ions produced and accelerated by a sputtergun. Common values for sputtering are a kinetic energy of ~1 keV, a pressure of ~10^{-6} mbar, a sputtering current of ~10 μA and a duration of ~20 min. Ionization is achieved by either permanent plasma discharge or thermally emitted electrons with a kinetic energy of 100 eV (maximum of the ionization cross section), after which the ions are emitted through a negatively charged extractor slit. Sputtering roughens up the surface and thereby removes adsorbed particles and some layers of substrate atom.

This roughing up is remedied by subsequent annealing. During annealing, the sample is heated up (to about 500 °C for 15 min for Ag(111)) and kept at the maximum temperature for a few minutes ($5 - 15$), due to which crystal defects are healed and remaining ions from sputtering are desorbed. The sample can either be heated up simply by applying a current to the filament but also by additionally applying a high voltage between sample and filament. For annealing metal surfaces, high voltage turned out to be unnecessary and was not used, for a sample with adsorbates, HV was never used due to the possible degradation of molecules and supramolecular structures due to accelerated electrons.

When a clean surface is available, the evaporation process is initiated. For the materials here, (O)MBE was employed. For harder materials, atoms are directly sputtered off rods. In the case here, chemicals were evaporated as powder from a Knudsen cell, as it is commonly found in an OMBE. Before evaporation, the cell is pre-cooled with water in order achieve a stable thermal environment, whereafter the evaporator is heated and brought into thermal equilibrium. A shutter enables temporally precise dosing of molecules. Often, the sample is kept at a certain temperature by simultaneously cooling it with LN2 and heating it with the filament.

For the adsorption itself, two different variants can be distinguished. The most important difference is observed between physisorption and chemisorption, while mixed forms exist [102].

Physisorption is characterized by van der Waals forces between substrate and adsorbate. This leads to comparatively low binding energies of 5-10 meV and substrate-adsorbate distances of 3-4 Å [103]. In case of dominant or pure physisorptive bonding, the thermal energy $k_B T$ already reaches ≈ 25 meV at room temperature, requiring a cold substrate to avoid desorption. Physisorption is generally reversible, the adsorbate remains chemically intact and can serve as a precursor to chemisorption [104].

The case is different for chemisorption in which bonding to the substrate occurs, leading to hybrid orbitals. Thereby, charge transfers occur that can initiate molecular dissociation and is also of interest in heterogeneous catalysis, e. g. the CO to CO_2 conversion [105]. Here, binding energies of around 1 eV for ionic or covalent bonds are typically observed, which also implies shorter substrate-adsorbate distances. Furthermore, chemisorptive bonds are not necessarily reversible and also often show a preference for specific binding sites combined with an aversion for multilayer adsorption (as the second layer is necessarily only bonded to the adsorbates of the first layer, often via physisorption, and not to the substrate).

A mathematical description of the adsorption rate $\mathrm{d}\theta/\mathrm{d}t$ is possible when neglecting desorption (which is equivalent to assuming low temperatures) by formulating [106]

$$\frac{\mathrm{d}\theta}{\mathrm{d}t} = \frac{p_A}{n_a \sqrt{2\pi k_B T}} S(\theta) e^{-E_A/k_B T}, \tag{3.2}$$

with the rate of particles colliding with the surface $p_A/\sqrt{2\pi k_B T}$ as derived from kinetic gas theory with the temperature T and the pressure of species A p_A, divided by the area density of adsorption sites n_a, multiplied by the sticking coefficient $S(\theta)$ and an Arrhenius term for taking into account an activation energy. The sticking coefficient deserves closer scrutiny, as it changes with the order (number of adsorption sites per particle) of adsorption. First order sticking coefficients will correlate with $(1-\theta)$, while the general proportionality for order q is $S(\theta) \propto (1-\theta)^q$. A constant sticking coefficient is set for systems in which substrate and adsorbate are the same material.

3.3 XPS Setup

The XPS setup used for the data in this work employed X-rays from a laboratory source (Mg or Al anodes that emit most of their photons at one distinct energy, K_α), while for the most precise measurement usually synchrotron light in conjunction with a monochromator would be utilized. The photoelectrons' kinetic energy is detected after leaving the sample in a hemispherical analyzer (commercial product by SPECS). Electrons traversing the analyzer, which consists of two hemispherical electrodes with potential difference ΔV and radii R_1 and R_2, have to match a set pass energy, otherwise they will not pass through an exit slit and cannot be detected. The kinetic pass energy is determined by the parameters of the analyzer as follows

$$E_{kin} = e\Delta V \left(\frac{R_1 R_2}{R_2^2 - R_1^2} \right). \tag{3.3}$$

In order to measure a spectrum with fixed photon energy, a varying retarding voltage slows the electrons down before entering the analyzer; after selecting them for their pass energy, the

electrons are detected by a channeltron and counted. UHV is necessary to guarantee a large free path for the electrons.

In case a monochromator is used (especially at synchrotron facilities), it is usually based on single crystal diffraction governed by the Bragg condition [71]

$$n\lambda = 2d\sin(\theta), \tag{3.4}$$

which states that the reflection angle θ of order n of a certain wavelength λ depends on the crystal lattice spacing d. Qualitatively, the Bragg condition is a result of constructive and destructive interference of wavelength. Often, for lab sources it is more convenient not to use a monochromator as the beam intensity will decrease and many or most of the emitted photons from a material have the energy of the dominant transition anyway. While the descriptions for the STM preparation chamber and procedure, pumps, etc. still apply, it ought to be noted that the system was not subdivided into a preparation and analysis chamber. The binding energy was calibrated against the Ag $3d_{5/2}$ peak of Ag(111).

3.4 TPD Setup

TPD was carried out in the same chamber as XPS. For TPD measurements, the sample was approached to a Feulner Cap [107] in order to ensure that only the signal from the sample was measured. The sample was then heated at a constant rate of 0.5 K/s while a quadrupole mass spectrometer recorded any molecular fragments that left the sample. Low pressure was maintained through an LN2 cold trap in combination with a titanium sublimation pump. For a general description of the adsorption/desorption process, see the relevant section above.

3.5 NEXAFS Setup

NEXAFS experiments were carried out at the HE-SGM beam line at BESSY II in Berlin. The setup used is a commercial arrangement built by PREVAC, consisting of – again – similar components as other system, including a preparation and analysis chamber, yet is also equipped with a dedicated transfer chamber. Linearly polarized X-ray light was obtained from a dipole magnet, resulting in a broad range of available photon energies. While such light is not as bright as that of an undulator, it also causes less beam damage. Still, the area on the sample that was analyzed was varied with each measurement. Angle-dependent absorption spectra were recorded at 25°, 53° and 90° (angle between $\mathbf{E}$ and the surface normal) for the bare surface and the sample. All presented spectra are difference spectra divided by the energy dependent transmission function of the photon flux and then normalized to an edge jump of one. A retarding voltage of -150 V was used for the K-edge spectra.

4 F1-DETP on Ag(111)

4.1 Molecule and Reaction

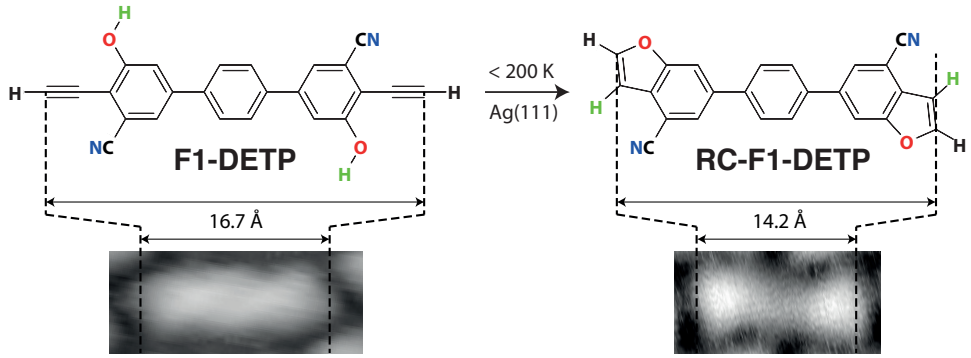

Figure 4.1: F1-DETP and its product RC-F1-DETP. RC denotes the ring-closed state of the product. Some atoms are color-coded to highlight their role, while typical STM topographs are given for reactant and product, together with a length comparison. Adapted from [108]. Copyright Wiley-VCH Verlag GmbH & Co. KGaA. Reproduced with permission (as is applicable to all other adaptations from this article in this work).

The molecule shown in Fig. 4.1 on the left hand side was used in a primary round of experiments. It consists of a terphenyl backbone and is functionalized with a hydroxyl group, a carbonitrile group and a terminal ethynyl group at both ends. In the following, the reaction shown above is validated and its features are unraveled. However, in order to show the significance of such an intramolecular hydroalkoxylation reaction, which leads to a furan-like ring closure (right panel), several introductory remarks and a description of the most important features of the process have to be given.

The reaction mechanism proposed here, a proton tunneling-induced, intramolecular hydroalkoxylation, as has been mentioned in the introduction, is enabled by a proton tunneling step (the H atom marked green). While (proton) tunneling is not unknown as an effect in chemical reactions, as early works by Hund (1927 [109]) and Ronald P. Bell (1933 [29]) show, its influence and significance in reaction mechanisms is often underestimated. However, over the course of the past 100 years, several important effects in biology [31–33] and low activation energy (e. g. interstellar) settings [34,35] have been noticed. And while, as already pointed out earlier, it has not been ignored in surface science [37,38,110,111], it has not yet been linked to

bottom-up nanoconstruction. With this thesis, a non-reversible reaction dominated by a tunneling step shall be presented, which has all the necessary ingredients for such a leap. While the reaction itself is intramolecular, a change of the on-surface domain structure can already be shown, as will be lined out in the next section. This process has a very low onset temperature, below 200 K, which is important since with an increase in activation energy, an increase in side reactions is to be expected. For obvious reasons, the absence of side reactions is a desirable ingredient in the targeted manipulation of matter. On the other hand, while some tunneling reactions can occur at *any* temperature, the process at hand requires a preliminary, thermally activated state, from which it can continue. This trigger is also quite important for 2D bottom-up synthesis and shall be lined out below as well. Finally, even though the reaction at hand is intramolecular, it may serve as an inspiration for the synthesis of covalent on-surface structures, prealigned through intermolecular forces and joined by low-activation-energy tunneling reactions.

The molecules used here were synthesized by Ping Du and Svetlana Klyatskaya from KIT, the synthesis is described in the methods of [108]. Data presented in the following shall show the molecule and its behavior under STM, NEXAFS, XPS, TPD and force-field investigations in order to corroborate the above assumptions. A cross-check with a deuterated molecule and a final discussion then follow in the next chapter. The evaporation temperature from the quartz crucible was around 200°C (varying depending on the configuration and powder content of the crucible) with evaporation times of a few seconds up to a few minutes, depending on the desired coverage. Unless otherwise noted, the molecules were always evaporated onto a cold, clean surface (cooled with LN2 to around 100 K) and then annealed for 10 minutes for each temperature step. In order to ensure that the molecule (and not its product) was evaporated, a preliminary evaporation experiment was carried out, after which nuclear magnetic resonance (NMR) confirmed that the molecule was still intact after evaporation.

Preliminary findings from my M. Sc. thesis [112] have contributed to this chapter, however a new analysis and new data is provided.

4.2 STM Investigation

The STM investigation is presented as a series of annealing steps from low to high temperatures. Originally, starting with a very cold sample was inspired by STM data showing mixed molecular phases (cf. intermediate temperature), which eventually led to the conclusion that these different phases consist of different molecules, which are not impurities but instead products achieved after adsorption.

4.2.1 Low Temperature

At low temperatures, meaning the lowest possible temperature in the STM system at 100 K (achieved with LN2 manipulator cooling), the molecules are observed to form small islands without a noticeable long-range order due to limited diffusion. The STM topograph (Fig. 4.2, with juxtaposed molecular model without STM data) is overlayed with F1-DETP molecules[1] in

[1]The molecular model was calculated with HyperChem [113] via semi-empiric methods.

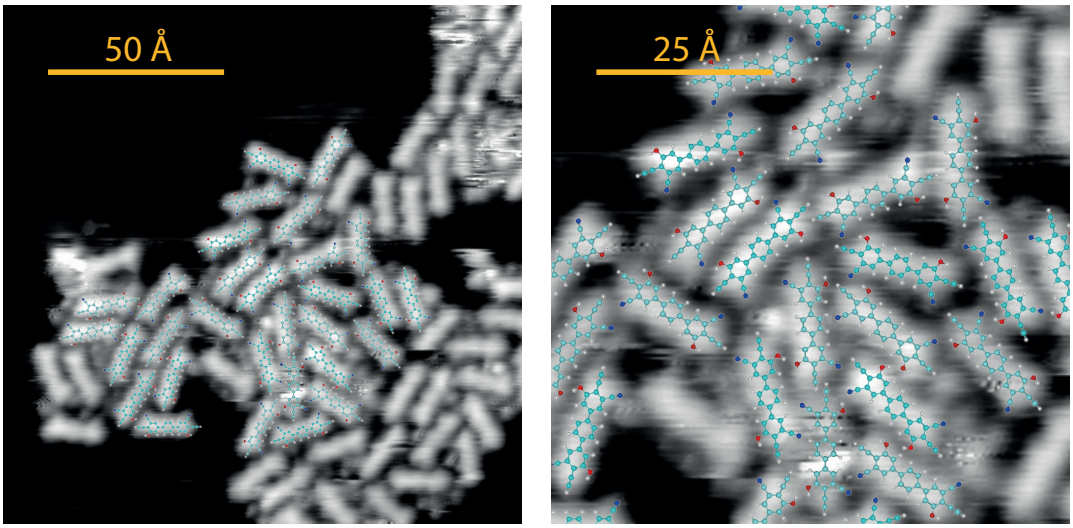

Figure 4.2: STM topograph of F1-DETP at low temperature (annealed to only 100 K, zoom-in on the right). The image has been corrected for drift of the piezo scanner. Setpoint: $V_B = -0.5$ V, $I_T = 20$ pA. Adapted from [108].

order to show that the reactants of the proposed reaction fit to the experimentally obtained data without steric hindrance. OH and CN groups have been arranged plausibly, i. e. in ways that take into account their preferred configuration when (electrostatic) intermolecular forces are taken into account. Both, trans and cis isomers are present in the fit.

4.2.2 Intermediate Temperature

At intermediate temperatures (here 250 K, Fig. 4.3) from 200 K up to 300 K a coexistence of two phases (marked S for snake and Z for zig-zag) was observed. In principle, several reasons can lead to such a phenomenon; coverage dependent phase formation is fairly common [104], while other options, such as gradual deprotonation [105] or a metastable assembly also possibly lead to such results. Here, it is argued that no other reason but the presented reaction causes the observation above, which leads to consequences once the wide temperature range of this coexistence is taken into account. Evidence presented in this section will focus on plausible fits that take into account steric hindrance and intermolecular forces. Returning to the consequence, it ought to be stated that the wide temperature range in which this occurrence is possible leads to the assumption that the reaction rate is nearly constant with respect to temperature over said range, which contradicts the Arrhenius-like behavior of normal reactions and leads to the assumption of a tunneling process (as a rate determining step).

All of the above-mentioned aspects will be further discussed and corroborated in the following sections but first, a thorough analysis of both phases is necessary. A zoom into the Z- and S-phase is provided in Figs. 4.4 and 4.5 below. For the Z-phase, very strong electrostatic intermolecular bonds stabilize the assembly, which are denoted as α, β and γ in Fig. 4.4 b, rep-

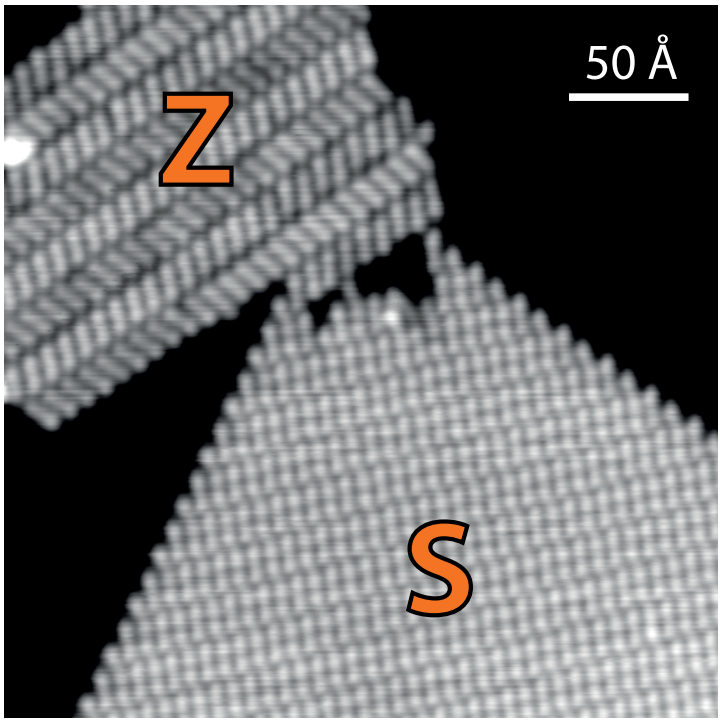

Figure 4.3: Typical STM topograph at intermediate temperatures (here annealed to 250 K, Set-point $V_B = -1.0$ V, $I_T = 100$ pA). While only one molecule was deposited, two phases are observed, Z and S. Adapted from [108].

resenting the OH-NC bond, a hydrogen bond between C-H and O and an interaction between CN and CCH, respectively. The fit reveals slightly smaller intermolecular distances for α and β of about 2.0-3.0 Å than literature values [114, 115], yet the comparison is still quite favorable, especially when considering that the literature here does not take into account surface effects. A higher distance of 3.2-3.3 Å is found for γ, justifying the assumption that it is less important for the formation of this structure. A very good agreement with the force-field simulations is achieved (see below).

On the other hand, the S-phase is mainly governed by the interactions between the CN group and neighboring aromatic rings (blue dashed ellipse in Fig. 4.5 b), which might amount to a proton-acceptor ring interaction [116]. A simulation of similar molecules on the same surface revealed an N-H distance of around 2.4 Å, which corresponds almost perfectly to fit values of 2.0-3.0 Å [117]. A minor role probably belongs to the interactions between the furanic moiety and the next aromatic ring (red ellipse). The force-field simulation again compares favorably.

Finally, some words should be spent on details of the preparation process and why the STM data already implies a reactant/product relationship between the constituents of Z- and S-domains. As has already been pointed out above, preevaporation experiments make it highly unlikely that more than one species was in the crucible. Further purification was achieved by

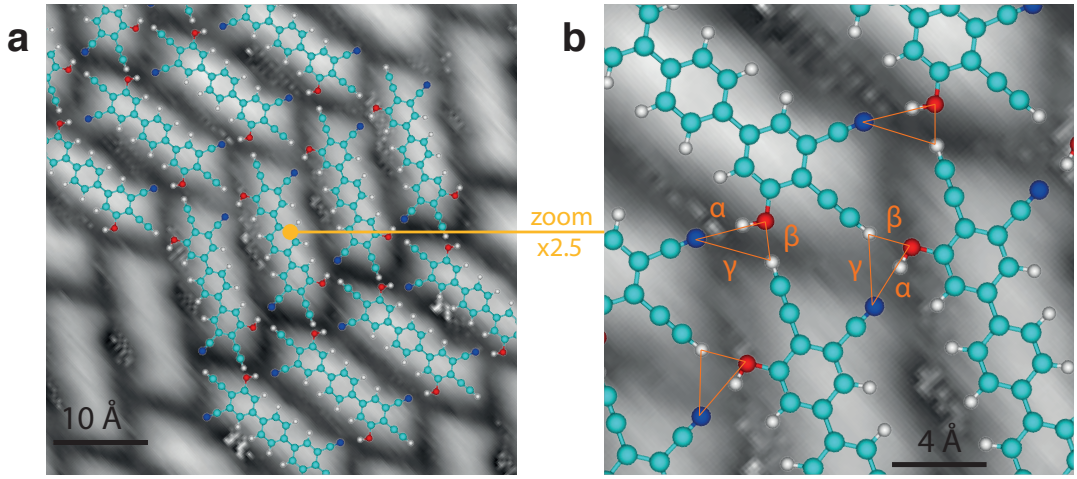

Figure 4.4: A closer look into the Z-phase with a superimposed molecular model (a) and a zoom-in in order to show its intermolecular bonding scheme (Setpoint $V_B = -0.3$ V, $I_T = 100$ pA). Adapted from [108].

careful degassing and a comparatively high evaporation temperature of ca. 200°C. Deprotonation will be discussed in the XPS and TPD subsections but from experience a deprotonation without a change of contrast in the STM topograph seems relatively unlikely. Moreover, the intact molecules are too long to be fitted to the S-phase (see subsection about unit cell). Metastable assemblies were excluded due to prior experience with similar tectons [118]. Since both domains were present in submonolayer coverage, a coverage dependent phase formation is not assumed either.

4.2.3 High Temperature

With the exception of some minority species by-product occurring at very high temperatures, after a certain annealing temperature (about 350 K), only the S-phase is observed. This allows for the analysis of a reference state via XPS and NEXAFS, meaning that the signal in these space-averaging techniques will correspond exactly to the S-phase, which enables an easier interpretation of mixed domain sample signals.

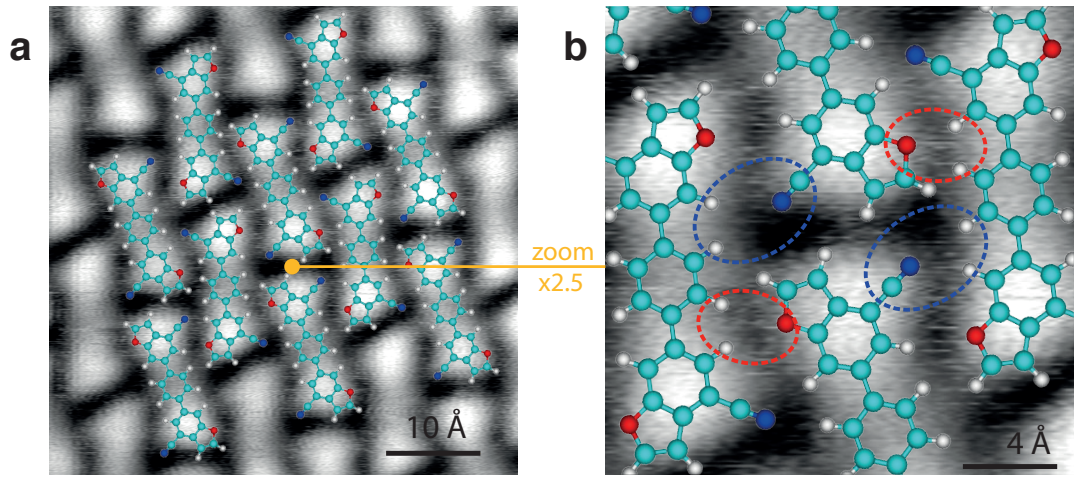

Figure 4.5: A closer look into the S-phase with a superimposed molecular model (a) and a zoom-in in order to show its intermolecular bonding scheme (Setpoint $V_B = 10$ mV, $I_T = 50$ pA). Adapted from [108].

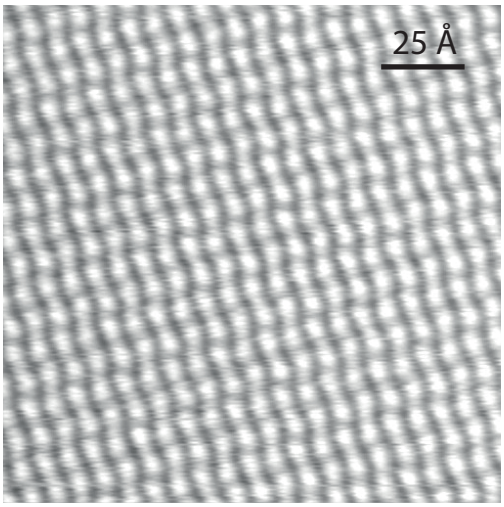

Figure 4.6: F1-DETP annealed to higher temperature (400 K, Setpoint $V_B = -1.0$ V, $I_T = 30$ pA). Only the Z-phase is observed for higher annealing temperatures. Adapted from [108].

4.2.4 Unit Cell Analysis and Steric Hindrance

Fig. 4.7 shows the experimental unit cells of both, the S- (a) and Z-domain (b) revealing a bimolecular unit cell for both phases. The lengths and angles given are derived from a statistical analysis, note the good agreement with simulated data (below). The unit cell and Ag(111) high symmetry directions are indicated, angles are given with respect to a horizontal line. Note that the unit cell in the S-phase is bimolecular, because the molecules of adjacent rows are turned by about 180°, as shown in the previous subsection.

Fig. 4.7 c and d show attempts to fit the intact molecules onto S-phase topographs. This represents the immediate (and chronologically first) piece of evidence that the S-phase does presumably not consist of intact molecules, as they would be too long and the intermolecular distances between atoms would become too short (red ellipse markers), therefore steric hindrance would be expected. This point of view is further corroborated in the XPS/NEXAFS sections.

4.3 Force-field Simulations

The force-field simulations achieved with CHARMM (description in theory chapter) are shown in Figs. 4.8 and 4.9. As an introductory remark, the force-field simulation is based on a pre-aligned sample, the position of the silver atoms was fixed and temperature effects were not taken into account.

When compared to the experimental data in Fig. 4.7, exceptionally good accordance between the two is observed. With regard to the Z-phase, the long unit cell vector is only 6 % longer than in the experimental data (35.8 Å vs. 33.7 Å). An even smaller deviation is observed for the short unit cell vector, which is 8.8 Å in the simulation, only 0.2 Å longer than expected from experimental data. The angle of 92° is found in both, simulated and experimental data. The α and β interactions, as defined in the STM section, which are of paramount importance for the binding motif, appear only with slightly longer (about 1 Å) distances between the involved moieties.

With regard to the S-phase, the bimolecular unit cell deduced from experimental data is confirmed. Unit cell vector lengths deviate by less than 3 % from experimental data, again the calculated cell is slightly larger than the experimentally derived model. Angles deviate by 3°. In both cases (S and Z) even the alignment of the molecules with respect to the high symmetry direction corresponds to experimental data.

In conclusion, the CHARMM force-field simulations confirm the experimental models and deductions.

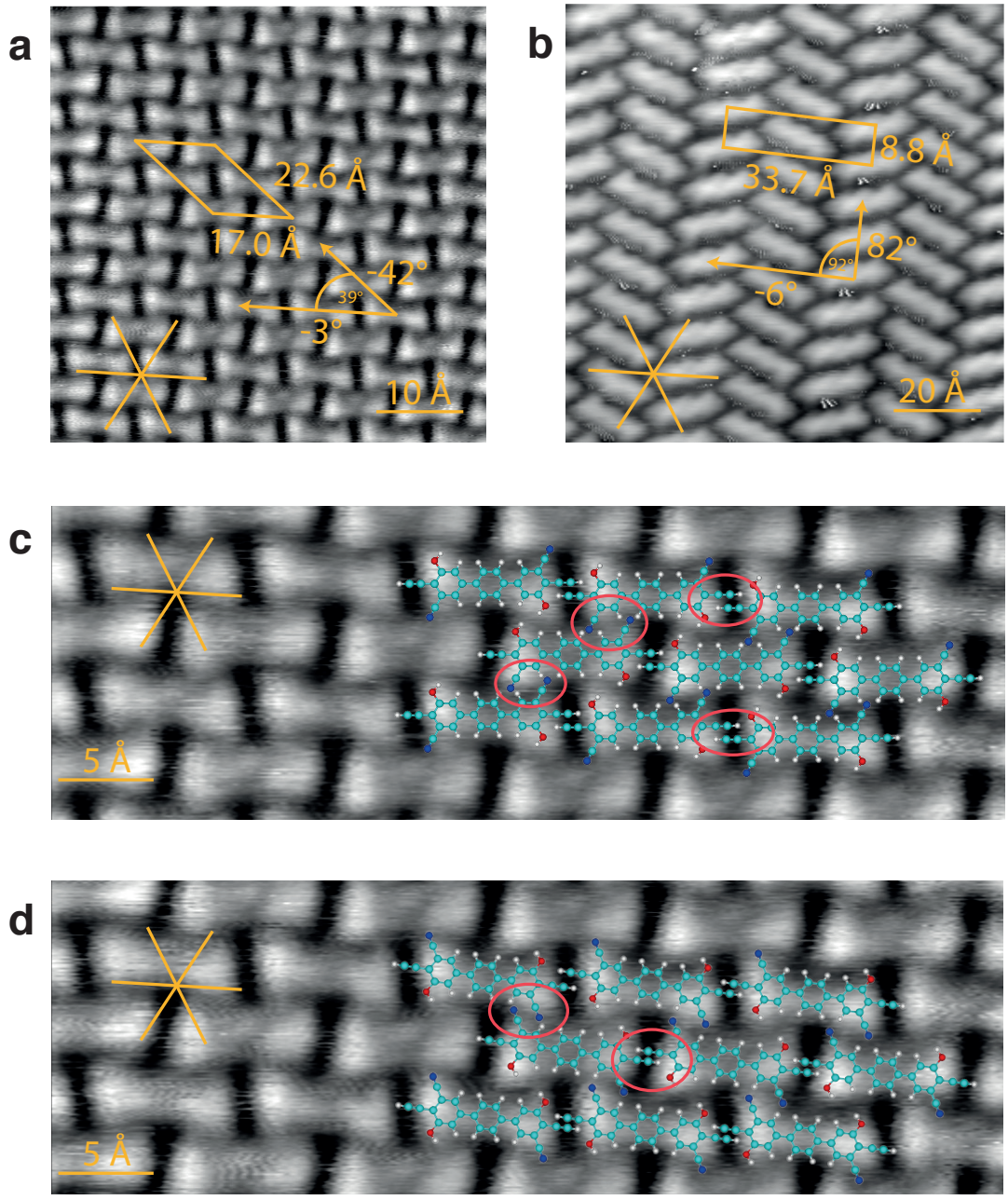

Figure 4.7: The different unit cells of RC-F1-DETP (S-phase, a and F1-DETP (Z-Phase, b) along with the high symmetry directions of Ag(111), together with two options for trying to fit the intact molecule to the S-phase (c, d). Setpoints: a/c/d $V_B = 216$ mV, $I_T = 100$ pA, b $V_B = -0.3$ V, $I_T = 100$ pA. Adapted from [108].

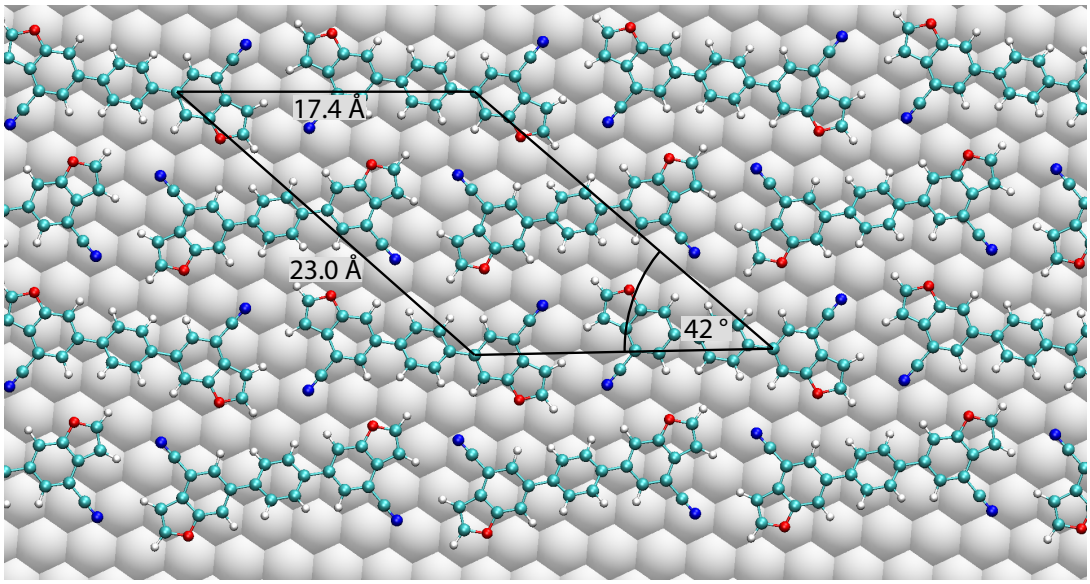

Figure 4.8: F1-DETP force-field simulation intact with unit cell. Adapted from [108].

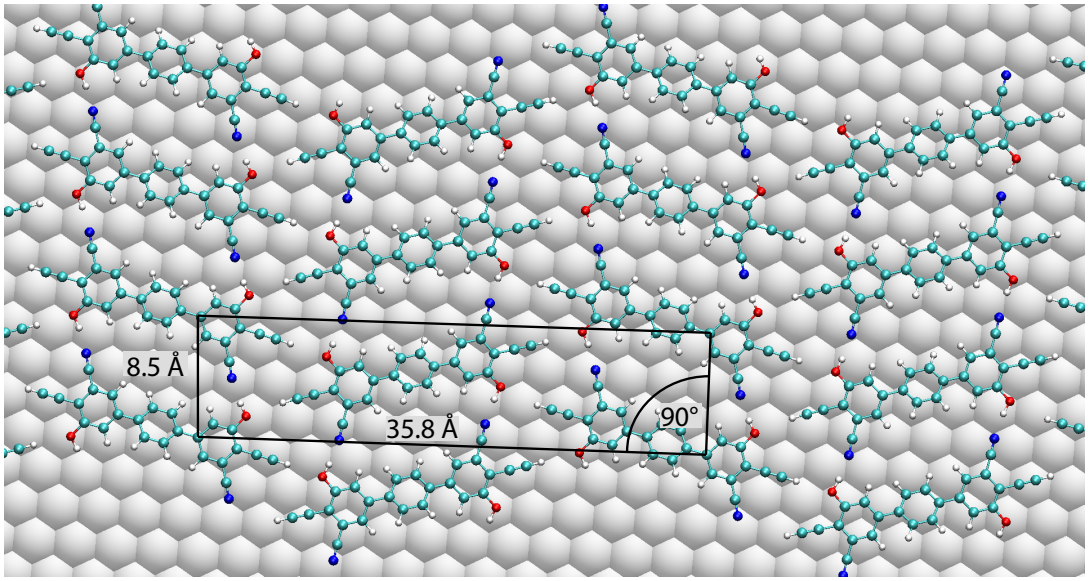

Figure 4.9: F1-DETP force-field simulation ring-closed with unit cell. Adapted from [108].

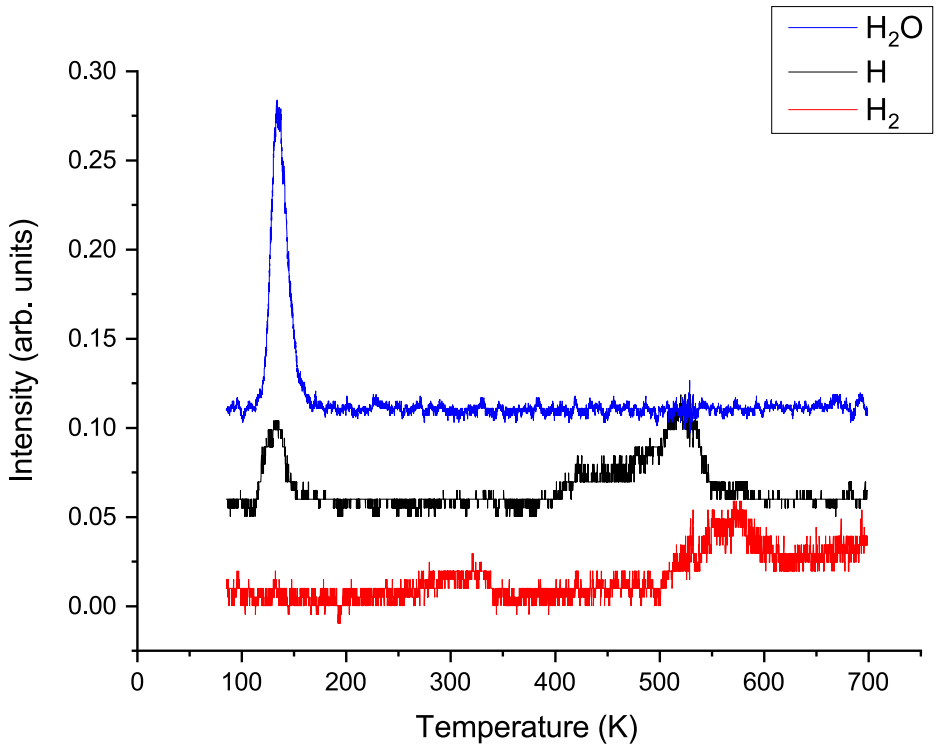

Figure 4.10: F1-DETP TPD verifying that neither H nor H2 leaves the surface, while some crystal water desorption is observed. Curves are vertically offset for clarity. Adapted from [108].

4.4 TPD

TPD experiments were necessary in order to confirm that rate estimations originating from either STM data or XPS data was not affected by desorption and that the originally proposed reaction mechanism could be upheld. With regard to these issues, it could be established that none of the molecular fragments (neither for multilayers nor for monolayers) leave the substrate before the onset of the reaction. For monolayers, no molecular fragment desorbs before the molecules are fully converted to the product at around 350 K (this is also confirmed by XPS data, as combined peak areas stay roughly the same). In particular, one of the most obvious options for a chemical change of F1-DETP on the substrate would be a deprotonation reaction. Since H or H_2 would not be stable on the surface, it would have been detected in the mass spectrometer in the relevant temperature range (before the onset at ca. 200 K). This is not the case, at least between 200 K and 250 K, both curves are flat (cf. Fig. 4.10). The water peak below 150 K was caused by crystal water in the hygroscopic powder, which was not removable prior to evaporation, the H peak in this temperature range is caused by dissociated water. Therefore, the TPD experiments reveal that deprotonation in this case is highly unlikely and that desorption is a relatively unimportant effect in the relevant temperature range (for

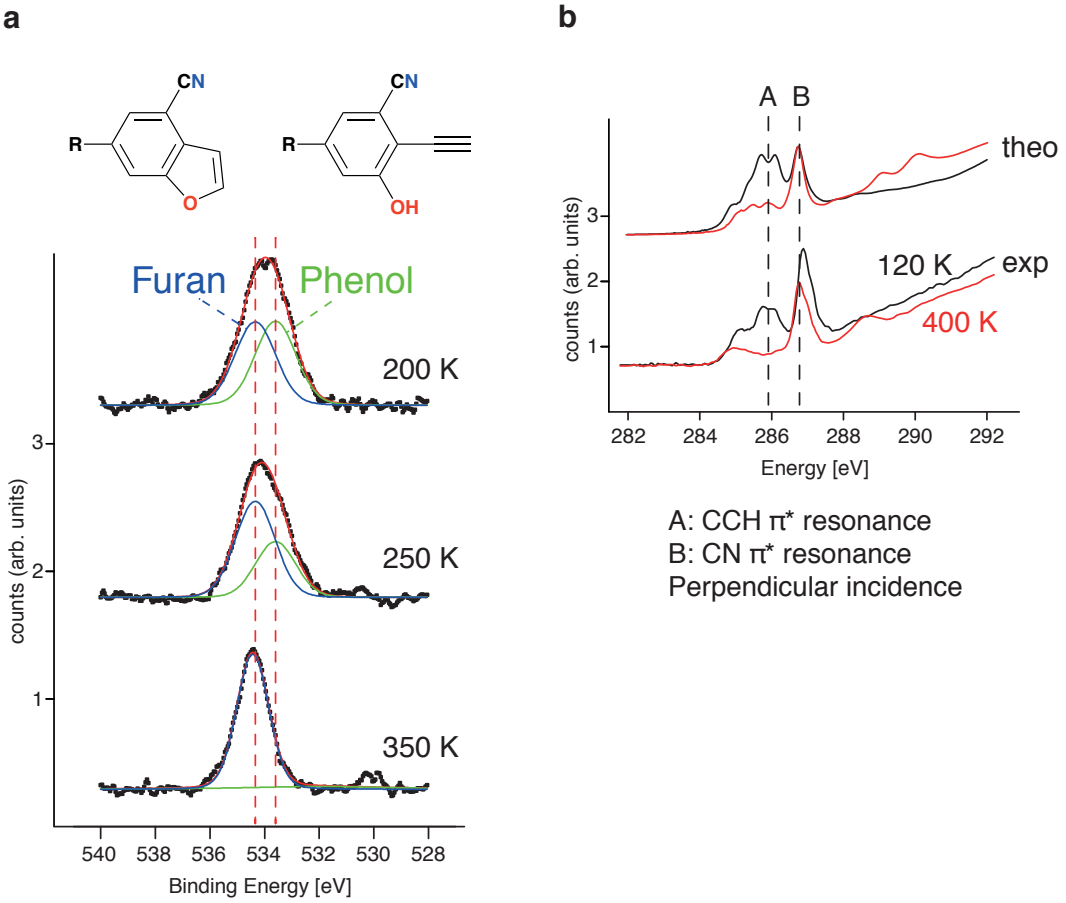

Figure 4.11: F1-DETP XPS O 1s (a) and NEXAFS C K-edge Annealing (b) Comparison. Adapted from [108].

submonolayers).

4.5 XPS and NEXAFS Investigation

Evidence for the proposed reaction is introduced here with two separate, space averaging techniques, with the second also being utilized in order to show the orientation of F1-DETP on the surface. The comparison to theoretical models is based on the work of Mateusz Paszkiewicz, while the author of this work was only involved in gaining the experimental data presented.

Starting with Fig. 4.11 a, the O 1s signature for an annealing series for F1-DETP on Ag(111) is shown and two peaks, one assigned to the furanic (product), the other assigned to the phenolic molecule (reactant) are fitted at a binding energy of 533.6 eV and 534.3 eV, respectively. This identification is based on literature values for similar molecules on Ag surfaces [119–121]. As can be concluded from the graphics, at 200 K furanic and phenolic species are still both present.

However, the ratio at 250 K clearly favors the furanic species until the phenolic species is not observed anymore at 350 K. The situations for temperatures below 200 K are not depicted due to the problem with crystal water (see TPD section above), from 200 K onwards water should have completely desorbed from the surface. A deprotonation, as would be indicated by prominent features between 530 eV and 532 eV under similar conditions, is again excluded [122, 123].

NEXAFS experiments clarified the adsorption geometry of F1-DETP (Fig. 4.12) and also confirmed the XPS results (Fig. 4.11 b). This is due to the fact that after annealing, the CCH resonance nearly vanishes for its most favorable incidence angle (90°) to the surface, which indicates that a change has occurred in the CC bond, while on the other hand, the resonance assigned to CN does not change significantly. A comparison between theoretical and experimental C K-edge data (Fig. 4.12 a<->c and b<->d) reveals that the molecules lie nearly flat on the surface (note the preserved dichroism at 285 eV before and after annealing). Due to the peak assignment and superposition of the curves for the theoretically calculated NEXAFS spectra, features A and B can clearly be assigned to CCH and CN, even with a visible double structure in the case of A. Together with previous experimental and simulation data, this confirms the proposed reaction from F1-DETP to RC-F1-DETP.

4.6 Conformational Protection

An intriguing effect was encountered when a first attempt was made in order to measure the reaction rate of the molecule at different temperatures, which would have been an important step towards evidence of a tunneling reaction, since such a reaction has a rate that is nearly constant with temperature. It turned out however that once intermediate temperatures had been reached, the ratio of furan to phenol in XPS O 1s measurements after further annealing did not or only marginally increase. In order to find a reason for this, a force field simulation was launched that simulated the flip of OH around the C-O axis in a molecule in the Z-phase (Fig. 4.13), which was required for the tunneling reaction (or rather, its initial state). It turns out that such a flip requires a relatively high amount of energy (0.4 eV) and makes the tunneling reaction very unlikely. Therefore, once the Z-domain has formed, this process dubbed "conformational protection" quenches further conversion of the reactant.

4.7 Results for the Non-Deuterated Species

The hypothesis, namely that an intramolecular hydroalkoxylation has occurred in F1-DETP on Ag(111), has been supported by the results of different experimental techniques. STM topographs show that different domains on the surface can be identified for intermediate temperatures and that at least one such domain cannot be fitted with the intact molecule but with its product. Only this S-phase is then visible for high annealing temperatures. STM data is consistent with force-field simulation data; only marginal deviations are observed. TPD confirms that a deprotonation or fragmented desorption is highly unlikely in the relevant temperature range. XPS reveals that, when compared to literature values, the assumption of a hydroalkoxylation scenario is highly likely and plausible. Ratios expected from XPS investigations, which show a coexistence of product and reactant at intermediate temperatures and the absence of the

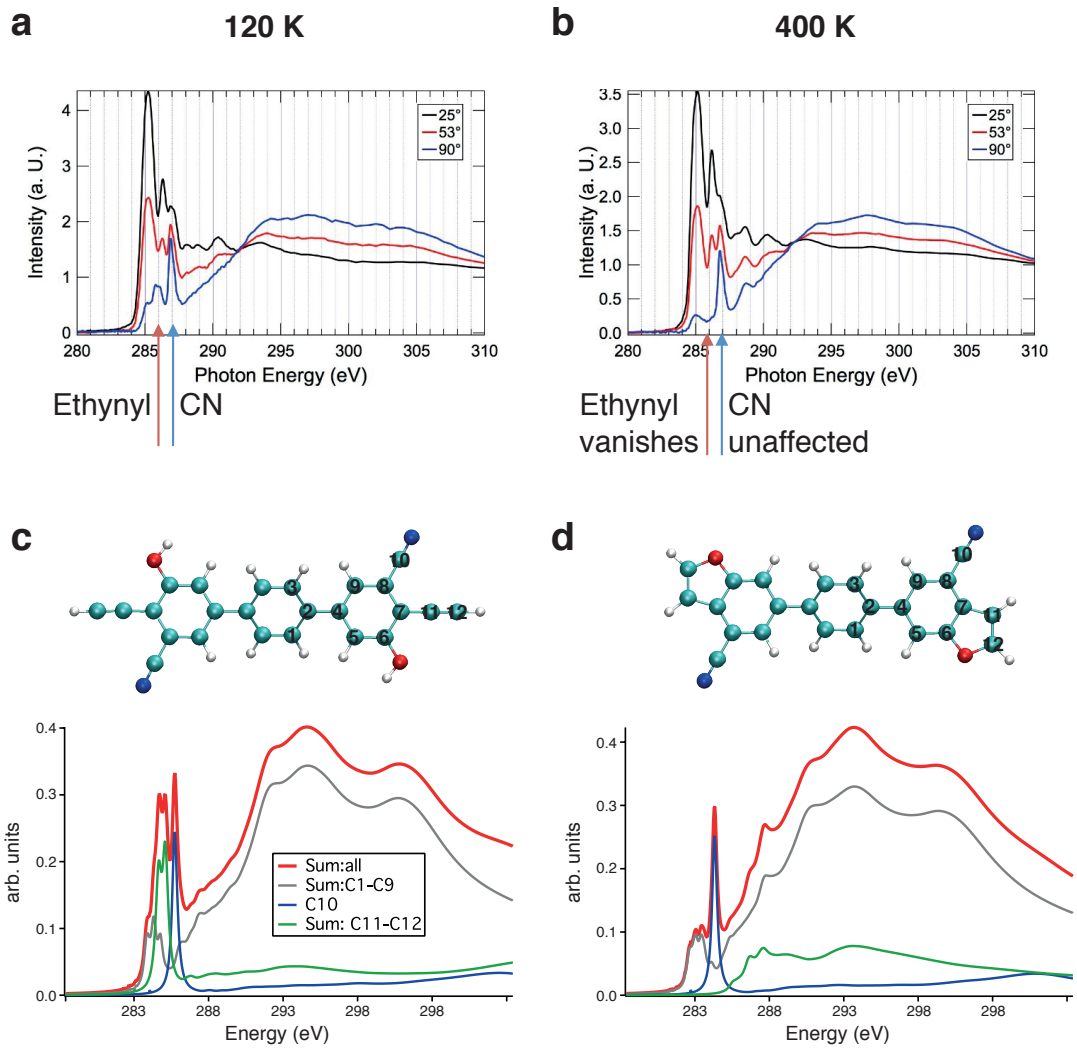

Figure 4.12: F1-DETP NEXAFS Theoretical Comparison with experimental C K-edge data for a variety of incidence angles and two different annealing temperatures (a, b) and simulated spectra for reactant (c) and product (d). Adapted from [108].

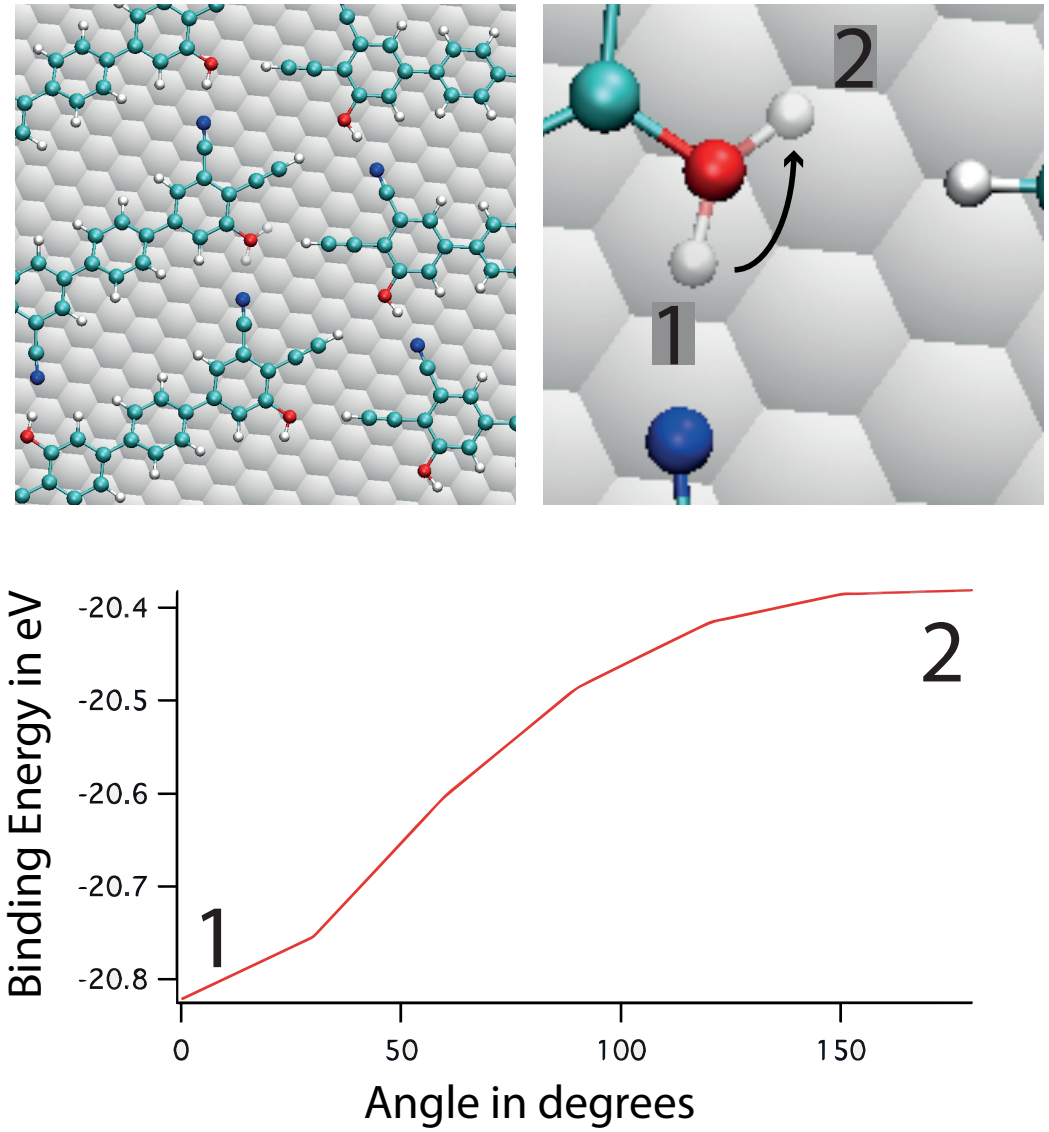

Figure 4.13: Conformational Protection in F1-DETP. Once the zig-zag motif has formed, moving the hydrogen atom around the C-O bond axis (from position 1 to 2) requires enough energy to quench any further reaction. Adapted from [108].

reactant for high annealing temperatures correspond to the coexistence of S- and Z-domains in intermediate temperature STM topographs and the absence of the Z-domains for higher annealing temperatures. NEXAFS confirms that the molecules are lying flat on the surface, which corroborates the steric hindrance scenario from S-phase STM data and that a chemical change only occurs in the CC triple bond but not in the CN moiety. Rates are hard to determine due to the conformational protection effect.

These findings however have so far mainly been focused on the reaction itself. Until now, it is not perfectly clear how this reaction proceeds and whether it does involve proton tunneling. In order to answer this question, the method of choice is the test with a deuterated variant of the molecule. While it is perfectly normal to observe a kinetic isotope effect (KIE) in a reaction, meaning that heavier ions involved in a reaction will generally slow it down, very large KIEs are interpreted as evidence for tunneling. In the following chapter, a comparison with a newly synthesized molecule, D-F1-DETP, which has OD instead of OH-groups, will be used in order to find such a KIE. Together with a theoretical investigation, the reaction mechanism will then be fully unraveled.

5 D-F1-DETP on Ag(111)

5.1 Molecule

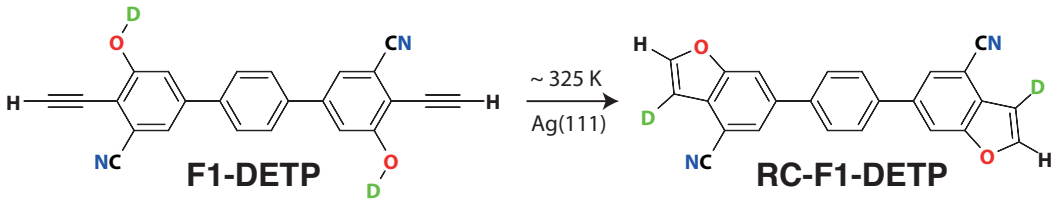

Figure 5.1: Scheme of the D-F1-DETP molecule. The hydrogens of the hydroxyls (and only they) were exchanged with deuterium atoms. Adapted from [108].

The deuterated molecule is shown above. Only the hydrogens of the hydroxyl groups were switched for deuterium atoms in order to evaluate their role in a possible tunneling step. The D-F1-DETP used in the XPS experiments was simply cooked in D_2O, while for the STM experiments it was specifically prepared from a precursor of F1-DETP. A complete description can be found in [108].

The molecule had to be handled with utmost care, as it turned out that air moisture was already able to convert OD into OH at room temperature. It was therefore stored in an Ar atmosphere until immediately before filling the OMBE crucible.

The reaction, as depicted in Fig. 5.1, eventually proceeded as the one shown for F1-DETP at high temperature. At intermediate temperature, as will be presented in the following, dramatic changes in the behavior of the molecule were observed.

5.2 STM Investigation

In Fig. 5.2 a direct and representative comparison of two STM topographs at intermediate annealing temperature (225 K) for F1-DETP and D-F1-DETP is shown. From the images, it is clear that a significant fraction of the non-deuterated molecules have already reacted and now form an S-phase (denoted with an S in the image). This is, however, not the case for the deuterated species in the right panel, where only the Z-phase is visible.

While two images do not immediately and conclusively prove that this accurately represents the situation on the surface, a statistical analysis can do so. Therefore, in Fig. 5.3, a set of large-scale STM images of D-F1-DETP annealed to 225 K on Ag(111) is depicted, which is in turn taken from many more such scans, showing no signs of S-domains, which means no product is observed. Since no S-phase was identified in any of the D-F1-DETP samples after annealing

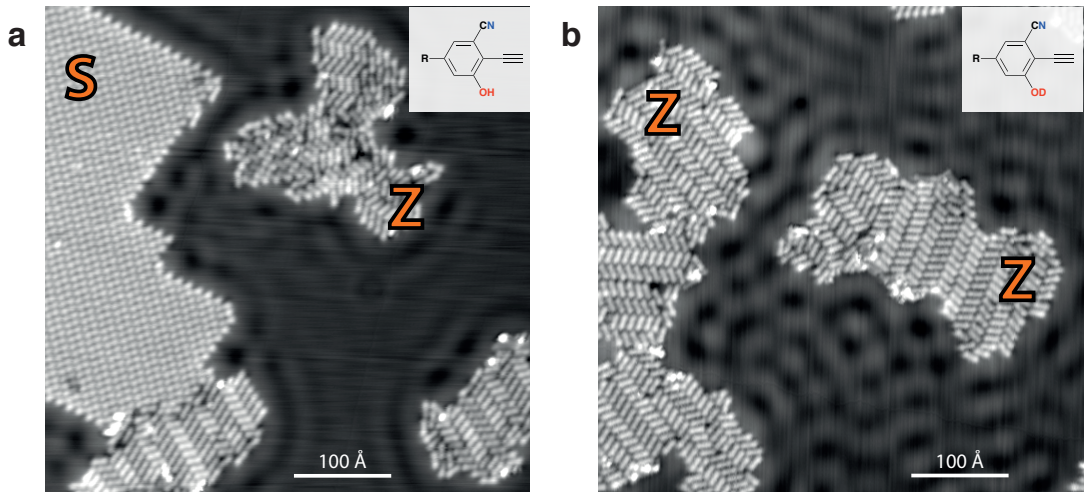

Figure 5.2: F1-DETP (a) to D-F1-DETP (b) STM topograph comparison showing only the Z-phase for D-F1-DETP annealed to 225 K. Setpoints: a $V_B = 50$ mV, b $V_B = 10$ mV, both $I_T = 100$ pA. Adapted from [108].

to 225 K and only few molecules could not be identified, a conservative estimate of 5 % reacted molecules is assumed. Even this already leads to a large KIE when compared to STM data from F1-DETP of about 10, indicative of tunneling (rate estimations, as far as they were possible, will be presented in the respective section below).

Fig. 5.4 shows an evolution of D-F1-DETP with annealing temperatures. Each sample was annealed 25 K higher than the one before, starting from 225 K at a and reaching 350 K at f. As seen above, the 225 K image does not show any signs of the S-domains. At 250 K, while minor irregularities can be observed, the sample is still dominated by the Z-phase. For higher temperatures, especially from 275 K to 300 K (c, d) the Z-phase is still dominant but an S-phase like intermediate phase with an irregular apparent height distribution appears (lower left and upper right in c and d respectively), which is assumed to consist of partially ring closed molecules. For higher annealing temperatures, mainly (325 K) or only (350 K) the S-phase is observed, which is evidence that the purely thermally triggered reaction in D-F1-DETP is the same as in F1-DETP and occurs under similar conditions.

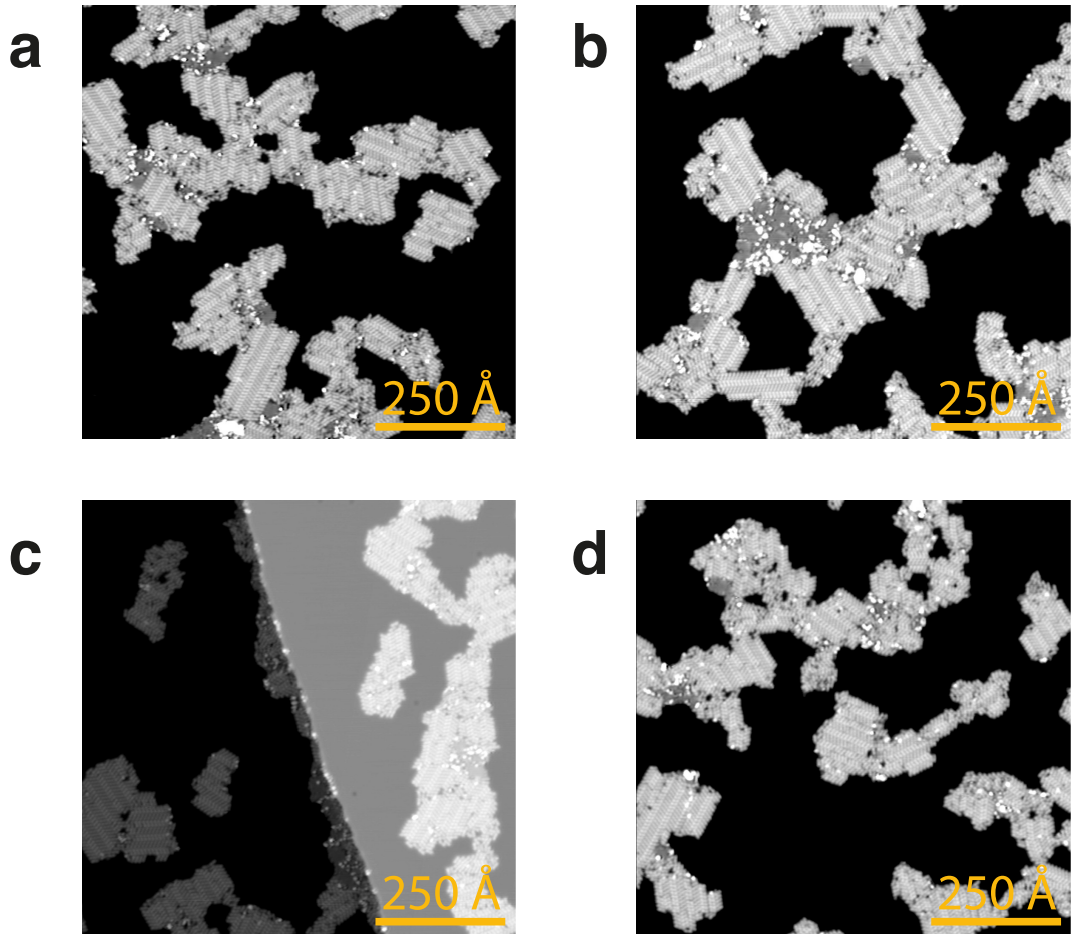

Figure 5.3: Four large scale images with submonolayer coverage of D-F1-DETP annealed to 225 K on Ag(111) taken from a larger sample. No product species is identified, only some molecules cannot be assigned to any phase. Setpoint: $V_B = 0.5$ V, $I_T = 100$ pA. Adapted from [108].

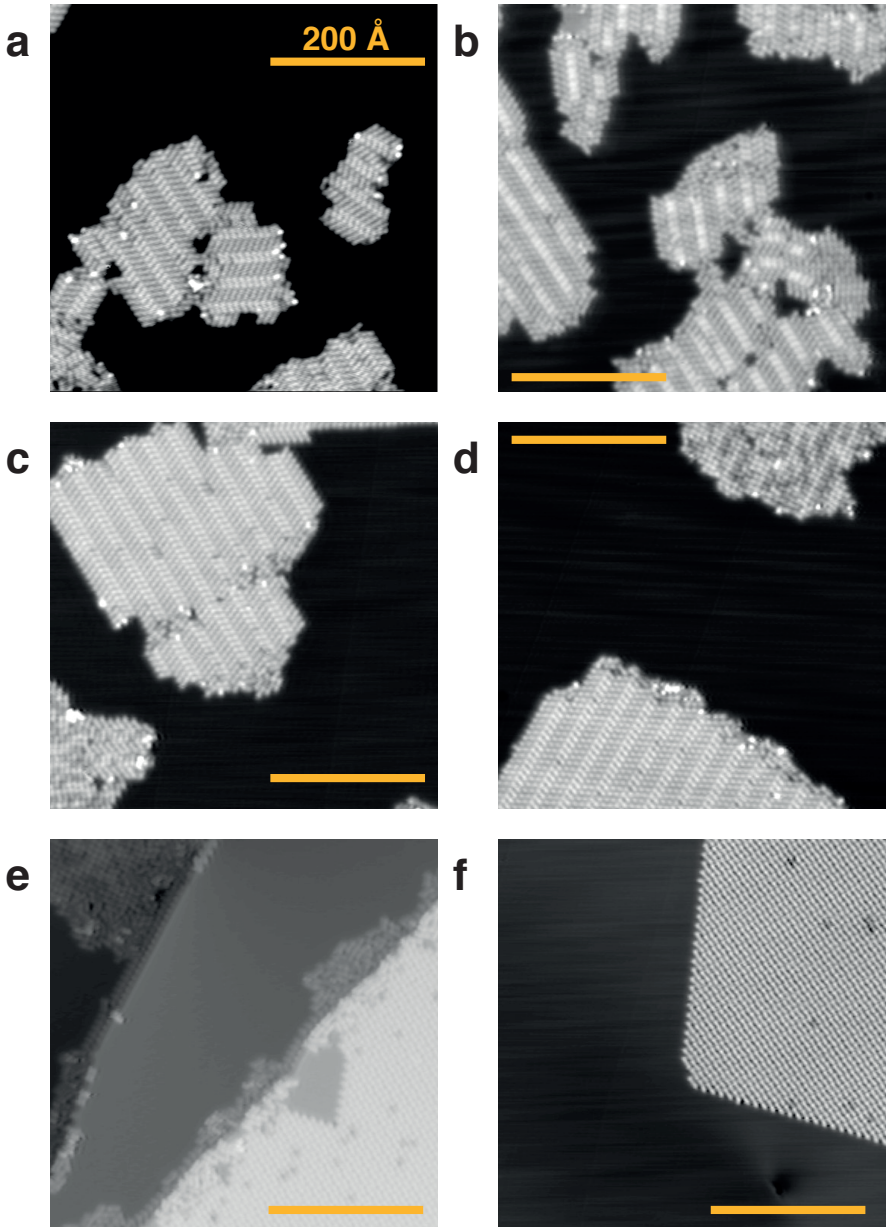

Figure 5.4: Six samples of D-F1-DETP on Ag(111) annealed to temperatures from 225 K to 350 K (a to f) in 25 K steps. Note the Z-phase in a and b with only minor impurities, still dominating in c and d as well. An intermediate S-like phase with irregular apparent height distribution appears in c and d, in e (325 K) the S-phase dominates, in f only the S-phase is observed (350 K). Setpoints: a $V_B = 0.5$ V, $I_T = 100$ pA; b $V_B = 1.0$ V, $I_T = 100$ pA; c-f $V_B = -0.5$ V, $I_T = 100$ pA. Adapted from [108].

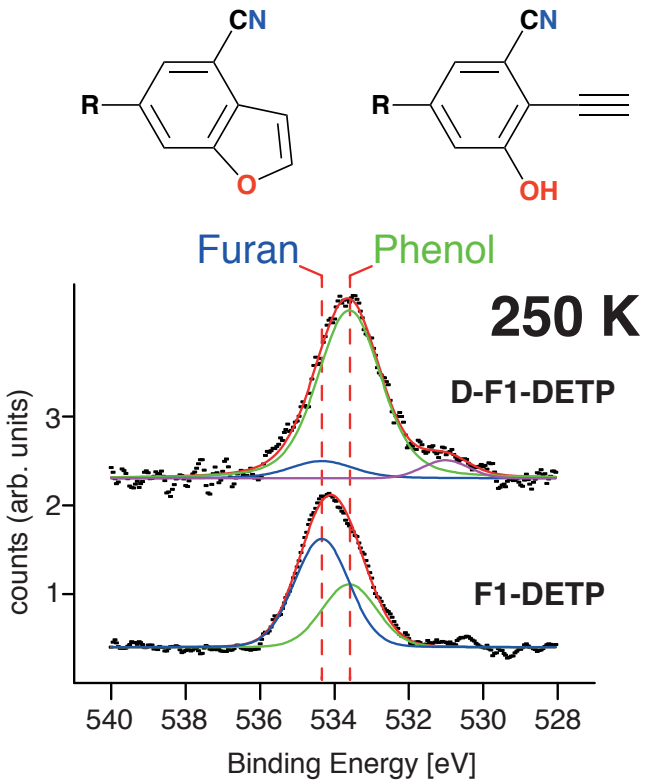

Figure 5.5: A comparison of O 1s signals for F1-DETP and D-F1DETP with dashed vertical lines indicating the peak positions for furanic and phenolic species after annealing to 250 K. Adapted from [108].

5.3 XPS Investigation

When comparing the O 1s signals of F1-DETP and D-F1-DETP (Fig. 5.5) under the peak assignment explained in the F1-DETP XPS section for furanic and phenolic species, it can be deduced that F1-DETP (lower graph) and D-F1-DETP (upper graph) greatly differ in their behavior when annealed to 250 K. While for the non-deuterated variant, the product is favored after annealing, for the deuterated variant it can barely be detected. That there is still some furanic species in the deuterated variant might also be influenced by the simpler preparation method[1] when compared to the D-F1-DETP used in the STM experiments.

[1]For the XPS experiments, only D-F1-DETP obtained from F1-DETP cooked in D_2O was available.

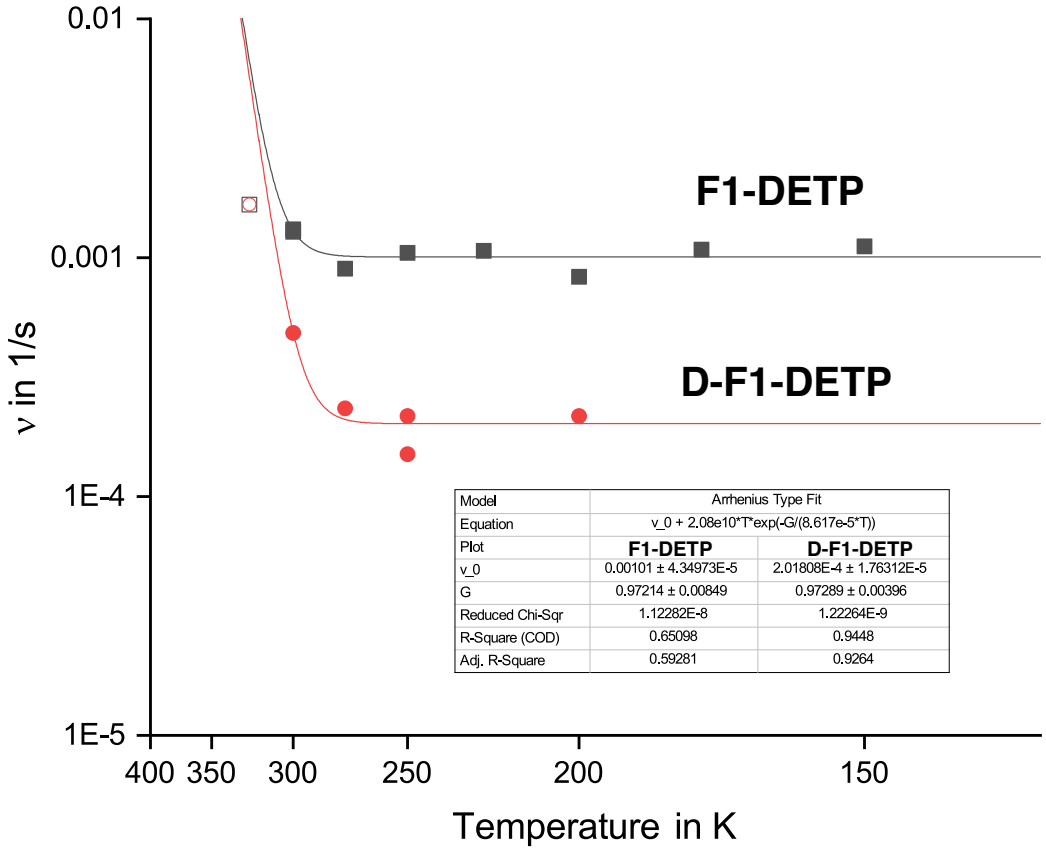

Figure 5.6: D-F1-DETP and F1-DETP rate comparison. Fit does not include hollow points. Adapted from [108].

5.4 Comparison of Reaction Rates

While some problems occurred when trying to calculate reaction rates for F1-DETP, a tentative estimate and comparison for both, the deuterated and the non-deuterated variant, is nonetheless provided in Fig. 5.6. The data points in the sample are obtained from several different sources and combine XPS and STM (statistical visual identification) experiments. It is calculated assuming a constant rate during the 10 min annealings. Data points above 300 K were not included (hollow symbols), as at that point all molecules of both variants are assumed to have reacted. Furthermore, it should be kept in mind that all data points only give lower bounds due to the conformational protection mechanism mentioned above. The graphs show the typical behavior of a tunneling reaction, as a base rate independent of the temperature below 300 K transitions to an Arrhenius graph above that temperature with a significant offset between the deuterated and the non-deuterated variant, yielding a significant KIE.

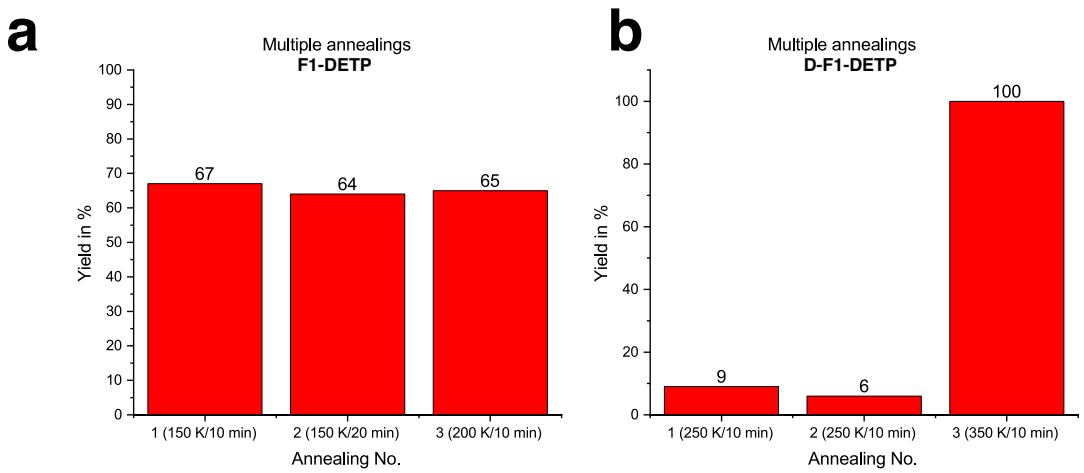

Figure 5.7: D-F1-DETP and F1-DETP multiple annealings. Adapted from [108].

Fig. 5.7 illustrates two different characteristics of the molecule. In a, a multiple annealing series of the original, non-deuterated F1-DETP is depicted in order to show why determining rates was so difficult. After the first annealing, two thirds of the molecules had already reacted, yet further annealings did not significantly alter the adsorbate concentrations. In b, the behavior of the deuterated variant D-F1-DETP is shown. While generally a very low fraction of the product is detected (possibly due to the molecule preparation method used in the XPS measurements on which this graph is based), the reaction proceeds normally at the thermal threshold.

5.5 Reaction Mechanism and DFT Support

The reaction pathway for the intramolecular hydroalkoxylation pathway was simulated via DFT (harmonic transition state theory) methods by Jonas Björk. Details are given in [108], however it ought to be mentioned that identifying the tunneling turning points was achieved by a novel algorithm that is to be published elsewhere.

At first glance, the right panel already shows that, while the reaction rate itself does not match the experimental rates, the difference between tunneling and classical rates corresponds to the large KIE requirement for experimental data with regard to tunneling. The rates are influenced by the number of channels available. Since in theoretical calculations only one channel or very few alternative channels are investigated, orders of magnitude between experimental and theoretical values are not uncommon in tunneling reactions [124].

Fig. 5.8 shows both, the classical and the tunneling pathway. In this framework, the hydrogen of the hydroxyl group is first transferred to the alkyne group (from initial state IS via transition state TS1 to intermediate state IntS), whereafter a ring closing reaction (transition state TS2 to final state FS) is initiated after the C_2H_2 moiety has turned (from the intermediate state to the second transition state TS2). The surface facilitates the reaction, especially since the intermediate state is lowered in energy due to the outermost carbon atom binding to the Ag

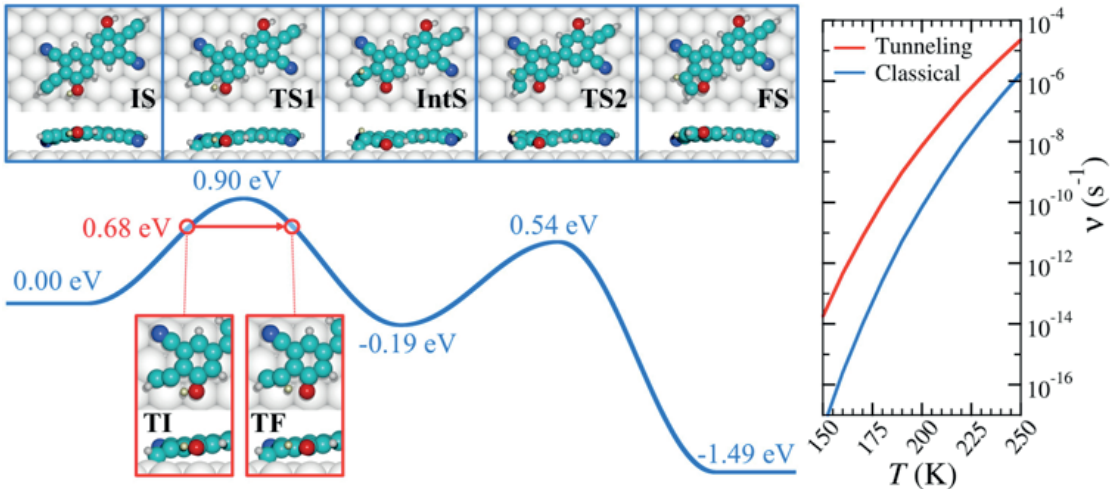

Figure 5.8: DFT calculated reaction pathway of an F1-DETP like, simplified molecule. The classical minimum energy pathway at $T = 200$ K is shown in blue, the tunneling step in red. Above the pathway top and side views of minima and transition states are depicted. Below the pathway, the tunneling turning points are shown in red frames. The right panel gives a rate comparison. Adapted from [108]. Figure created by Jonas Björk.

surface (cf. panel 3). The classical reaction rate for a barrier of 0.903 eV at 200 K as given by the Eyring equation yields

$$\nu_C = \frac{k_B T}{h} \cdot \exp\left(\frac{-\Delta G}{k_B T}\right) = 7.0 \cdot 10^{-11} \frac{1}{s} \tag{5.1}$$

rendering the reaction classically impossible. The tunneling turning points identified with the method mentioned above, however, are two turning points of the same energy that allow an H transfer over a distance of just 0.60 Å. Employing the WKB approximation and assuming a barrier from the free energy of state TI to that of the maximum energy in the tunneling channel, the tunneling rate shown in the right panel was calculated. As pointed out above, the general features of a tunneling reaction are represented by this comparison, even though the experimental rates are far higher, which can be explained by additional tunneling channels or more favorable, yet unfound, turning points. Finally, the DFT approach gives an impression of the reaction mechanism that allows for a better interpretation of the experimental findings. Especially a possible tunneling mechanism is confirmed, and while absolute values for the rates are somewhat off, the general fact of a large classical v. tunneling ratio of reaction rates is confirmed.

5.6 Discussion of the Intramolecular Hydroalkoxylation Reaction

With the additional insights gained from the D-F1-DETP experiments and a thorough theoretical analysis of the reaction pathway, not only general information about the reaction that was established in the last chapter is obtained. It turns out that D-F1-DETP generally reacts later, as observed from STM and XPS data. In the STM data, pure Z-domain samples were possible with only some unidentifiable molecules leading to conservative estimates regarding yield estimates. XPS data generally returned the same results, though due to the preparation method used for the molecules, a relatively high ratio of reacted molecules was found. Nonetheless, the KIEs obtained point to tunneling as a rate determining step in the reaction at hand. A tentative comparison of the reaction rates returned graphs with the standard combination of Arrhenius-like and constant rate that is generally found for tunneling reactions, including the rate offset between the deuterated and non-deuterated molecule. Multiple annealing experiment for both variants exemplify the problem (or depending on the situation, maybe even feature) of conformational protection in the Z-phase, while standard behavior of the deuterated variant above the thermal threshold was demonstrated. Thanks to the theoretical description of the system, even though the calculated rates are influenced by unavoidable systematic errors, it was possible to show that the classical process is nearly impossible in the relevant temperature range but also that tunneling can greatly enhance the reaction rate. In conclusion, it was established via a combination of the methods above that the reaction in question is indeed a tunneling mediated hydroalkoxylation reaction.

As pointed out above, one of the advantages of this reaction is that, while it does proceed via tunneling, there are several ingredients needed. The reaction is influenced by the prealignment of the molecules and by a thermal activation. As a proof of concept, this could lead to new techniques in the construction of nanostructures by integrating tunneling steps into the self-assembly protocol.

6 Honeycomb Networks via Ext-TEB on Ag(111)

6.1 The Molecule and its Previous Applications

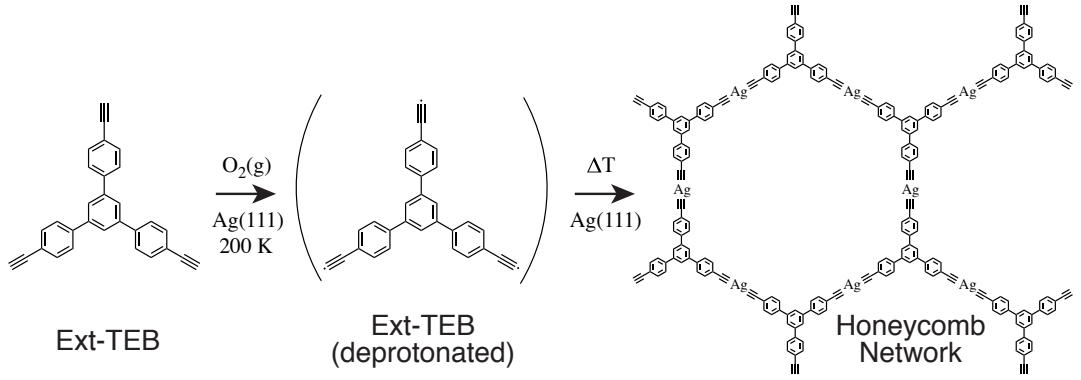

Figure 6.1: Scheme showing Ext-TEB and the reaction proceeding on the Ag(111) surface. Though it was possible to stabilize the radical on the surface, it is shown in brackets as an intermediate state.

This chapter is concerned with the formation of an extended (micrometer-scale), highly-regular organometallic honeycomb network. The formation of this network proceeds through a gas-mediated deprotonation step after which the radicals attach to adatoms provided by the Ag(111) surface, cf. Fig. 6.1. It is interesting in so far as traditional routes for bottom-up construction protocols often focus on co-adsorbed molecules and thermal activation only, while the mechanism presented here is analogous to Eley-Rideal mechanisms [125], with adsorbed precursors and additional reactants from the gas-phase. Though an exact examination of the reaction pathway turned out to be very difficult, since even with further XPS and TPD data it was not possible to clearly identify desorbed products, the novelty here is that the reaction offers an extraordinarily clean pathway towards large-scale organometallic networks when carried out strictly according to protocol.

To provide some context, an outline of previous studies with this and similar other molecules (TEB) is given. TEB and Ext-TEB have previously been used as promising candidates for the bottom-up synthesis of graphdiyne-related structures [126–128] via coupling of terminal alkynes [27, 28, 129]. Further experiments have turned out to be quite fruitful, with results ranging from reticulated networks on Ag(111) [130], an intriguing assembly of the molecules adsorbed on Ag(111) [131], deprotonation and deprotonation driven assembly on Cu(111) [132]

to Ho-mediated homo-coupling [133]. The homo-coupling observed in Ext-TEB [130] thereby represents an alternative to the well-known method of Ullmann-coupling [28], which also avoids co-adsorbed halogens [134]. Such co-adsorbed halogens can influence the self-assembly process [135] and are recognized as a factor hampering further polymerization as they can cause "steric crowding" [136, 137].

One of the biggest promises in the field is the precise construction of covalent material, which includes the formation of long-range C-C bonded structures [41, 138–140], as these strong bonds make applications more realistic by allowing high stability, the promise of tunable bandgaps (especially with regard to graphyne and graphdiyne) and possibly a removal of the layer from the substrate. Often, C-Metal-C bonded sheets are considered an intermediate on the path to C-C bond formation [141]. However, it turns out that, especially in this case, organo-metallic networks can display extraordinary (thermal) stability. Here, the organometallic network could not be converted to C-C bonds, however, C-M-C bonds also show covalent character [140] and are therefore promising candidates for organic insulators [42, 142]. The material created here thus offers an exciting new possibility for a 2D material with novel applications, especially since long-range ordered materials with these features seem to be hard to achieve (see citations at the beginning of the paragraph).

In the following, the molecular behavior will be established under several conditions. In the first part, the focus is on showing that the molecule will not simply develop the honeycomb network after long-term annealing, excluding a preparation method without the addition of oxygen[1]. The second part will portray the ideal recipe and optimal annealing temperature for long-range, well ordered honeycomb networks. A third part is dedicated to a detailed analysis of the synthesized networks, while a fourth part evidences that the steps of the synthesis protocol (Ext-TEB adsorption and subsequent oxygen treatment and annealing) cannot simply be carried out in any manner. It is shown that adsorbing oxygen at very low temperature after Ext-TEB has dramatic consequences on the outcome of the experiment. Afterwards, a final discussion is offered in order to concisely sum up the most important findings.

As to experimental conditions, the specifications laid out in the STM experimental section apply here. The molecules were deposited on the sample from a Knudsen cell heated to 200-210°C for about 20 minutes, varying due to desired coverage, substrate temperature and filling level.

6.2 Ext-TEB on Ag(111) without O_2 Treatment

Before proceeding towards an annealing of the molecules or the oxygen treatment experiments, the adsorbates are shown prior to these treatments and consistency with previous findings [131] is established. Fig. 6.2 shows the close-packed phase achieved after evaporation of the molecules on the substrate held at 200 K. Fig. 6.2 b is a zoom into a with the silver lattice and semi-empirically simulated molecular models simulated with Hyperchem [113]. The unit cell

[1] In preliminary experiments it seemed as if the networks would form by themselves at room temperature. Further research revealed, however, that the vacuum in the preparation chamber was one order of magnitude worse than for the experiments presented here, which lead to the conclusion that the remaining gas had converted the reactants in the preliminary experiments. This was an important conclusion, as it finally inspired the oxygen treatment experiments.

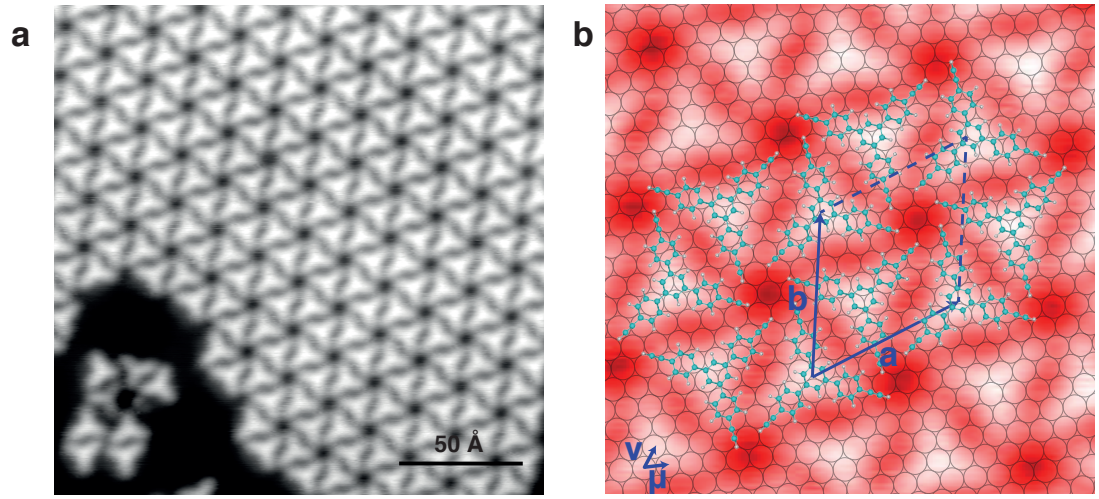

Figure 6.2: STM topograph showing the standard close-packed phase of Ext-TEB on Ag(111) (a) with a zoom-in overlayed with the Ag(111) lattice (b) (high symmetry directions confirmed by a separate atomic resolution image, a registry is proposed for the adsorbates). Setpoint: $V_B = 0.1$ V, $I_T = 100$ pA. Preparation temperature: 200 K.

vectors of the molecules can be expressed through the unit cell vectors of the substrate lattice as follows:

$$\begin{pmatrix} \mathbf{a} \\ \mathbf{b} \end{pmatrix} = \begin{pmatrix} 5 & 3 \\ -3 & 8 \end{pmatrix} \begin{pmatrix} \boldsymbol{\mu} \\ \boldsymbol{\nu} \end{pmatrix} \tag{6.1}$$

which simply represents a version chirally different from the unit cell identified in [143], in line with [131]:

$$\begin{pmatrix} \mathbf{a_c} \\ \mathbf{b_c} \end{pmatrix} = \begin{pmatrix} 8 & -3 \\ -5 & 8 \end{pmatrix} \begin{pmatrix} \boldsymbol{\mu} \\ \boldsymbol{\nu} \end{pmatrix} \tag{6.2}$$

The proposed registry is commensurate, in line with the lack of a Moire pattern. Given the atomic distance on Ag(111) of $\mu = \nu = 2.889$ Å all unit cell vectors have the length $a = b = a_c = b_c = 20.22$ Å.

The governing intermolecular interactions for this phase have been thoroughly studied in [131], with extensive DFT support for the molecule's smaller analog TEB. From the evaluation of a charge difference plot in the cited work, it is concluded that two main interactions determine the assembly. First, a weak H-bond between neighboring ethyne groups is identified, indicated by an electron depletion around one moiety's hydrogen and an electron accumulation around the other moiety's π-system. The same can be observed between ethyne π-systems and neighboring aromatic rings, where an electron depletion of the ring is observed, with the lone pair of the ethyne group pointing towards it. This is consistent with a proton-acceptor-ring interaction (PARI) [116]. Both bonds are found to contribute significantly to the bonding motif due to comparisons with molecules lacking ethyne-ethyne interactions. The average bond

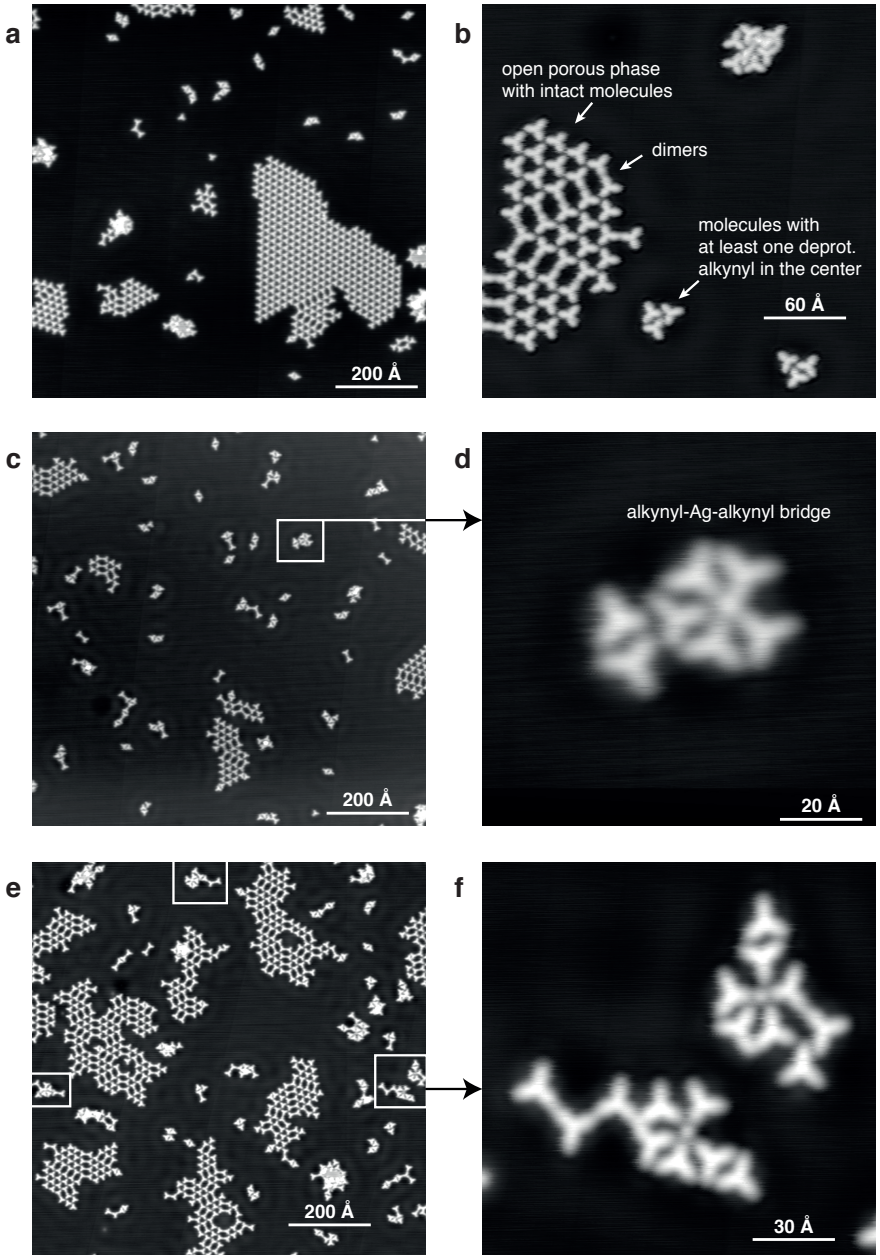

Figure 6.3: Annealing series showing the behavior of Ext-TEB on Ag(111) annealed at 300 K for 16 h (a, b), 29 h (c, d) and 63 h (e, f). Images d and f are zoom-ins into c and e respectively (areas are marked with white rectangles, further white rectangles in f denote further alkynyl-Ag-alkynyl bridges. At first, only covalent dimers and some deprotonated molecules are discovered. Further annealing results in an increasing number of alkynyl-Ag-alkynyl bridges, however, no honeycomb networks were observed without oxygen treatment. For intact molecules, an open porous phase is preferred. Setpoints: a $V_B = 1.0$ V, $I_T = 100$ pA; b-f $V_B = -0.1$ V, $I_T = 200$ pA.

distance is about 3 Å (ethyne) and 3.17 Å (PARI).

First, we tested the chemical conversion triggered by conventional annealing at 300 K. Samples of Ext-TEB on Ag(111) ordered by annealing time are depicted in Fig. 6.3, which shows the evolution of the species on the surface at room temperature. For a time frame of 63 h, the development on the substrate is outlined in three steps (16 h, 29 h and 63 h). This particular investigation was inspired by previously gathered data which implied that sufficiently long annealing times at room temperature would trigger the formation of an organo-metallic network. As observed from the STM topographs, repeating this technique only had very limited success. The open-porous phase of the molecule and some covalently linked dimers [130] along with few deprotonations can be readily observed after 16 h. The deprotonations are identified by characteristic molecular assemblies (highlighted in Fig. 6.3) via additional XPS and DFT data comparison, which show that the highlighted trimolecular structure includes two molecules oriented at a deprotonated terminal alkyne (see Fig. 6.4 a and b for occurrence after oxygen treatment and a model). No alkynyl-Ag bonds are found after 16 h. After 29 h and 63 h, the amount of dimers increases, as expected, and some Ag-alkynyl bonds are observed, where a center adatom can be resolved. These occurrences are highlighted in Fig. 6.3 c and e. While their number really does grow larger, no honeycomb network formation could be expected from this approach, since dimerization clearly occurs faster than Ag-alkynyl bonding. Even if this method had shown results, preparation times of several days would have rendered it inadequate.

It was thus concluded that indeed the residual gas contained in the preparation chamber must have had a decisive effect on the reaction observed in previous data in which the organometallic phase was discovered (see footnote above). Yet as already noted, this annealing experiment served two important purposes: on the one hand it excluded the possibility that only annealing can lead to the honeycomb networks and on the other hand it inspired the oxygen approach after we had figured out that residual gas in conjunction with moderate annealing temperatures was present when the honeycomb phase was first recorded.

6.3 Ext-TEB on Ag(111) with O_2 Treatment

Following the unsuccessful attempts to generate the honeycomb networks solely through annealing, the oxygen approach was implemented. Low doses of oxygen first lead to the already familiar trimolecular cluster shown in Fig. 6.4 a, which can be rationalized with the DFT model presented in b. Slightly higher doses of oxygen (Fig. 6.4 c) already give the assembly an entirely different appearance. This intensifies upon exposure of a sample like the one presented above 6000 L of oxygen (cf. Fig. 6.5 a). The phase is now denser and depressions are visible at the molecule's ends (marked with arrows in Fig. 6.5 b). The depressions are attributed to deprotonation occurring due to the oxygen treatment by way of analogy to previous experiments with the same molecule on Cu(111) [132]. Both, the emerging molecular assembly and extensive previous and current XPS measurements (Fig. 6.4 d, low binding energy contribution is evidence of strong substrate interaction which in turn indicates deprotonation [132]) and DFT calculations are consistent with the ionic hydrogen bond scenario found on Cu(111) previously. For example, through measurements by Yiqi Zhang and Felix Haag, it was found

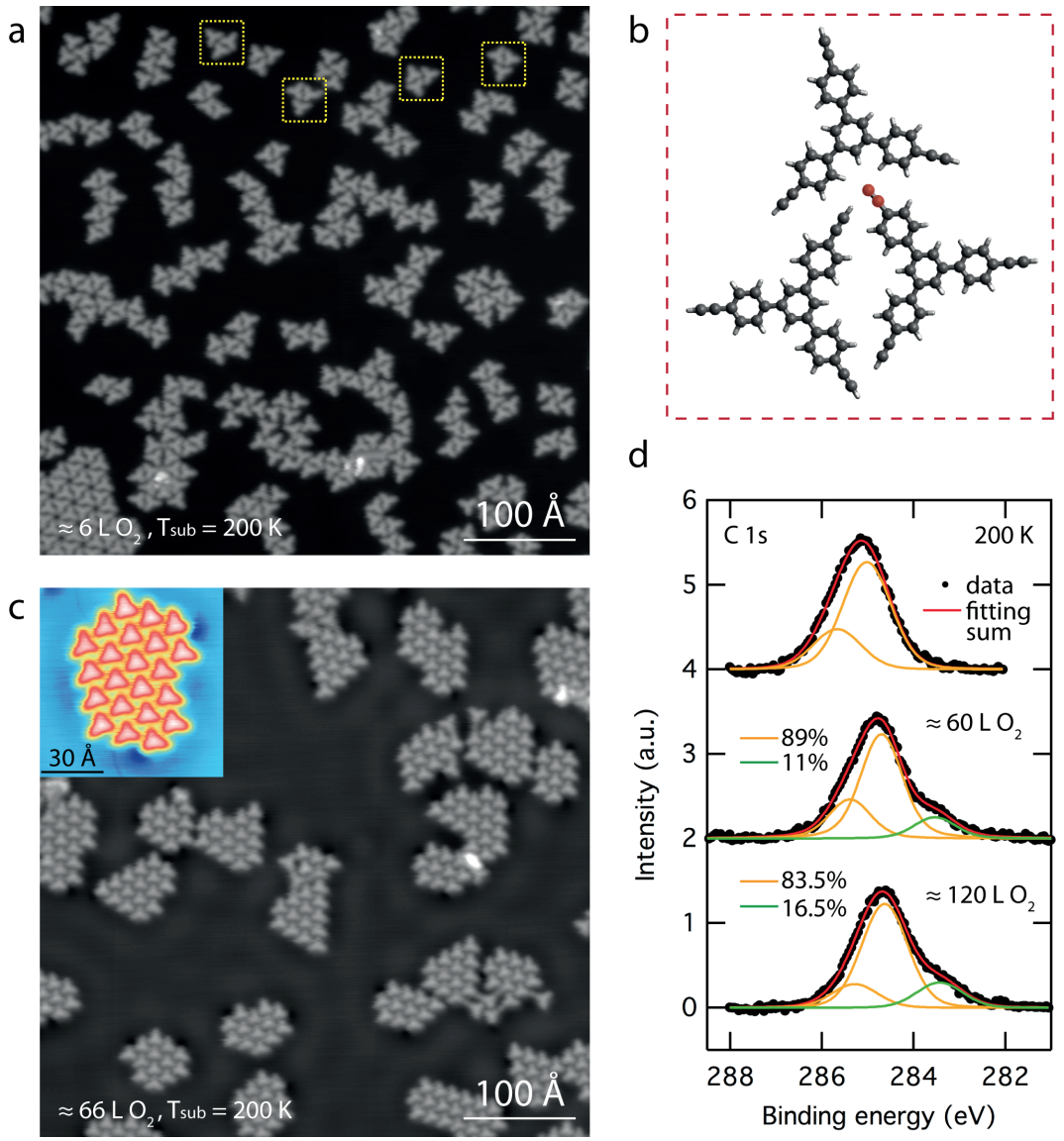

Figure 6.4: STM topographs showing Ext-TEB on Ag(111) after a 6 L (a) and 66 L (c) oxygen treatment at a substrate temperature of 200 K complemented by a gas phase DFT (RPBE-D3BJ/def2-SVP) model (b) of a trimolecular Ext-TEB cluster in which one alkyne is deprotonated (red) and C 1s XPS spectra (d) of sub-monolayer Ext-TEB@Ag(111) before and after oxygen treatment. The yellow dashed squares in (a) highlight the clusters shown in (b) already known from the experiments without O_2 above. Higher dosage of oxygen (c) results in the phase thoroughly investigated in Fig. 6.5. XPS data (d) reveals that for oxygen dosages of 60 L and 120 L the deprotonation rate can be estimated to be 60 % and 80 % respectively (max. value of the low binding energy contribution is 20 %, green line). Setpoints: a $V_B = -1$ V, $I_T = 100$ pA; c $V_B = -0.1$ V, $I_T = 100$ pA. Reprinted/adapted with permission from [143]. Copyright 2019 American Chemical Society. Image composition by Yiqi Zhang.

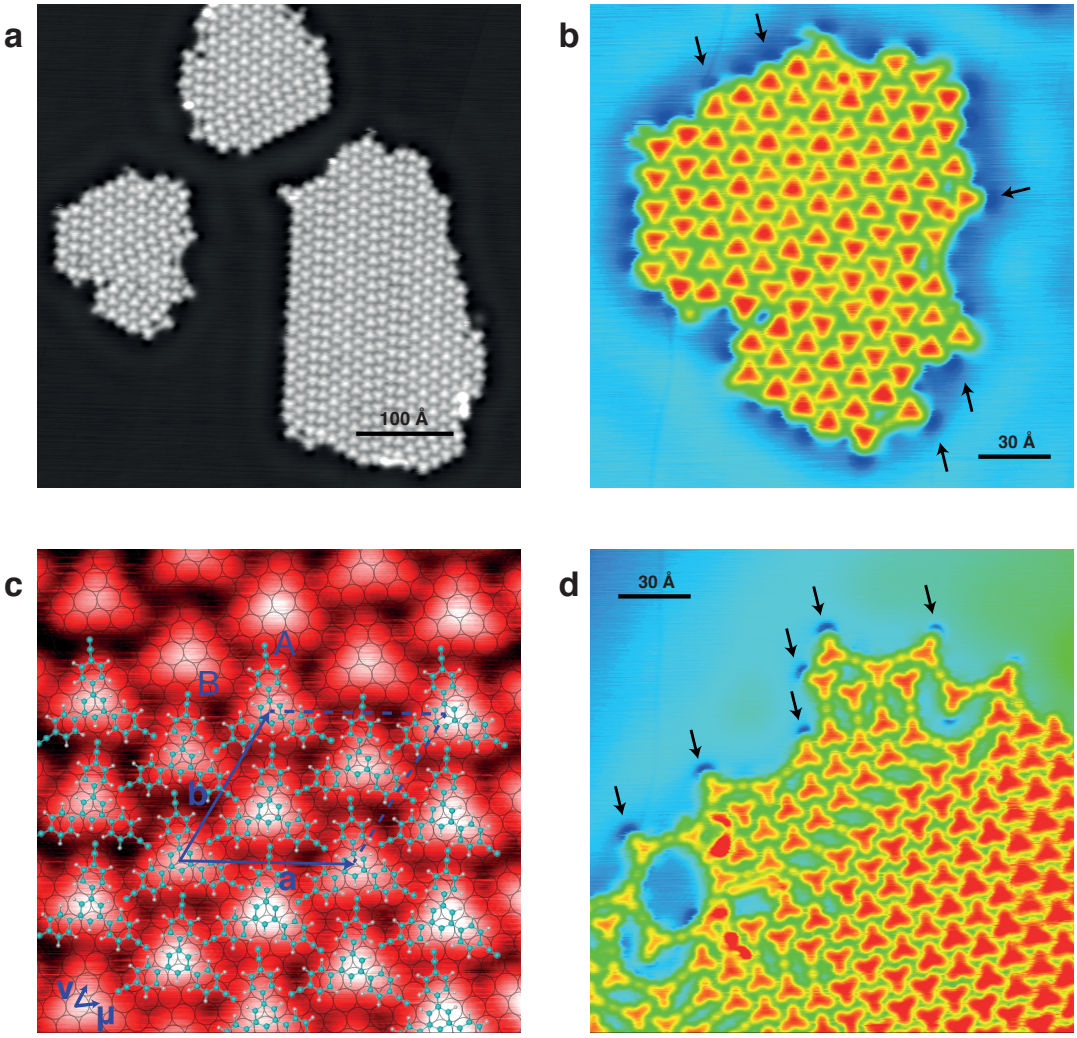

Figure 6.5: STM topograph showing Ext-TEB on Ag(111) after an oxygen treatment without further annealing achieved from the sample in Fig. 6.2 (200 K). (a) Overview image showing close-packed molecular islands, (b) zoom-in with arrows pointing at characteristic depressions indicating dehydrogenated molecular species, (c) zoom into an island of deprotonated molecules with a proposed registry, the unit cell is bimolecular with molecules showing two different adsorption geometries A and B, where in A, alkyne radical groups lie on top sites and in B, they lie on bridge sites, (d) after annealing to 250 K, honeycomb network formation from these islands is observed. Setpoints: a $V_B = -0.5$ V, $I_T = 100$ pA; b $V_B = -0.2$ V, $I_T = 100$ pA; c $V_B = -0.2$ V, $I_T = 100$ pA; d $V_B = -0.1$ V, $I_T = 100$ pA.

that after the oxygen treatment, the C 1s binding energy of Ext-TEB shifts down by 0.3 eV, which is in line with other reactions involving on-surface dehalogenation [25] and CH activation [144], most likely due to the negative partial charge of the molecule after bonding to the metal surface. Furthermore, another feature in the XPS data [143], a C 1s shoulder at a binding energy of 283.6 eV is identified as indicative of alkynyl-metal bond formation [145, 146] with a contribution close to its simulated area. Likewise, since no O 1s is detected for such a sample after the treatment, remaining byproducts or adsorbed oxygen can be excluded.

Fig. 6.5 c shows an STM zoom-in overlayed with the Ag(111) lattice and simulated, deprotonated molecules. The elementary unit cell is given as

$$\begin{pmatrix} \mathbf{a} \\ \mathbf{b} \end{pmatrix} = \begin{pmatrix} 8 & -1 \\ 1 & 7 \end{pmatrix} \begin{pmatrix} \boldsymbol{\mu} \\ \boldsymbol{\nu} \end{pmatrix} \tag{6.3}$$

with $a = b = 21.8$ Å. The molecular fit uses a flat adsorption geometry, while the simulations for Ext-TEB on Cu(111) indicated a bent adsorption geometry, owing to the molecular model stemming from a semi-empirical gas phase simulation with HyperChem. The assembly is governed by a trifurcated CH-$\pi^{-\delta}$ hydrogen bond. Note that two different adsorption geometries are observed, A and B with the ethynyl groups occupying top sites in A and bridge sites in B, leading to a larger unit cell (Fig. 6.5 c).

After annealing the sample to 250 K, signs of a new bonding motif are visible (Fig. 6.5 d). While the characteristic assembly is still observed, at the edges of a molecular island the first alkynyl-Ag-alkynyl linkages are present. Depressions on the peripheral functional moieties are still identified as well as the clearly resolved silver adatoms in the Ag-alkynyl dimers, trimers and oligomers.

When these structures develop further Ag-alkynyl linkages, they do not immediately form a perfect honeycomb network. Instead, upon further annealing to intermediate temperatures (300 K), they form distinguishable patches of molecular assemblies on Ag(111) dubbed Phase I and Phase II (see Fig. 6.6). Phase I hereby is the fully formed Ag-alkynyl network (which is only disturbed by occasional impurities and which also contains trapped molecules), phase II consists of Ag-alkynyl macrocycles. Phase I is shown clearer in the upper right panel of Fig. 6.6. It consists of Ag-alkynyl linkages arranged as a honeycomb, the Ag-adatoms could be clearly resolved in the STM topograph. It is noteworthy that the unit cell is twice as large as expected due to different pore sizes, the pores exhibit a glide symmetry (explained in detail in the next section). When considering the thermal evolution of the Ag-alkynyl linkages present on the surface (see Fig. 6.7), it is observed that the phase II to phase I ratio continuously drops from infinity to 0 for higher annealing temperatures, justifying the assumption that phase II is an intermediate in the conversion from Ag-alkynyl linkages to phase I.

The annealing series for the honeycomb network formation given in Fig. 6.7 is meant to depict the effect of different annealing temperatures on network formation in order to produce networks with the maximum possible lateral dimensions (Fig. 6.8) with the highest possible purity and structural quality. While an annealing temperature of 300 K enables the coexistence of phase I and II (with a preference for phase II, as seen in Fig. 6.6), higher annealing temperatures quickly lead to a preference for phase I, as observed in Fig. 6.7 a, annealed to 350 K. While there are already long-range phase I networks appearing in Fig. 6.7 a, a patch of phase II is still left in

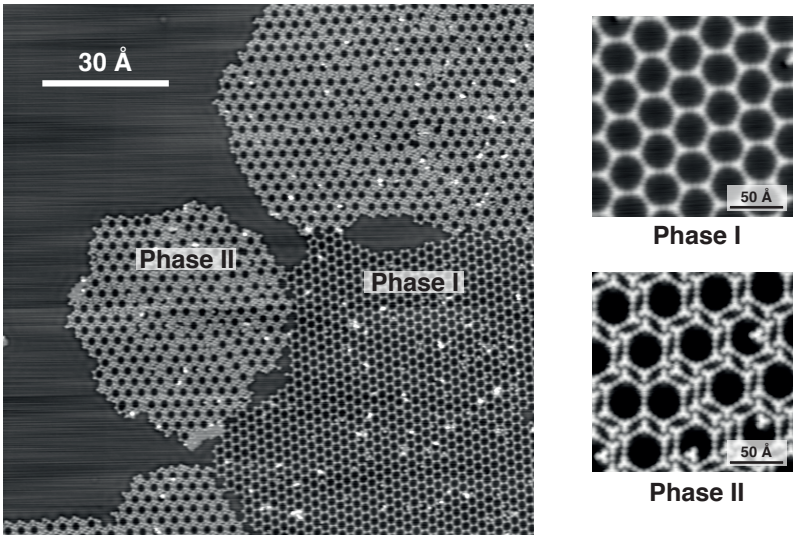

Figure 6.6: STM topograph showing the formation of Ag/Ext-TEB honeycomb networks on Ag(111). Phases I and II are denoted to differentiate between the alkynyl-Ag network (I) and organometallic macrocycles (II). Note the visibility of the adatoms in both phases (image quality for phase II is better). Setpoints: $V_B = -0.1$ V, $I_T = 200$ pA; zoom phase I $V_B = -0.1$ V, $I_T = 100$ pA; zoom phase II $V_B = -0.2$ V, $I_T = 100$ pA. Annealing temperature: 300 K.

the center. Upon annealing to 375 K, these phase II patches disappear and the phase I networks grow larger, as seen in Fig. 6.7 b. Annealing further to 425 K seems to result in increased network purity and lateral dimensions (Fig. 6.7 c, d), with the assembly covering the full step-edge and the zoom-in showing only few impurities and some trapped molecules. Yet annealing to higher temperatures does not improve the sample's condition anymore. Large scale image e indicates that scanning conditions have worsened even for ideal tip conditions, which indicates that the overall regularity and definition of the network have deteriorated. This can be directly observed in zoom-in f, which shows that the honeycomb structures are breaking up, leading to more molecules in pores or irregular structures replacing pores. Ideal annealing temperatures in order to achieve long-range network formation therefore are deduced to be 375-425 K.

Fig. 6.8 shows how large these networks can grow. The image covers ca. 1 µm horizontally, which evidences the extraordinary capabilities of this type of synthesis. Further confirmation of the mesoscopic extension and thermal stability up to room temperature of the network is provided through LEED measurements by Yiqi Zhang and Felix Haag [143], leading to an intriguing new method for the formation a 2D material. Further conversion to C-C covalent bonds was not possible, as higher annealing temperature (450 K and above) lead to an irreversible disintegration of the precursor network (see above) rather than enabling covalent coupling. One reason for this strong preference may be found in the organometallic phase's match with the substrate lattice, which has been shown to cause high selectivity when there is a rivalry between Glaser-coupling and Ag-alkynyl bond formation [147].

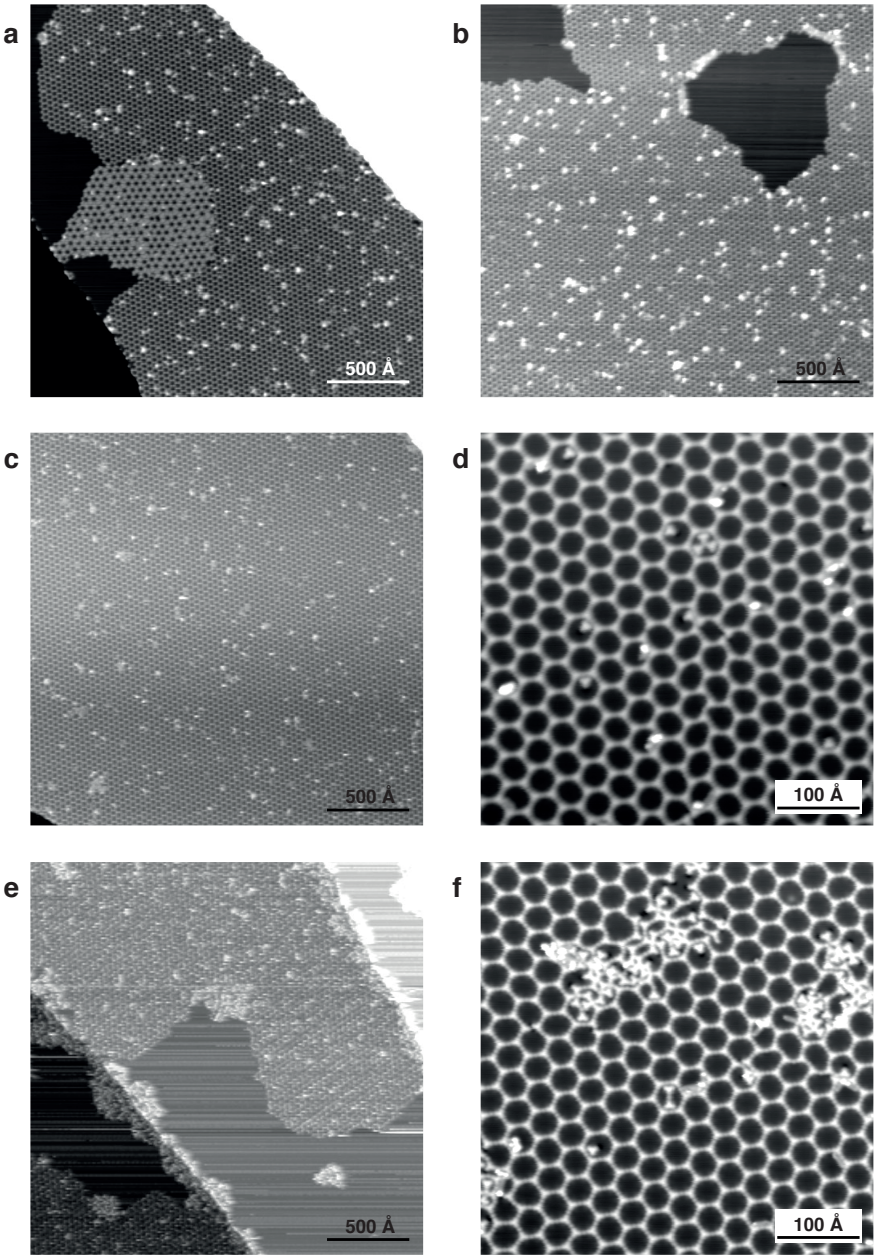

Figure 6.7: Annealing series showing the stability of the alkynyl-Ag networks. At 350 K (a), Phase II is still observed, while from 375 K (b) the networks seem to have fully evolved to phase I; at 425 K (c, d) the alkynyl-Ag networks (best image quality available for this stage yet adatoms are hardly visible in d) reach their largest extent, only very few impurities are still visible, some molecules are found within the pores; at 450 K (e, f) the networks decompose again (even for optimal tip condition, irregular structures lead to adsorbates dragged from side to side in the scanning frame). Setpoints: a-e $V_B = -1.0$ V, $I_T = 100$ pA; f $V_B = -0.1$ V, $I_T = 100$ pA. Annealing temperatures: a 350 K, b 375 K, c-d 425 K, e-f 450 K.

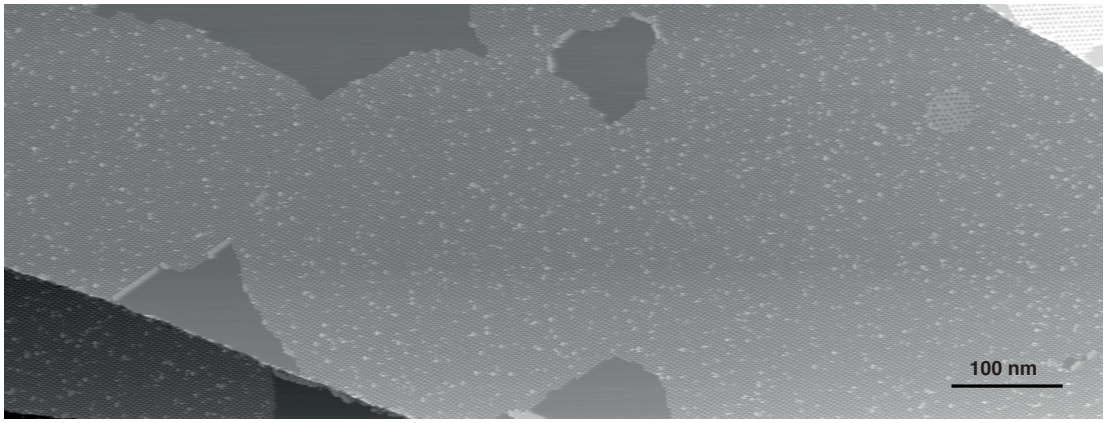

Figure 6.8: STM topograph demonstrating the extraordinary regularity and lateral extent of the alkynyl-Ag networks (here: more than 1 µm). Setpoint: $V_B = -2.0$ V, $I_T = 100$ pA. Annealing temperature: 375 K.

6.4 Network Analysis

In this section, both, the phase I network and the phase II macrocycles are analyzed by comparison to DFT models provided by Ari Seitsonen (published with parameters in [143]). The DFT simulation consists of a periodically extended unit cell of four molecules with six adatoms on the Ag(111) surface[2]. On the left side of Fig. 6.9, only simulation data is shown, while on the right side it transitions to an STM topograph of an O_2 exposed Ext-TEB@Ag(111) sample annealed to 350 K in order to show the good consistency between experiment and theory. The unit cell contains four instead of two Ext-TEB molecules because an FFT analysis of STM data consistent with DFT simulations demonstrates that the pores are not perfectly identical hexagons, they differ along the high symmetry direction of the substrate $[\bar{1}10]$ (unit cell vector $\mathbf{a}$) but are the same in direction $[\overline{11}2]$ (unit cell vector $\mathbf{b}$). The lengths of the unit cell vectors are $a = 63.6$ Å and $b = 35.0$ Å, the unit cell is commensurate with the substrate lattice. LEED by coworkers Zhang and Haag could not resolve the slight distortion of the network but did confirm the general appearance of the network and its thermal stability at room temperature [143]. The Ag adatoms are aligned in a distorted kagome lattice. It is noteworthy that single adatoms could be resolved with extraordinary clarity, which is especially well visible in the presentation of Fig. 6.10 (although it depicts phase II, the adatom-molecule linkages appear in the same fashion).

Phase II is shown in Fig. 6.10 with a fit of the DFT model obtained for phase I. Fig. 6.10 a shows the extraordinarily good imaging conditions at the setpoint given, providing the possibility of clearly resolving adatoms and molecules. The fit in Fig. 6.10 b achieves very good consistency and thus further confirms our experimental interpretations, although here the periodic DFT model of phase I was transferred to the not yet fully formed honeycomb network.

[2]The high symmetry directions of the DFT simulation were aligned with STM topography data and then superposed on the topography.

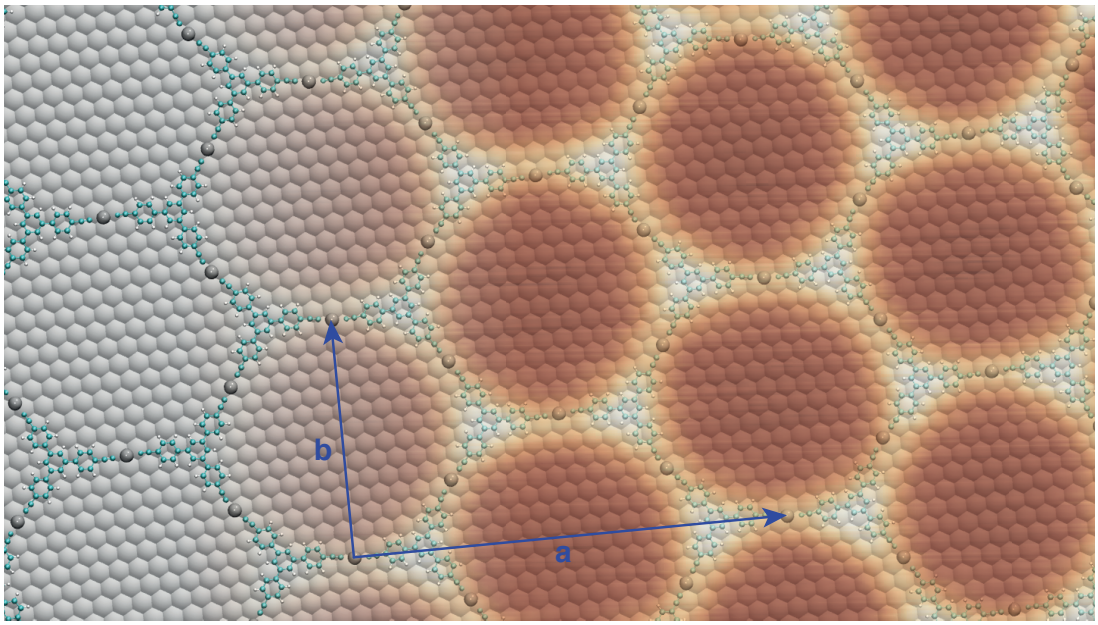

Figure 6.9: DFT calculated model of Ext-TEB alkynyl-Ag honeycomb networks on Ag(111) superposed on an STM topograph with varying transparency showing the good agreement between the calculation and experimental data. Setpoint: $V_B = -0.1$ V, $I_T = 100$ pA. Annealing temperature: 350 K.

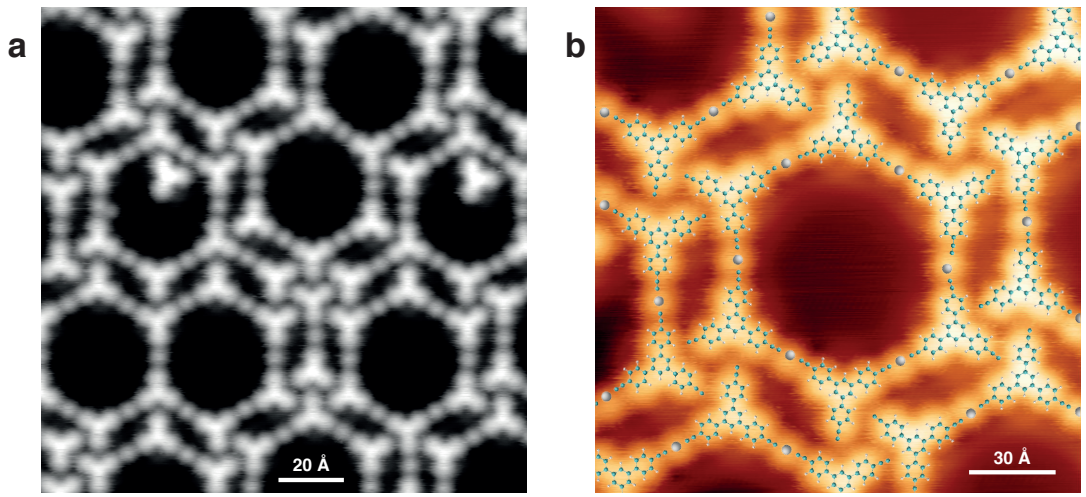

Figure 6.10: STM topograph depicting Phase II (a), and a zoom-in (b) superposed with a DFT calculated unit cell of the Ext-TEB Ag-Alkynyl network unit cell. Setpoints: $V_B = -0.2$ V, $I_T = 100$ pA. Annealing temperature: 300 K.

This analysis of phases I and II concludes the presentation of the primary experimental findings for Ext-TEB@Ag(111) with oxygen treatment at 200 K. A comprehensive discussion will follow at the end of this chapter complemented by final considerations at the end of this work. The next chapter is concerned with a different approach, incorporating the same ingredients, yet with different results.

6.5 Low Temperature O_2 Adsorption

In the experimental approach depicted in Fig. 6.11, both oxygen and the same adsorbates were used as in the 200 K oxygen treatment case, however, the oxygen exposure here occurred at a substrate temperature of 100 K. The very different results are an intriguing example of how different protocols in bottom-up synthesis can have tremendous effects. The molecules in this section were preadsorbed and annealed to room temperature before exposure, yet the oxygen treatment was carried out at the coldest accessible temperature at around 100 K after cooling down the substrate again. This resulted in the situation depicted in Fig. 6.11 a, showing parts of the Ag(111) surface in grey, oxidized patches in black (cf. white arrows in a) and some molecules. The nature of this oxygen adsorption was confirmed by XPS studies by colleagues Zhang and Haag [143], their results were consistent with previous XPS studies [148, 149].

Further XPS measurements by coworkers Zhang and Haag indicate a C 1s shift to lower binding energies as in the case for the 200 K treatment. O 1s measurements confirm the presence of oxygen and from an annealing temperature of 200 K onwards, atomic oxygen on the surface. Annealing to 200 K (Fig. 6.11 b) has results entirely different from a treatment with an exposure at 200 K. While some Ag-acetylides can be identified, the surface appears entirely different from previous experiments, especially due to the presence of point-like depressions and sombrero-shaped features. Both STM occurrences are in line with the XPS confirmation of oxygen presence. A comparison of STM data in the literature allows an identification of the depressions as Ag vacancies surrounded by oxygen atoms [150] and the sombrero protrusions as adsorbed oxygen, analogous to the O/Ag(110) case [151].

Annealing to 300 K (Fig. 6.11 c, d) and 400 K (Fig. 6.11 e, f) yielded some non-hexagonal Ag-acetylide pores (white arrow in d) but mostly resulted in irregular structures (image part d) and Ag islands (white arrows in e), most probably due to Ag extraction after O_2 dissociation.

In conclusion, this protocol did not yield regular structures but heavily modified the surface, which epitomizes the importance of carefully designing and testing the preparation methods of bottom-up synthesized materials since even the same combination of elements in a procedure can return completely different results.

6.6 Summary

In order to conclude this chapter, a summarization and outlook are provided. Herein, a novel 2D nanomaterial was constructed by employing a step-wise process, consisting of the adsorption of molecular tectons and their subsequent deprotonation and annealing. That the tectons originally occupied the surface in their protonated form was evidenced by STM images and previous research, along with DFT and XPS data. By annealing the molecular tectons without

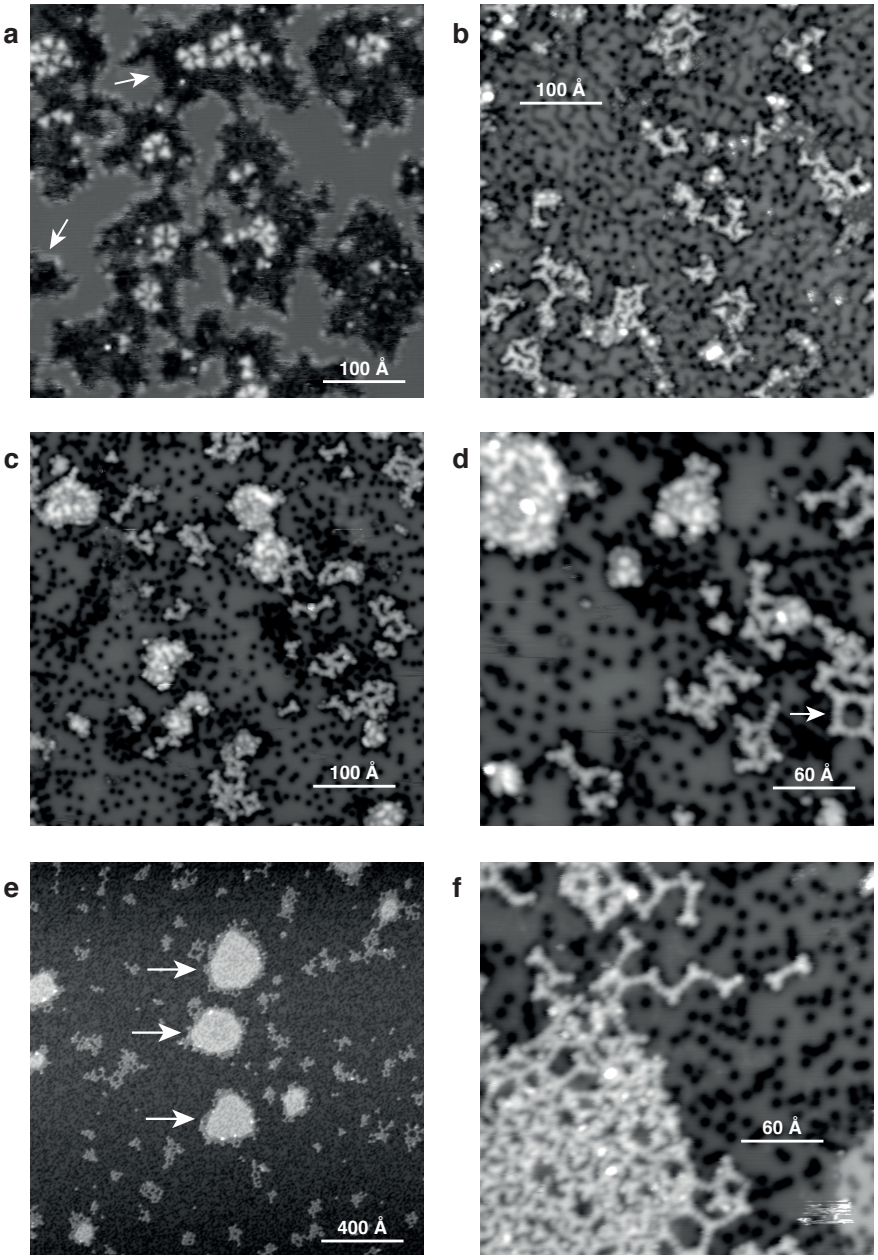

Figure 6.11: STM topographs showing Ext-TEB and oxygen coadsorbed at 100 K (a) and subsequently annealed up to 400 K. The situation is completely different from the deprotonation reaction observed for an oxygen treatment at 200 K. Depressed areas (white arrows, a) are identified as oxidized surface. Annealing induces the same alkynyl reaction as with previous samples (b, c, esp. white arrow in d), but no large scale networks form and oxygen stays adsorbed. Upon annealing to 400 K, silver islands aggregate (white arrows, e) and uncontrolled reactions between molecules and Ag adatoms occur (f, much like Fig. 6.7 f). Setpoints: a $V_B = 1.0$ V, $I_T = 100$ pA; b-d $V_B = -0.1$ V, $I_T = 100$ pA; e $V_B = -1.0$ V, $I_T = 100$ pA; f $V_B = -0.2$ V, $I_T = 100$ pA. Prep./Ann. T: a 100 K, b 200 K, c-d 300 K, e-f 400 K.

prior deprotonation, the O_2 treatment at 200 K was shown to be of crucial importance. After deprotonation, again XPS and STM data were correlated with previous research on Cu(111), which led to the confirmation that indeed the oxygen treatment led to the deprotonation. Unfortunately, the reaction mechanism, i. e. whether the oxygen really abstracted the hydrogen via an Eley-Rideal or rather via a Langmuir-Hinshelwood mechanism and which products occur remains elusive, even after TPD measurements by Yiqi Zhang and Felix Haag[3].

Nonetheless, a stable recipe was established, since it was possible to deprotonate virtually all adsorbate molecules as a comparison between DFT and XPS data revealed. Thereafter, annealing conditions were varied in order to achieve the best possible networks, resulting in the discovery of an ideal temperature of ca. 375-425 K, at which substrate terrace wide coverage of nearly perfect organo-metallic networks were found, which were stable up to room temperature (as evidenced by LEED measurements, which showed that the network was intact) and had a lateral dimension of at least one micrometer. Nearly perfect agreement between these networks and their simulated counterparts was observed. Although conversion to a covalent C-C network was not feasible and higher annealing temperature instead destroyed the metal-alkynyl network, it is assumed that the organometallic network's bonding mechanism is covalent to a significant degree [140]. In the last part, an alternative preparation procedure is shown, which leads to tremendously different effects with a drastically altered surface structure, especially in order to highlight the importance of finely tuning the synthesis of 2D-bottom-up constructed materials.

It should be noted that in order to demonstrate the significance of both, substrate and gas choice, further experiments were carried out on Au(111) and with CO and H_2O on Ag(111), in which neither gas was able abstract the terminal hydrogen from the Ext-TEB molecule. Neither would the synthesis protocol tolerate a change of substrate, further confirming the statement above that finely tuning the fabrication process is of paramount importance.

As for the significance of the items presented, several aspects have to be highlighted. First, the resulting networks are extraordinarily large, regular and robust. Second, these networks were formed by utilizing terminal ethynyls as functional groups instead of e. g. Ullmann coupling, avoiding possible halogenic byproducts. And third, that an extraordinarily precise mechanism for the deprotonation of terminal alkynes on Ag(111) was discovered with possible applications for other molecules.

[3]Only the expected natural mass ratio for oxygen isotopes was found when probing for hydrogen/oxygen compounds shortly after exposure.

7 Conclusion and Outlook

This thesis explored new grounds in the field of on-surface synthesis by introducing and characterizing two novel synthesis methods. Both methods are extraordinary in the sense that they contain ingredients going beyond the regular settings of interfacial reactions under ultra-high vacuum conditions.

In the first part a furan ring-closing hydroalkoxylation was investigated. The thesis demonstrated that the reactant is irreversibly converted into a new species and unraveled the dominant pathway which carries the special ingredient that a tunneling-mediated step enables the conversion at unprecedentedly low temperatures down to 150 K. A thorough understanding of the reaction pathway was obtained via the interplay of many experimental methods combined with state-of-the-art theoretical modeling. In order to provide unambiguous evidence, a comparison to a molecule with a heavier hydrogen isotope at the relevant group was carried out. The markedly reduced reaction rate of the deuterated species left no doubt about the involvement of tunneling in the synthesis pathway. Thus, this reaction represents the first complex synthesis approach based on quantum tunneling of hydrogen atoms. It exceeds the scope of known tunneling-related reactions which are limited to elementary conversions such as simple (de-)hydrogenation and tautomerization scenarios.

A synthesis method based on a tunneling-related rate-limiting process can provide desirable advantages over classical approaches. First, the selectivity against side reactions can be improved. While the tunneling rate remains finite for low temperatures, the rates for all classical reactions overcoming a barrier drop to zero. Thus, the yield of the targeted synthesis product can be optimized by carrying out the tunneling-mediated synthesis at lower temperatures. Second, a tunneling process is extremely sensitive to the exact positioning of the involved atoms which can be utilized to control the related synthesis. In the reaction mechanism at hand, we observed a tremendous influence on the reaction rates depending on whether the H atom of the involved hydroxy group pointed towards or away from the alkyne. Thus, the -OH configuration can be regarded as a trigger allowing to control when the reaction is taking place. In the presented case, this sensitive trigger mechanism rationalized the strong influence of the self-assembly behavior on the covalent synthesis. In general, a variety of other methods can be envisioned to profit from the sensitive trigger. For example, resonant excitation of vibrational modes of the OH group appears attractive for the field of light-induced chemistry. Third, even though the ring-closure at hand represents an intramolecular conversion, it raises hopes for applying the approach to intermolecular reactions. The molecules have to be carefully designed, so that their conformation on the surface would allow for a tunneling-mediated polymerization. A potential impact of this study is that it raises the awareness about tunneling processes in bottom-up synthesis. It seems likely that similar mechanisms are operational in other reactions too, but which might have been overlooked so far.

In the second part, an oxygen-mediated deprotonation of alkynyls was carried out. The

special ingredient distinguishing this approach from other methods is exposing the sample, already carrying the adsorbed precursors, with molecular oxygen being in the gas phase at a carefully selected temperature to initiate highly selective dehydrogenation of the adsorbate's terminal alkynes. This treatment allows for an extraordinarily clean process, as the gaseous byproducts readily desorb and only the deprotonated molecules remain on the sample. After such preparation, a regular annealing step can easily and reliably convert the organic adlayer into a highly regular and robust organometallic honeycomb network stabilized through Ag-bis-alkynyl bridges. The cleanliness mentioned above is an enormous advantage when compared to other reaction types, such as Ullmann coupling. While adsorbed halogens can hinder polymerization processes in later steps, H is elusive and will not stay on the surface. Also, the method provides an interesting alternative to solid-liquid or electrochemical setups without the requirement of using an omnipresent solvent potentially interfering with the fabrication process. Furthermore, a low onset temperature is observed, something desirable within limits in 2D bottom-up synthesis, see above. Moreover, the networks achieved reach very high quality and long-range order, especially with regard to the preparation mode based on terminal-alkyne hydrogen abstraction.

Lastly, the material is robust and stable at room temperature. These features are of high importance when considering applications in electronics or as a membrane. The higher stability is required when a material ought to survive the conditions outside of the protective UHV environment in real devices under atmospheric conditions.

Both of the reaction mechanisms explored have their unique capabilities and possible applications, e. g. with regard to electronics, magnetics and optics. Their main advantage is that both depend on trigger elements that render them highly selective and controllable. This facilitates the pursuit of the main goal in bottom-up synthesis: building up atomically precise structures from building blocks according to protocol at will. They require further investigation in order to show whether the behavior of the molecules at hand can be generalized to other situations, as is usually the case in basic research. Yet these novel protocols are already - in the way they have been presented and investigated - valuable tools in the realm of on-surface synthesis and they show novel, intriguing features, which warrant recognition and further investigation.

8 Acknowledgements

I would like to thank PD Dr. Florian Klappenberger for the chance to research and study at TUM and especially for his patient and diligent advice and support. Furthermore I would like to thank both, PD Dr. Florian Klappenberger and Prof. Dr. Johannes Barth for giving me the opportunity to work at E20.

A special thanks is in order for Prof. Dr. Peter Feulner, whom I had the honor of sharing an office with. A true veteran of his profession, he never grew tired of my questions and was rapidly able to repair our equipment when necessary, yet on top of all this, his wit and humor made the time in (t)his office extraordinarily enjoyable.

I would further like to thank my JT-STM coworkers, Dr. Yiqi Zhang, Martin Uphoff and Dr. Raphael Hellwig. Yiqi especially, since he (together with Borja Cirera) was the person who first introduced me to STM and whom I closely collaborated with on the Ext-TEB experiments in this work in particular, Martin and Raphael for the close and fruitful collaboration on the JT-STM setup.

Moreover, I would like to thank the other members of the Klappenberger group, especially my beamtime colleagues Mateusz Paszkiewicz, Liding Zhang, Dr. Tao Lin and Dr. Yiqi Zhang.

In addition I want to thank all the other colleagues who provided help whenever needed, in particular Dr. Anthoula Papageorgiou, Dr. Francesco Allegretti, Peter Deimel and Felix Haag (esp. for the PSD collaboration), Dr. Knud Seufert, Sabine Synkule and Pascal Leone (esp. when the lab was under water), Dr. Hartmut Schlichting, Dr. Joachim Reichert and Prof. Dr. Wilhelm Auwärter for fruitful discussion and support, our technical and administrative team without whom all of us would have had a hard time, Reinhold Schneider, Max Glanz, Karl Eberle and Viktoria Blaschek.

I would further like to thank Dr. Katharina Diller for authorizing me to use her graphics in the XPS and NEXAFS parts of the theory chapter.

I also thank our collaborators, chemists and theoreticians as well as other experimentalists, especially Murat Anil Öner, Prof. Dr. Carlos-Andres Palma, Prof. Dr. Jonas Björk, Dr. Ari Seitsonen, Dr. Ping Du, Dr. Svetlana Klyatskaya, Prof. Dr. Mario Ruben and Dr. Alexei Nefedov.

I would also like to express my gratitude to all the colleagues in our lunch/dinner/barbecue group, Martin Uphoff, Andreas Walz, Dr. Jacob Ducke, Domenik Zimmermann, Sabine Synkule, Mathias Pörtner, Eduardo Rascon, Karolina Stoiber, Aleksandr Baklanov, Dr. Alex Riss, Dr. Felix Bischoff, Dr. Tobias Kaposi, Dr. Maryam Ebrahimi, Dr. Reza Kakavandi and Prof. Dr. Peter Feulner, you had a great part in making my time at E20 exceptionally pleasant.

Finally I would like to thank my family, my parents Ingrid and Josef and my grandmother Marianne who have continuously supported me during my studies and without whom this would not have been possible.

List of Publications

The following list sums up my contributions to scientific publications; this work mainly draws from the two uppermost entries. Some of the figures used in this work are republished from the first entry, but are, unless someone else is specifically credited, my own work. Any previous publication is nonetheless clearly labeled and republication is authorized.

- T. Paintner, J. Björk, P. Du, S. Klyatskaya, M. Paszkiewicz, R. Hellwig, M. Uphoff, M. A. Öner, E. Cuniberto, P. S. Deimel, Y.-Q. Zhang, C. A. Palma, F. Allegretti, M. Ruben, J. V. Barth, F. Klappenberger, *Quantum tunneling-mediated interfacial synthesis of a benzofuran derivative, accepted by Angewandte Chemie*, 2019

- Y.-Q. Zhang, T. Paintner, R. Hellwig, F. Haag, F. Allegretti, P. Feulner, S. Klyatskaya, M. Ruben, A. P. Seitsonen, J. V. Barth, F. Klappenberger, *Synthesizing highly regular single-layer alkynyl-silver networks at the micrometer scale via gas-mediated surface reaction*, Journal of the American Chemical Society 2019, 13, 5087. `https://doi.org/10.1021/jacs.8b13547`

- R. Hellwig, M. Uphoff, T. Paintner, J. Björk, M. Ruben, F. Klappenberger, J. V. Barth, *Ho-mediated alkyne reactions at low temperatures on Ag(111)*, Chemistry – A European Journal 2018, 24, 16126. `https://doi.org/10.1002/chem.201803102`

- H. Aldahhak, M. Paszkiewicz, E. Rauls, F. Allegretti, S. Tebi, A. C. Papageorgiou, Y.-Q. Zhang, L. Zhang, T. Lin, T. Paintner, R. Koch, W. G. Schmidt, J. V. Barth, W. Schöfberger, S. Müllegger, F. Klappenberger, U. Gerstmann, *Identifying on-surface site-selective chemical conversions by theory-aided NEXAFS spectroscopy: The case of free-base corroles on Ag(111)*, Chemistry – A European Journal 2018, 24, 6787. `https://doi.org/10.1002/chem.201705921`

- F. Klappenberger, R. Hellwig, P. Du, T. Paintner, M. Uphoff, L. Zhang, T. Lin, B. Moghanaki, M. Paszkiewicz, I. Vobornik, J. Fujii, O. Fuhr, Y.-Q. Zhang, F. Allegretti, M. Ruben, J. V. Barth, *Functionalized graphdiyne nanowires: On-surface synthesis and assessment of band structure, flexibility, and information storage potential*, Small 2018, 14, 1704321. `https://doi.org/10.1002/smll.201704321`

- A. Ozcelik, R. Pereira-Cameselle, A. von Weber, M. Paszkiewicz, M. Carlotti, T. Paintner, L. Zhang, T. Lin, Y.-Q. Zhang, J. V. Barth, T. van den Nobelen, R. C. Chiechi, M. Jakob, U. Heiz, S. Chiussi, A. Kartouzian, F. Klappenberger, J. L. Alonso-Gómez, *Device-compatible chiroptical surfaces through self-assembly of enantiopure allenes*, Langmuir 2018, 34, 15, 4548. `https://doi.org/10.1021/acs.langmuir.8b00305`

- R. Hellwig, T. Paintner, Z. Chen, M. Ruben, A. P. Seitsonen, F. Klappenberger, H. Brune, J. V. Barth, *Epitaxy-induced assembly and enantiomeric switching of an on-surface formed dinuclear organocobalt complex*, ACS Nano 2017, 11, 2, 1347. https://doi.org/10.1021/acsnano.6b06114
- P. B. Weber, R. Hellwig, T. Paintner, M. Lattelais, M. Paszkiewicz, P. C. Aguilar, P. S. Deimel, Y. Guo, Y.-Q. Zhang, F. Allegretti, A. C. Papageorgiou, J. Reichert, S. Klyatskaya, M. Ruben, J. V. Barth, M.-L. Bocquet, F. Klappenberger, *Surface-guided formation of an organocobalt complex*, Angewandte Chemie 2016, 128, 5848. https://doi.org/10.1002/ange.201600567

Disclaimer

This is my own work. Only the references cited have been used in the way indicated. Schemes from [66] have been republished with permission by the original author. Fig. 6.4 is reprinted (slightly adapted) with permission by the American Chemical Society. Figs. adapted from [108] are reproduced with permission by the copyright holder Wiley-VCH Verlag GmbH & Co. KGaA. Figs. 1.1, 2.1 and 3.2 are used and provided with licenses CC BY-SA 2.5[1], CC BY-NC-SA 3.0[2] and CC BY-SA 2.0 AT[3], respectively (no changes were made to the images). Images that have previously been published in other scientific works and whose rights belong to their respective owners are included (and cited) herein in accordance with § 51 S. 1 No. 1 Urheberrechtsgesetz (German copyright law).

[1] https://creativecommons.org/licenses/by-sa/2.5/
[2] https://creativecommons.org/licenses/by-nc-sa/3.0/
[3] https://creativecommons.org/licenses/by-sa/2.0/at/deed.en

References

[1] H. H. Kung and M. C. Kung, *Heterogeneous catalysis: what lies ahead in nanotechnology*, Applied Catalysis A: General **246**, 193 (2003).

[2] F. Rosei, *Nanostructured surfaces: challenges and frontiers in nanotechnology*, Journal of Physics: Condensed Matter **16**, S1373 (2004).

[3] M. E. Vance, T. Kuiken, E. P. Vejerano, S. P. McGinnis, M. F. Hochella Jr, D. Rejeski, and M. S. Hull, *Nanotechnology in the real world: Redeveloping the nanomaterial consumer products inventory*, Beilstein Journal of Nanotechnology **6**, 1769 (2015).

[4] G. Paumier, *A comparison of the scales of various biological and technological objects.* `https://en.wikipedia.org/wiki/Nanoscopic_scale#/media/File:Biological_and_technological_scales_compared-en.svg`.

[5] J. I. Goldstein, D. E. Newbury, J. R. Michael, N. W. Ritchie, J. H. J. Scott, and D. C. Joy, *Scanning electron microscopy and X-ray microanalysis*, Springer, 2017.

[6] F. Klappenberger, *Two-dimensional functional molecular nanoarchitectures - complementary investigations with scanning tunneling microscopy and X-ray spectroscopy*, Progress in Surface Science **89**, 1 (2014).

[7] J. K. Gimzewski and C. Joachim, *Nanoscale science of single molecules using local probes*, Science **283**, 1683 (1999).

[8] D. M. Eigler and E. K. Schweizer, *Positioning single atoms with a scanning tunnelling microscope*, Nature **344**, 524 (1990).

[9] F. J. Giessibl, S. Hembacher, H. Bielefeldt, and J. Mannhart, *Subatomic features on the silicon(111)-(7× 7) surface observed by atomic force microscopy*, Science **289**, 422 (2000).

[10] J. V. Barth, *Molecular architectonic on metal surfaces*, Annual Review of Physical Chemistry **58**, 375 (2007).

[11] G. E. Moore, *Cramming more components onto integrated circuits*, Electronics **38**, 114 (1965).

[12] S. E. Thompson and S. Parthasarathy, *Moore's law: the future of Si microelectronics*, Materials Today **9**, 20 (2006).

[13] G. M. Whitesides and B. Grzybowski, *Self-assembly at all scales*, Science **295**, 2418 (2002).

[14] H. Fernandez-Moran, T. Oda, P. Blair, and D. E. Green, *A macromolecular repeating unit of mitochondrial structure and function correlated electron microscopic and biochemical studies of isolated mitochondria and submitochondrial particles of beef heart muscle*, Journal of Cell Biology **22**, 63 (1964).

[15] J. D. Watson, F. H. Crick, et al., *Molecular structure of nucleic acids*, Nature **171**, 737 (1953).

[16] G. Binnig, H. Rohrer, C. Gerber, and E. Weibel, *Surface studies by scanning tunneling microscopy*, Physical Review Letters **49**, 57 (1982).

[17] G. Binnig, H. Rohrer, C. Gerber, and E. Weibel, *7×7 reconstruction on Si(111) resolved in real space*, Physical Review Letters **50**, 120 (1983).

[18] J. Barth, H. Brune, G. Ertl, and R. Behm, *Scanning tunneling microscopy observations on the reconstructed Au(111) surface: Atomic structure, long-range superstructure, rotational domains, and surface defects*, Physical Review B **42**, 9307 (1990).

[19] D. M. Eigler, C. P. Lutz, and W. E. Rudge, *An atomic switch realized with the scanning tunnelling microscope*, Nature **352**, 600 (1991).

[20] W. Auwärter, K. Seufert, F. Bischoff, D. Ecija, S. Vijayaraghavan, S. Joshi, F. Klappenberger, N. Samudrala, and J. V. Barth, *A surface-anchored molecular four-level conductance switch based on single proton transfer*, Nature Nanotechnology **7**, 41 (2012).

[21] J. Shang, Y. Wang, M. Chen, J. Dai, X. Zhou, J. Kuttner, G. Hilt, X. Shao, J. M. Gottfried, and K. Wu, *Assembling molecular sierpiński triangle fractals*, Nature Chemistry **7**, 389 (2015).

[22] D. Kühne, F. Klappenberger, W. Krenner, S. Klyatskaya, M. Ruben, and J. V. Barth, *Rotational and constitutional dynamics of caged supramolecules*, Proceedings of the National Academy of Sciences **107**, 21332 (2010).

[23] K. von Bergmann, A. Kubetzka, O. Pietzsch, and R. Wiesendanger, *Interface-induced chiral domain walls, spin spirals and skyrmions revealed by spin-polarized scanning tunneling microscopy*, Journal of Physics: Condensed Matter **26**, 394002 (2014).

[24] L. Grill, M. Dyer, L. Lafferentz, M. Persson, M. V. Peters, and S. Hecht, *Nano-architectures by covalent assembly of molecular building blocks*, Nature Nanotechnology **2**, 687 (2007).

[25] Y.-Q. Zhang, M. Paszkiewicz, P. Du, L. Zhang, T. Lin, Z. Chen, S. Klyatskaya, M. Ruben, A. P. Seitsonen, J. V. Barth, and F. Klappenberger, *Complex supramolecular interfacial tessellation through convergent multi-step reaction of a dissymmetric simple organic precursor*, Nature Chemistry **10**, 296 (2018).

[26] S. Maier, *Alterations in the electronic structure upon hierarchical growth of 2D networks*, in Encyclopedia of Interfacial Chemistry: Surface Science and Electrochemistry, K. Wandelt, ed., Elsevier, 2018.

[27] F. Klappenberger, Y.-Q. Zhang, J. Björk, S. Klyatskaya, M. Ruben, and J. V. Barth, *On-surface synthesis of carbon-based scaffolds and nanomaterials using terminal alkynes*, Accounts of Chemical Research **48**, 2140 (2015).

[28] S. Maier, *On-surface synthesis of two-dimensional polymers: Rational design and electronic properties*, in On-Surface Synthesis II, D. G. de Oteyza and C. Rogero, eds., Cham, 2018, Springer International Publishing, pp. 179–194.

[29] R. P. Bell, *The application of quantum mechanics to chemical kinetics*, Proceedings of the Royal Society of London. Series A, Containing Papers of a Mathematical and Physical Character **139**, 466 (1933).

[30] R. P. Bell, *The Tunneling Effects in Chemistry*, Chapman and Hall, London, 1980.

[31] Y. Cha, C. J. Murray, and J. P. Klinman, *Hydrogen tunneling in enzyme reactions*, Science **243**, 1325 (1989).

[32] L. Masgrau, A. Roujeinikova, L. O. Johannissen, P. Hothi, J. Basran, K. E. Ranaghan, A. J. Mulholland, M. J. Sutcliffe, N. S. Scrutton, and D. Leys, *Atomic description of an enzyme reaction dominated by proton tunneling*, Science **312**, 237 (2006).

[33] P.-O. Löwdin, *Proton tunneling in dna and its biological implications*, Reviews of Modern Physics **35**, 724 (1963).

[34] R. J. Shannon, M. A. Blitz, A. Goddard, and D. E. Heard, *Accelerated chemistry in the reaction between the hydroxyl radical and methanol at interstellar temperatures facilitated by tunnelling*, Nature Chemistry **5**, 745 (2013).

[35] T. P. Goumans and J. Kästner, *Hydrogen-atom tunneling could contribute to H_2 formation in space*, Angewandte Chemie International Edition **49**, 7350 (2010).

[36] J. Kua, L. J. Lauhon, W. Ho, and W. A. Goddard III, *Direct comparisons of rates for low temperature diffusion of hydrogen and deuterium on Cu(001) from quantum mechanical calculations and scanning tunneling microscopy experiments*, The Journal of Chemical Physics **115**, 5620 (2001).

[37] M. Koch, M. Pagan, M. Persson, S. Gawinkowski, J. Waluk, and T. Kumagai, *Direct observation of double hydrogen transfer via quantum tunneling in a single porphycene molecule on a Ag(110) surface*, Journal of the American Chemical Society **139**, 12681 (2017).

[38] X. Meng, J. Guo, J. Peng, J. Chen, Z. Wang, J.-R. Shi, X.-Z. Li, E.-G. Wang, and Y. Jiang, *Direct visualization of concerted proton tunnelling in a water nanocluster*, Nature Physics **11**, 235 (2015).

[39] C. S. Tautermann and D. C. Clary, *The importance of tunneling in the first hydrogenation step in ammonia synthesis over a Ru(0001) surface*, The Journal of Chemical Physics **122**, 134702 (2005).

[40] T. Minato, S. Kajita, C.-L. Pang, N. Asao, Y. Yamamoto, T. Nakayama, M. Kawai, and Y. Kim, *Tunneling desorption of single hydrogen on the surface of titanium dioxide*, ACS Nano **9**, 6837 (2015).

[41] J. Eichhorn, T. Strunskus, A. Rastgoo-Lahrood, D. Samanta, M. Schmittel, and M. Lackinger, *On-surface ullmann polymerization via intermediate organometallic networks on Ag(111)*, Chemical Communications **50**, 7680 (2014).

[42] Z. Wang, Z. Liu, and F. Liu, *Organic topological insulators in organometallic lattices*, Nature Communications **4**, 1471 (2013).

[43] T. Krähling, *Tunneleffekt – Wellenfunktion und Potential (1)*. `http://www.semibyte.de/wp/graphicslibrary/gl-physics/tunneleffekt/#img1`.

[44] G. Gamow, *Zur Quantentheorie des Atomkernes*, Zeitschrift für Physik **51**, 204 (1928).

[45] E. Schrödinger, *An undulatory theory of the mechanics of atoms and molecules*, Physical Review **28**, 1049 (1926).

[46] C. Chen, *Introduction to scanning tunneling microscopy*, Monographs on the Physics and Chemistry of Materials, Oxford University Press, 2008.

[47] C. Kittel, *Introduction to solid state physics*, Wiley, 2005.

[48] J. Bardeen, *Tunnelling from a many-particle point of view*, Physical Review Letters **6**, 57 (1961).

[49] I. Giaever, *Electron tunneling between two superconductors*, Physical Review Letters **5**, 464 (1960).

[50] I. Giaever, *Energy gap in superconductors measured by electron tunneling*, Physical Review Letters **5**, 147 (1960).

[51] I. Giaever and K. Megerle, *Study of superconductors by electron tunneling*, Physical Review **122**, 1101 (1961).

[52] J. Bardeen, L. N. Cooper, and J. R. Schrieffer, *Theory of superconductivity*, Physical Review **108**, 1175 (1957).

[53] A. D. Gottlieb and L. Wesoloski, *Bardeen's tunnelling theory as applied to scanning tunnelling microscopy: a technical guide to the traditional interpretation*, Nanotechnology **17**, R57 (2006).

[54] R. C. Jaklevic and J. Lambe, *Molecular vibration spectra by electron tunneling*, Physical Review Letters **17**, 1139 (1966).

[55] R. Wiesendanger and M. Bode, *Nano- and atomic-scale magnetism studied by spin-polarized scanning tunneling microscopy and spectroscopy*, Solid State Communications **119**, 341 (2001).

[56] M. Julliere, *Tunneling between ferromagnetic films*, Physics Letters A **54**, 225 (1975).

[57] J. Tersoff and D. Hamann, *Theory and application for the scanning tunneling microscope*, Physical Review Letters **50**, 1998 (1983).

[58] J. Tersoff and D. Hamann, *Theory of the scanning tunneling microscope*, Physical Review B **31**, 805 (1985).

[59] J. V. Lauritsen and F. Besenbacher, *Model catalyst surfaces investigated by scanning tunneling microscopy*, Advances in Catalysis **50**, 97 (2006).

[60] P. Sautet, *Images of adsorbates with the scanning tunneling microscope: Theoretical approaches to the contrast mechanism*, Chemical Reviews **97**, 1097 (1997).

[61] A. Einstein, *Über einen die Erzeugung und Verwandlung des Lichtes betreffenden heuristischen Gesichtspunkt*, Annalen der Physik **4**, 132 (1905).

[62] `http://www.nobelprize.org/nobel_prizes/physics/laureates/1921/index.html`.

[63] H. Hertz, *Über einen Einfluss des ultravioletten Lichtes auf die electrische Entladung*, Annalen der Physik **267**, 983 (1887).

[64] W. Hallwachs, *Über den Einfluss des Lichtes auf electrostatisch geladene Körper*, Annalen der Physik **269**, 301 (1888).

[65] J. J. Thomson, *LVIII. On the masses of the ions in gases at low pressures*, The London, Edinburgh, and Dublin Philosophical Magazine and Journal of Science **48**, 547 (1899).

[66] K. Diller, *Free-base and metalated porphyrins on metal surfaces - a systematic X-ray spectroscopy and density functional theory investigation*, PhD thesis, Technische Universität München, 2013.

[67] M. Planck, *Über irreversible Strahlungsvorgänge*, Annalen der Physik **306**, 69 (1900).

[68] S. Hüfner, *Photoelectron spectroscopy: principles and applications*, vol. 82, Springer Science & Business Media, 2013.

[69] T. Koopmans, *Über die Zuordnung von Wellenfunktionen und Eigenwerten zu den einzelnen Elektronen eines Atoms*, Physica **1**, 104 (1934).

[70] B. D. Ratner and D. G. Castner, *Electron Spectroscopy for Chemical Analysis*, Wiley, 2009, p. 47.

[71] J. F. Watts and J. Wolstenholme, *An introduction to surface analysis by XPS and AES*, Wiley, 2003.

[72] H. Haken and H. C. Wolf, *Atom-und Quantenphysik: Einführung in die experimentellen und theoretischen Grundlagen*, Springer-Verlag, 2013.

[73] L. H. Thomas, *The motion of the spinning electron*, Nature **117**, 514 (1926).

[74] K. Oura, A. Zotov, V. Lifshits, A. Saranin, and M. Katayama, *Surface Science*, Springer, 2003.

[75] J. Stöhr, *NEXAFS spectroscopy*, vol. 25, Springer Science & Business Media, 2013.

[76] P. Hohenberg and W. Kohn, *Inhomogeneous electron gas*, Physical Review **136**, B864 (1964).

[77] J. Kohanoff, *Electronic structure calculations for solids and molecules: theory and computational methods*, Cambridge University Press, 2006.

[78] M. Born and R. Oppenheimer, *Zur Quantentheorie der Molekeln*, Annalen der Physik **389**, 457 (1927).

[79] W. Kohn and L. J. Sham, *Self-consistent equations including exchange and correlation effects*, Physical Review **140**, A1133 (1965).

[80] B. Brooks, R. Bruccoleri, D. Olafson, D. States, S. Swaminathan, and M. Karplus, *CHARMM: A program for macromolecular energy, minimization, and dynamics calculations*, Journal of Computational Chemistry **4**, 187 (1983).

[81] A. MacKerel Jr., C. Brooks III, L. Nilsson, B. Roux, Y. Won, and M. Karplus, *CHARMM: The Energy Function and Its Parameterization with an Overview of the Program*, vol. 1 of The Encyclopedia of Computational Chemistry, Wiley, 1998, p. 271.

[82] B. R. Brooks, C. L. Brooks, III, A. D. Mackerell, Jr., L. Nilsson, R. J. Petrella, B. Roux, Y. Won, G. Archontis, C. Bartels, S. Boresch, A. Caflisch, L. Caves, Q. Cui, A. R. Dinner, M. Feig, S. Fischer, J. Gao, M. Hodoscek, W. Im, K. Kuczera, T. Lazaridis, J. Ma, V. Ovchinnikov, E. Paci, R. W. Pastor, C. B. Post, J. Z. Pu, M. Schaefer, B. Tidor, R. M. Venable, H. L. Woodcock, X. Wu, W. Yang, D. M. York, and M. Karplus, *CHARMM: The biomolecular simulation program*, Journal of Computational Chemistry **30**, 1545 (2009).

[83] T. A. Halgren, *Merck molecular force field. I. Basis, form, scope, parameterization, and performance of MMFF94*, Journal of Computational Chemistry **17**, 490 (1996).

[84] T. A. Halgren, *Merck molecular force field. II. MMFF94 van der waals and electrostatic parameters for intermolecular interactions*, Journal of Computational Chemistry **17**, 520 (1996).

[85] T. A. Halgren, *Merck molecular force field. III. Molecular geometries and vibrational frequencies for MMFF94*, Journal of Computational Chemistry **17**, 553 (1996).

[86] T. A. Halgren and R. B. Nachbar, *Merck molecular force field. IV. Conformational energies and geometries for MMFF94*, Journal of Computational Chemistry **17**, 587 (1996).

[87] T. A. Halgren, *Merck molecular force field. V. Extension of MMFF94 using experimental data, additional computational data, and empirical rules*, Journal of Computational Chemistry **17**, 616 (1996).

[88] C.-A. Palma, J. Björk, F. Klappenberger, E. Arras, D. Kühne, S. Stafström, and J. V. Barth, *Visualization and thermodynamic encoding of single-molecule partition function projections*, Nature Communications **6**, 6210 (2015).

[89] L. Zhang, T. Miyamachi, T. Tomanić, R. Dehm, and W. Wulfhekel, *A compact sub-kelvin ultrahigh vacuum scanning tunneling microscope with high energy resolution and high stability*, Review of Scientific Instruments **82**, 103702 (2011).

[90] M. Schmid, *Schematic diagram of a scanning tunneling microscope.* `https://en.wikipedia.org/wiki/Scanning_tunneling_microscope#/media/File:ScanningTunnelingMicroscope_schematic.png`.

[91] G. Meyer, L. Bartels, and K.-H. Rieder, *Atom manipulation with the STM: nanostructuring, tip functionalization, and femtochemistry*, Computational Materials Science **20**, 443 (2001).

[92] L. Bartels, G. Meyer, and K.-H. Rieder, *Basic steps of lateral manipulation of single atoms and diatomic clusters with a scanning tunneling microscope tip*, Physical Review Letters **79**, 697 (1997).

[93] M. F. Crommie, C. P. Lutz, and D. M. Eigler, *Confinement of electrons to quantum corrals on a metal surface*, Science **262**, 218 (1993).

[94] B. Stipe, M. Rezaei, W. Ho, S. Gao, M. Persson, and B. Lundqvist, *Single-molecule dissociation by tunneling electrons*, Physical Review Letters **78**, 4410 (1997).

[95] S. Pan, Q. Fu, T. Huang, A. Zhao, B. Wang, Y. Luo, J. Yang, and J. Hou, *Design and control of electron transport properties of single molecules*, Proceedings of the National Academy of Sciences **106**, 15259 (2009).

[96] A. Zhao, S. Tan, B. Li, B. Wang, J. Yang, and J. Hou, *STM tip-assisted single molecule chemistry*, Physical Chemistry Chemical Physics **15**, 12428 (2013).

[97] G. Dujardin, R. Walkup, and P. Avouris, *Dissociation of individual molecules with electrons from the tip of a scanning tunneling microscope*, Science **255**, 1232 (1992).

[98] J. Gimzewski, T. Jung, M. Cuberes, and R. Schlittler, *Scanning tunneling microscopy of individual molecules: beyond imaging*, Surface Science **386**, 101 (1997).

[99] S.-W. Hla, L. Bartels, G. Meyer, and K.-H. Rieder, *Inducing all steps of a chemical reaction with the scanning tunneling microscope tip: towards single molecule engineering*, Physical Review Letters **85**, 2777 (2000).

[100] F. Reif, *Fundamentals of statistical and thermal physics*, Waveland Press, 2009.

[101] W. B. Krenner, *Supramolecular Templates*, PhD thesis, Technische Universität München, 2012.

[102] J. Müller, *Interaction of the Pt(111) surface with adsorbed Xe atoms*, Physical Review Letters **65**, 3021 (1990).

[103] E. Zaremba and W. Kohn, *Theory of helium adsorption on simple and noble-metal surfaces*, Physical Review B **15**, 1769 (1977).

[104] A. Luntz, J. Grimblot, and D. Fowler, *Sequential precursors in dissociative chemisorption: O_2 on Pt(111)*, Physical Review B **39**, 12903 (1989).

[105] G. Ertl, *Reactions at well-defined surfaces*, Surface Science **299**, 742 (1994).

[106] T. Fauster, L. Hammer, K. Heinz, and A. Schneider, *Oberflächenphysik: Grundlagen und Methoden*, Walter de Gruyter, 2013.

[107] P. Feulner and D. Menzel, *Simple ways to improve "flash desorption" measurements from single crystal surfaces*, Journal of Vacuum Science and Technology **17**, 662 (1980).

[108] T. Paintner, J. Björk, P. Du, S. Klyatskaya, M. Paszkiewicz, R. Hellwig, M. Uphoff, M. A. Öner, E. Cuniberto, P. S. Deimel, Y.-Q. Zhang, C. A. Palma, F. Allegretti, M. Ruben, J. V. Barth, and F. Klappenberger, *Quantum tunneling-mediated interfacial synthesis of a benzofuran derivative*, accepted by Angewandte Chemie, (2019).

[109] F. Hund, *Zur Deutung der Molekülspektren. III.*, Zeitschrift für Physik **43**, 805 (1927).

[110] L. Lauhon and W. Ho, *Direct observation of the quantum tunneling of single hydrogen atoms with a scanning tunneling microscope*, Physical Review Letters **85**, 4566 (2000).

[111] A. D. Jewell, G. Peng, M. F. Mattera, E. A. Lewis, C. J. Murphy, G. Kyriakou, M. Mavrikakis, and E. C. H. Sykes, *Quantum tunneling enabled self-assembly of hydrogen atoms on Cu (111)*, ACS Nano **6**, 10115 (2012).

[112] T. Paintner, *On-surface chemistry of functionalized terphenylene terminal alkyne compounds*, master's thesis, Technische Universität München, 2015.

[113] HyperChem(TM) Professional 7.51, Hypercube, Inc., 1115 NW 4th Street, Gainesville, Florida 32601, USA.

[114] J. A. Bis, P. Vishweshwar, D. Weyna, and M. J. Zaworotko, *Hierarchy of supramolecular synthons: Persistent hydroxyl···pyridine hydrogen bonds in cocrystals that contain a cyano acceptor*, Molecular Pharmaceutics **4**, 401 (2007).

[115] M. Viswamitra, R. Radhakrishnan, J. Bandekar, and G. R. Desiraju, *Evidence for OH···C and NH···C hydrogen bonding in crystalline alkynes, alkenes, and aromatics*, Journal of the American Chemical Society **115**, 4868 (1993).

[116] E. Arras, A. P. Seitsonen, F. Klappenberger, and J. V. Barth, *Nature of the attractive interaction between proton acceptors and organic ring systems*, Physical Chemistry Chemical Physics **14**, 15995 (2012).

[117] D. Abbasi-Pérez, J. M. Recio, and L. Kantorovich, *The role of isomerization in the kinetics of self-assembly: p-terphenyl-m-dicarbonitrile on the Ag(111) surface*, Physical Chemistry Chemical Physics **17**, 11182 (2015).

[118] F. Klappenberger, R. Hellwig, P. Du, T. Paintner, M. Uphoff, L. Zhang, T. Lin, B. A. Moghanaki, M. Paszkiewicz, I. Vobornik, et al., *Functionalized graphdiyne nanowires: On-surface synthesis and assessment of band structure, flexibility, and information storage potential*, Small **14**, 1704321 (2018).

[119] J. Solomon, R. Madix, and J. Stöhr, *Orientation and absolute coverage of furan and 2,5-dihydrofuran on Ag(110) determined by near edge X-ray absorption fine structure and X-ray photoelectron spectroscopy*, The Journal of Chemical Physics **94**, 4012 (1991).

[120] J. Solomon, R. Madix, and J. Stöhr, *Orientation and absolute coverage of benzene, aniline, and phenol on Ag(110) determined by NEXAFS and XPS*, Surface Science **255**, 12 (1991).

[121] J. A. Lloyd, A. C. Papageorgiou, S. Fischer, S. C. Oh, O. Saglam, K. Diller, D. A. Duncan, F. Allegretti, F. Klappenberger, M. Stöhr, R. J. Maurer, K. Reuter, J. Reichert, and J. V. Barth, *Dynamics of spatially confined bisphenol A trimers in a unimolecular network on Ag(111)*, Nano Lett. **16**, 1884 (2016).

[122] A. C. Papageorgiou, S. Fischer, J. Reichert, K. Diller, F. Blobner, F. Klappenberger, F. Allegretti, A. P. Seitsonen, and J. V. Barth, *Chemical transformations drive complex self-assembly of uracil on close-packed coinage metal surfaces*, ACS Nano **6**, 2477 (2012).

[123] L. Smykalla, P. Shukrynau, C. Mende, H. Lang, M. Knupfer, and M. Hietschold, *Photoelectron spectroscopy investigation of the temperature-induced deprotonation and substrate-mediated hydrogen transfer in a hydroxyphenyl-substituted porphyrin*, Chemical Physics **450-451**, 39 (2015).

[124] T. Miyazaki, *Atom tunneling phenomena in physics, chemistry and biology*, vol. 36, Springer Science & Business Media, 2013.

[125] W. H. Weinberg, *Eley-rideal surface chemistry: Direct reactivity of gas phase atomic hydrogen with adsorbed species*, Accounts of Chemical Research **29**, 479 (1996).

[126] A. L. Ivanovskii, *Graphynes and graphdyines*, Progress in Solid State Chemistry **41**, 1 (2013).

[127] Y. J. Li, L. Xu, H. B. Liu, and Y. L. Li, *Graphdiyne and graphyne: from theoretical predictions to practical construction*, Chemical Society Reviews **43**, 2572 (2014).

[128] K. Srinivasu and S. K. Ghosh, *Graphyne and graphdiyne: promising materials for nanoelectronics and energy storage applications*, Journal of Physical Chemistry C **116**, 5951 (2012).

[129] D. Prenzel, T. Sander, J. Gebhardt, H. Soni, F. Hampel, A. Görling, S. Maier, and R. R. Tykwinski, *Triethynylmethanol derivatives: Stable acetylenic building blocks for surface chemistry*, Chemistry - A European Journal **23**, 1846 (2017).

[130] Y. Q. Zhang, N. Kepčija, M. Kleinschrodt, K. Diller, S. Fischer, A. C. Papageorgiou, F. Allegretti, J. Björk, S. Klyatskaya, F. Klappenberger, M. Ruben, and J. V. Barth, *Homo-coupling of terminal alkynes on a noble metal surface*, Nature Communications **3**, 1286 (2012).

[131] N. Kepčija, Y. Q. Zhang, M. Kleinschrodt, J. Björk, S. Klyatskaya, F. Klappenberger, M. Ruben, and J. V. Barth, *Steering on-surface self-assembly of high-quality hydrocarbon networks with terminal alkynes*, Journal of Physical Chemistry C **117**, 3987 (2013).

[132] Y.-Q. Zhang, J. Björk, P. Weber, R. Hellwig, K. Diller, A. C. Papageorgiou, S. C. Oh, S. Fischer, F. Allegretti, S. Klyatskaya, M. Ruben, J. V. Barth, and F. Klappenberger, *Unusual deprotonated alkynyl hydrogen bonding in metal-supported hydrocarbon assembly*, Journal of Physical Chemistry C **119**, 9669 (2015).

[133] R. Hellwig, M. Uphoff, T. Paintner, J. Björk, M. Ruben, F. Klappenberger, and J. V. Barth, *Ho-mediated alkyne reactions at low temperatures on Ag(111)*, Chemistry - A European Journal **24**, 16126 (2018).

[134] J. Björk, *Reaction mechanisms for on-surface synthesis of covalent nanostructures*, Journal of Physics: Condensed Matter **28**, 083002 (2016).

[135] J. Lipton-Duffin, O. Ivasenko, D. Perepichka, and F. Rosei, *Synthesis of polyphenylene molecular wires by surface-confined polymerization*, Small **5**, 592 (2009).

[136] M. Lackinger, *Surface-assisted ullmann coupling*, Chemical Communications **53**, 7872 (2017).

[137] S. Schlögl, W. M. Heckl, and M. Lackinger, *On-surface radical addition of triply iodinated monomers on Au(111) - the influence of monomer size and thermal post-processing*, Surface Science **606**, 999 (2012).

[138] R. Gutzler, H. Walch, G. Eder, S. Kloft, W. M. Heckl, and M. Lackinger, *Surface mediated synthesis of 2D covalent organic frameworks: 1,3,5-tris(4-bromophenyl)benzene on graphite(001), Cu(111), and Ag(110)*, Chemical Communications **0**, 4456 (2009).

[139] Q. Sun, L. L. Cai, H. H. Ma, C. X. Yuan, and W. Xu, *Dehalogenative homocoupling of terminal alkynyl bromides on Au(111): incorporation of acetylenic scaffolding into surface nanostructures*, ACS Nano **10**, 7023 (2016).

[140] Z. Yang, J. Gebhardt, T. A. Schaub, T. Sander, J. Schönamsgruber, H. Soni, A. Görling, M. Kivala, and S. Maier, *Two-dimensional delocalized states in organometallic bis-acetylide networks on Ag(111)*, Nanoscale **10**, 3769 (2018).

[141] W. Wang, X. Shi, S. Wang, M. A. Van Hove, and N. Lin, *Single-molecule resolution of an organometallic intermediate in a surface-supported ullmann coupling reaction*, Journal of the American Chemical Society **133**, 13264 (2011).

[142] Z. Wang, N. Su, and F. Liu, *Prediction of a two-dimensional organic topological insulator*, Nano Letters **13**, 2842 (2013).

[143] Y. Q. Zhang, T. Paintner, R. Hellwig, F. Haag, F. Allegretti, P. Feulner, S. Klyatskaya, M. Ruben, A. P. Seitsonen, J. V. Barth, and F. Klappenberger, *Synthesizing highly regular single-layer alkynyl-silver networks at the micrometer scale via gas-mediated surface reaction*, Journal of the American Chemical Society **141**, 5087 (2019).

[144] N. Orozco, G. Kyriakou, S. K. Beaumont, J. Fernandez Sanz, J. P. Holgado, M. J. Taylor, J. P. Espinós, A. M. Márquez, D. J. Watson, A. R. Gonzalez-Elipe, and R. M. Lambert, *Critical role of oxygen in silver-catalyzed glaser–hay coupling on Ag(100) under vacuum and in solution on Ag particles*, ACS Catalysis **7**, 3113 (2017).

[145] M. Di Giovannantonio, M. El Garah, J. Lipton-Duffin, V. Meunier, L. Cardenas, Y. Fagot Revurat, A. Cossaro, A. Verdini, D. F. Perepichka, F. Rosei, et al., *Insight into organometallic intermediate and its evolution to covalent bonding in surface-confined ullmann polymerization*, ACS Nano **7**, 8190 (2013).

[146] Q. Sun, L. Cai, S. Wang, R. Widmer, H. Ju, J. Zhu, L. Li, Y. He, P. Ruffieux, R. Fasel, et al., *Bottom-up synthesis of metalated carbyne*, Journal of the American Chemical Society **138**, 1106 (2016).

[147] J. Liu, Q. Chen, L. Xiao, J. Shang, X. Zhou, Y. Zhang, Y. Wang, X. Shao, J. Li, W. Chen, et al., *Lattice-directed formation of covalent and organometallic molecular wires by terminal alkynes on Ag surfaces*, ACS Nano **9**, 6305 (2015).

[148] C. T. Campbell, *Atomic and molecular oxygen adsorption on Ag(111)*, Surface Science **157**, 43 (1985).

[149] C. T. Campbell, *An XPS study of molecularly chemisorbed oxygen on Ag(111)*, Surface Science Letters **173**, L641 (1986).

[150] B. Andryushechkin, V. M. Shevlyuga, T. V. Pavlova, G. Zhidomirov, and K. Eltsov, *Adsorption of O_2 on Ag(111): evidence of local oxide formation*, Physical Review Letters **117**, 056101 (2016).

[151] J. Pal, T. B. Rawal, M. Smerieri, S. Hong, M. Alatalo, L. Savio, L. Vattuone, T. S. Rahman, and M. Rocca, *Adatom extraction from pristine metal terraces by dissociative oxygen adsorption: Combined STM and density functional theory investigation of O/Ag(110)*, Physical Review Letters **118**, 226101 (2017).

List of Figures